Technische Universität München
Max-Planck-Institut für Quantenoptik

Ultracold Rubidium Molecules

Thomas Volz

Vollständiger Abdruck der von der Fakultät für Physik der Technischen Universität München zur Erlangung des akademischen Grades eines

Doktors der Naturwissenschaften (Dr. rer. nat.)

genehmigten Dissertation.

Vorsitzender:	Univ.-Prof. Dr. M. Stutzmann
Prüfer der Dissertation:	
	1. Hon.-Prof. Dr. G. Rempe
	2. Univ.-Prof. Dr. H. Friedrich

Die Dissertation wurde am 13.03.2007 bei der Technischen Universität München eingereicht und durch die Fakultät für Physik am 11.04.2007 angenommen.

Abstract

This thesis describes experiments with diatomic molecules associated from ultracold ^{87}Rb atoms using magnetically-induced Feshbach resonances. The association method is based on a slow magnetic-field ramp across a Feshbach resonance which converts atom pairs into bound molecules. This constitutes a form of superchemistry: The reaction is reversible and coherent. No latent heat is released, and as a consequence, the Feshbach molecules are about as cold as the atoms from which they are associated.

The first experiment introduced in this thesis, characterizes the broadest of the known Feshbach resonances in ^{87}Rb. To that end, the mean-field driven expansion of an atomic Bose-Einstein condensate near resonance is studied and the scattering length as a function of magnetic field is extracted. The position and magnetic-field width of the Feshbach resonance are determined to be 1007.4 G and 200 mG, respectively.

Subsequently, this Feshbach resonance is used to associate ultracold molecules from a Bose-Einstein condensate of ^{87}Rb atoms. The molecules are detected by a Stern-Gerlach method. This yields the magnetic moment of the molecules as a function of magnetic field. Due to an avoided crossing between two bound states, the magnetic moment changes sign at 1001.7 G. As a consequence, an applied magnetic-field gradient creates a 1D harmonic trap for the molecules. The corresponding harmonic oscillation is observed.

Next, we study the dissociation of the molecules by magnetic-field ramps that are linear in time. From the kinetic energy released in the dissociation process, the magnetic-field widths of four Feshbach resonances are determined. The method is largely insensitive to magnetic-field noise and is applicable to very narrow Feshbach resonances.

Using fast magnetic-field pulses instead of linear ramps, mono-energetic pairs of atoms are created. For Feshbach resonances with an s-wave bound state, the outgoing wavefunction is spherically symmetric. However, at a Feshbach resonance near 632 G which is caused by a d-wave bound state, we populate outgoing s and d waves. The measured dissociation rate shows a significant increase due to a d-wave shape resonance. The position and the width of the shape resonance are extracted from the data. For understanding our experimental observations, new theory is developed.

Finally, the thesis reports on an experiment in which we prepare a quantum state with one molecule at each site of an optical lattice. Our technique relies on the creation of an atomic Mott insulator with exactly two atoms at each lattice site at the core of the cloud. A magnetic-field ramp across the Feshbach resonance at 1007.4 G associates the atom pairs to molecules. The method does not depend on the interaction properties of the molecules and is therefore applicable to many systems.

Zusammenfassung

Die vorliegende Arbeit beschreibt Experimente mit zweiatomigen Molekülen, welche mittels magnetisch-induzierter Feshbach-Resonanzen aus ultrakalten ^{87}Rb-Atomen assoziiert werden. Dabei konvertiert eine langsame Magnetfelrampe über eine Feshbach-Resonanz hinweg ein Atompaar in ein gebundenes Molekül. Bei dem Prozess handelt es sich um eine Art Superchemie: die Reaktion läuft reversibel und kohärent ab. Es wird keine latente Wärme freigesetzt, so dass die Feshbach-Moleküle so kalt sind wie die anfänglich vorhandenen Atome.

Das erste der hier beschriebenen Experimente charakterisiert die breiteste der bekannten Feshbach-Resonanzen in ^{87}Rb. Dazu wird die Expansion eines atomaren Bose-Einstein-Kondensates nahe der Resonanz untersucht und die Streulänge als Funktion des Magnetfeldes extrahiert. Die so bestimmte Position liegt bei 1007.4 G, die gemessene Breite beträgt 200 mG.

Anschließend wird diese Feshbach-Resonanz zur Assoziation von ultrakalten Molekülen aus einem Bose-Einstein-Kondensat benutzt. Der Nachweis der Moleküle erfolgt mit Hilfe einer Stern-Gerlach-Methode. Diese liefert das magnetische Moment der Moleküle, welches aufgrund einer vermiedenen Kreuzung zwischen zwei Molekülzuständen bei einem Magnetfeld von 1001.7 G das Vorzeichen wechselt. Durch Anlegen eines Magnetfeldgradienten entsteht deshalb eine eindimensionale harmonische Falle für die Moleküle. Die entprechende harmonische Oszillation der Molekülwolke wird im Experiment beobachtet.

In einem nächsten Experiment wird die Dissoziation der Feshbach-Moleküle durch lineare Magnetfeldrampen untersucht. Aus der freigesetzten kinetischen Energie wird die Breite von vier verschiedenen Feshbach-Resonanzen bestimmt. Die Methode ist weitgehend unempfindlich gegen Magnetfeldrauschen und kann deshalb auch für sehr schmale Resonanzen verwendet werden.

Werden statt linearer Rampen schnelle Magnetfeldpulse zur Dissoziation verwendet, entstehen mono-energetische Atompaare. Im Fall von Feshbach-Resonanzen mit einem gebundenen s-Wellenzustand ist die Wellenfunktion der Atompaare sphärisch symmetrisch. Verwendet man hingegen eine Feshbach-Resonanz bei 632 G mit einem gebundenen d-Wellenzustand, werden zusätzlich auslaufende d-Wellen bevölkert. Die Dissoziationsrate der Moleküle zeigt eine signifikante Erhöhung aufgrund einer sogenannten Form-Resonanz (shape resonance). Position und Breite der Form-Resonanz ergeben sich aus den Daten. Ein neu entwickeltes theoretisches Model erklärt die experimentellen Beobachtungen.

Im letzten hier beschriebenen Experiment wird ein Quantenzustand mit einem Molekül an jedem Gitterplatz eines optischen Gitters erzeugt. Die Technik basiert auf der Erzeugung eines atomaren Mott-Isolators mit genau zwei Atomen an jedem Gitterplatz im Zentrum der Wolke. Eine Magnetfeldrampe über die Feshbach-Resonanz bei 1007.4 G assoziiert anschließend die Atome zu Molekülen. Die Methode hängt nicht von den Stoßeigenschaften der Moleküle ab und ist deshalb in vielen Systemen anwendbar.

Contents

Chapter 1

Introduction

This introductory chapter puts the present work into the context of the field of ultracold quantum gases. After some general remarks on Bose-Einstein condensation and the early years of research on these fascinating quantum objects, the developments in recent years are presented, with special emphasis on Feshbach resonances and ultracold molecules. The introduction ends with a discussion of the contents and the relevance of this thesis work.

1.1 Ultracold quantum gases

The field of ultracold quantum gases emerged in 1995 when three groups independently realized Bose-Einstein condensation in dilute atomic vapors of ^{87}Rb [1], ^{7}Li [2] and ^{23}Na [3]. A series of spectacular experiments followed that revealed the fascinating nature of these Bose-Einstein condensates (BECs).

Bose-Einstein condensation is a quantum statistical effect. It occurs in an ideal gas of indistinguishable bosons at extremely low temperatures when the thermal de-Broglie wavelength of the particles becomes comparable to the inter-particle distance. Below a critical temperature, the wavefunctions of the particles start to overlap and a macroscopic number of particles condenses into the single-particle ground-state of the system. A macroscopic matter wave forms.

The first prediction of Bose-Einstein condensation dates back to the year 1925 when A. Einstein wrote his seminal paper [4] based on the findings in a paper by N. Bose [5]. In the following decades, the connection between superfluidity in liquid ^{4}He and the occurrence of Bose-Einstein condensation could be established [6, 7]. To some degree, superconductivity in metals could also be linked to Bose-Einstein condensation. However, in all the systems studied before 1995, the interactions between particles made a quantitative comparison with the ideal-gas theory difficult.

In contrast, condensation of dilute gases comes very close to the ideal-gas case. This allows a theoretical description from first principles. Interactions between the atoms due to elastic collisions are treated in a mean-field approach, where interaction-induced correlations between the particles are neglected.

Today, close to a hundred experiments worldwide routinely produce Bose-Einstein condensates [8]. Many properties of dilute Bose-condensed gases are well understood by now, thus opening up several avenues for further research. The status of the field about four years ago is summarized in two excellent textbooks [9, 10]. Part of the more recent developments will be discussed in detail in Secs. 1.2 and 1.3.

One trend in fundamental research on ultracold quantum gases is the engineering of more complicated quantum systems. During the past few years, researchers have developed a range of experimental tools to control external and internal degrees of freedom of the atoms in real time. Optical lattices, i.e. artificial crystals of light created by interfering laser beams, are an important example [11]. Quantum gases in optical lattices resemble solid-state systems, but have the advantage of experimentally adjustable parameters. Hence, the hope is to engineer artificial condensed-matter systems in order to simulate open questions from solid-state physics [12].

Besides studying Bose-condensed gases, there is a strong motivation for investigating the properties of fermionic quantum gases. This field was pioneered by Debbie Jin at JILA in Boulder, Colorado. Her group applied and adapted the techniques of laser cooling and evaporative cooling known from the experiments on Bose-Einstein condensation to a gas of fermionic ^{40}K atoms. In 1999, the group reached the regime of quantum degeneracy [13]. Since then, the number of groups studying fermionic quantum gases and also mixtures between bosons and fermions has grown continuously [8].

1.2 Feshbach resonances

Collisions between particles are crucial for the physics of ultracold quantum gases. The creation of a degenerate quantum gas by evaporative cooling relies on a favorable ratio between elastic and inelastic collisional cross sections. Furthermore, elastic interactions determine the static and dynamic properties of dilute Bose-Einstein condensates. Hence, controlling the elastic interactions between atoms could open the door to exciting experiments and is certainly an experimenter's dream. Magnetically-tunable Feshbach resonances offer this possibility.

A Feshbach resonance is a scattering resonance, which occurs if two colliding particles couple resonantly to a bound state. The concept of a Feshbach resonance was first introduced in the context of nuclear physics [14, 15]. There a Feshbach resonance is probed by tuning the energy of the colliding particles. In ultracold gases, however, the collision energy is fixed. Here the resonance condition can be met by inducing a relative energy shift between free and bound state with an external static magnetic field. Magnetic tuning of collisional properties for cold gases was initially discussed in terms of inelastic collisions and trap loss [16, 17]. In 1993, the group of Boudewijn Verhaar in Eindhoven proposed to change the elastic scattering properties by means of a magnetically tunable Feshbach resonance [18].

A few years later in 1998, four groups independently observed Feshbach resonances in ^{23}Na, ^{85}Rb, and ^{133}Cs [19–22]. While clearly demonstrating the desired influence on elastic collisions, the experiments also revealed the simultaneous enhancement of inelastic processes near a Feshbach resonance. This was seen as a serious limitation for future experiments and, as a consequence, dampened the interest in Feshbach resonances. Among the few people still working on Feshbach resonances at that time was Carl Wieman. His group performed a series of important experiments using a Feshbach resonance in ^{85}Rb. They employed the Feshbach resonance to produce a stable Bose-Einstein condensate of ^{85}Rb [23]. Furthermore, they induced a controlled collapse of the condensate and carried out a detailed study of the collapse dynamics [24]. By using a Ramsey scheme, the group demonstrated the coherent coupling of the free atomic state to the molecular bound state involved in the Feshbach resonance [25]. This experiment attracted much interest in the community since it was an important step towards the creation of a molecular BEC as first suggested by Timmermans et al. [26, 27].

Meanwhile, several experiments working with fermionic gases had entered the quantum degenerate regime and turned their attention to realizing a superfluid of fermionic atom pairs. The critical temperature for pairing and superfluidity depends on the interaction strength between the atoms. Feshbach resonances were therefore suggested as a means to bring the critical temperature into an experimentally accessible regime [28–30].

This prospect and the hope of creating a molecular BEC motivated a number of groups to implement the technique of magnetically-tunable Feshbach resonances in their experiments. In 2002, Feshbach resonances were reported for ^{40}K [31], ^{6}Li [32, 33], ^{7}Li [34–36] and also for ^{87}Rb [37]. Since then, the number of groups using Feshbach resonances has constantly grown. Today Feshbach resonances are a well-established and widely-used tool in experiments on ultracold quantum gases.

Alternative methods for inducing Feshbach resonances were also put forward. Proposals suggested to replace the static magnetic field with a radio-frequency field [38], a static electric field [39] or a light field [40]. In the case of light, these resonances are called optically induced Feshbach resonances and experiments demonstrated their feasibility [41–43]. However, due to the big success of magnetically-induced Feshbach resonances, these alternatives have not yet attracted as much attention.

1.3 Ultracold molecules

Recent years have witnessed an increasing interest in ultracold molecules. Compared to atoms, molecules have the additional degrees of freedom of rotation and vibration. Moreover, molecules can have a permanent electric dipole moment. These polar molecules are good candidates for high-precision measurements such as the search for an electric dipole moment of the electron [44]. Here, ultracold temperatures would lead to an increase in precision. In addition, the long-range dipole-dipole interaction

would offer the exciting chance to probe new physical regimes in ultracold quantum gases (see e.g. Refs. [45, 46]).

Due to the complicated internal structure of the molecules, laser-cooling strategies developed for alkali atoms do not work in the case of molecules. Hence, alternative cooling methods are needed. Pioneering work was done using cryogenic methods (buffer gas cooling) [47] and a Stark decelerator [48]. Today, more and more methods are proposed and put into practice (see Ref. [49]). However, there is still quite a long way to go in order to reach quantum degeneracy with these methods.

A complementary approach to the cooling methods is the association of molecules from ultracold atoms. The Julienne group first pointed out that a slow magnetic-field ramp across a Feshbach resonance in the right direction would take population into a bound molecular state [50]. This association technique constitutes a form of super-chemistry, where the temporal evolution of the reaction is under complete experimental control. The reaction is fully reversible and adiabatic, i.e. no latent heat is released. Hence, an adiabatic ramp should convert an atomic condensate into a molecular condensate.

In 2003, several groups adapted the ramping technique to associate ultracold molecules from ^{40}K [51], ^{133}Cs [52], ^{87}Rb [53], ^{6}Li [54, 55], and ^{23}Na [56]. Two groups reported the successful creation of molecules based on a slightly different technique. They relied on the formation of dimers by three-body recombination close to the pole of a Feshbach resonance [57, 58]. This is remarkable insofar as under normal conditions, i.e. far from the pole of the Feshbach resonance, three-body recombination leads to undesired loss of atoms.

None of the experiments starting from an atomic BEC managed to produce a BEC of molecules. The reason was the short lifetime of the Feshbach molecules due to inelastic collisions. Measurements in the bosonic systems ^{23}Na, ^{133}Cs, and ^{87}Rb revealed loss-rate coefficients on the order of $10^{-10}\mathrm{cm}^3\mathrm{s}^{-1}$ [59–61]. Far away from the Feshbach resonance, fast loss was also observed in the fermionic systems ^{6}Li and ^{40}K. However, close to the pole of the Feshbach resonance, inelastic molecule collisions are suppressed by several orders of magnitude [54, 57, 62], which was a big surprise. An explanation on the basis of the Pauli exclusion principle was suggested [63].

In November 2003, the groups of Rudi Grimm, Debbie Jin and Wolfgang Ketterle demonstrated Bose-Einstein condensation of molecules [57, 58, 64]. In early 2004, the same groups observed condensation of fermionic atom pairs on the Fermi side of the Feshbach resonance [65–67]. The proof for superfluidity of the condensed pairs was given by the Ketterle group in a spectacular experiment in 2005, in which they demonstrated the creation of vortices [68].

Meanwhile, groups starting from bosonic atoms carried out a range of different experiments with Feshbach molecules. The association process was investigated systematically [69], one- and two-body decay of the molecules was studied [59–61, 70]. Moreover, several groups looked into molecule dissociation by fast magnetic-field ramps [59, 71]. An alternative method for the production of Feshbach molecules

was demonstrated [72]. Experiments on coherent molecular optics were performed [73]. Feshbach molecules were associated at the sites of a three-dimensional optical lattice leading to a considerable increase of the molecule lifetime [74–76]. Very recently, the coherent Raman transfer of Feshbach molecules to the next lower-lying bound state was reported [77].

At the end of this section, another - much older - association technique should be mentioned. Before the potential of Feshbach resonances was realized, photoassociation was the standard method for associating molecules from ultracold atoms [78]. One problem in photoassociation is the spontaneous scattering of photons, which leads to heating. As a consequence, no molecular BEC could be created that way yet.

1.4 This thesis

The experiments described in this thesis were carried out in an apparatus for Bose-Einstein condensation of ^{87}Rb. During the construction of the apparatus, special emphasis was put on a high-flux source of atoms [79] and the stability of the magnetic trap [80]. As a result, the apparatus produces large Bose-Einstein condensates with high reproducibility and a large repetition rate. In addition, ultra-stable homogeneous magnetic fields of up to 1260 G can be created [80]. This enabled the detection of 42 Feshbach resonances, prior to this thesis work [37]. Most of these resonances are too narrow for further applications. The broadest resonance by far is located at $\sim$ 1007.4 G and has a magnetic-field width of 200 mG. This is rather narrow in comparison to typical resonance widths in other alkali atoms. Nevertheless, this particular resonance served as an excellent starting point for the experiments described in this thesis.

An experiment that we performed in the beginning of this PhD work was a measurement of the elastic scattering properties near the 1007-G resonance (Chap. 3). Thereby, we demonstrated the controlled variation of the s-wave scattering length by a significant amount. This was an important result, since most BEC experiments work with ^{87}Rb. At the same time, the measurement revealed the excellent stability and the high resolution of our magnetic field, a prerequisite for further experiments.

Shortly after, we produced ultracold molecules at the 1007-G resonance using slow magnetic-field ramps (Chap. 4). This was one of the first experiments on ultracold chemistry with Feshbach resonances. Unfortunately, the molecules are short lived due to collisional decay and as a consequence no molecular BEC could be obtained in our system.

Next, we turned our attention to the investigation of molecule dissociation by fast magnetic-field ramps. From the kinetic energy released in the dissociation process, the magnetic-field width of the corresponding Feshbach resonance was determined, even in the case of very narrow resonances (Chap. 4). By using a magnetic-field pulse with rectangular shape, we also created a spherical wave of mono-energetic

atom pairs.

A similar technique allowed us to populate higher partial waves near a d-wave Feshbach resonance at 632 G. From the measured molecule dissociation rate, spectroscopic information on a d-wave shape resonance was extracted. Our newly developed theory connects the dissociation experiment to a scattering gedanken experiment, which can be solved by a coupled-channels calculation. Chapter 5 introduces both experiment and theory.

During the last year of this thesis work, a three-dimensional optical lattice was implemented. Using our expertise on Feshbach molecules, we were the first group worldwide to create a Mott-like state of molecules, i.e. a quantum state with exactly one molecule per lattice site. Chapter 6 describes the corresponding experiment. The thesis ends with an Outlook (Chap. 7).

Chapter 2

Experimental setup

Starting point for all the measurements presented in this thesis is a BEC of ^{87}Rb atoms. This chapter briefly describes the procedure for obtaining a BEC and loading it into an optical dipole trap (Sec. 2.1 and Sec. 2.2). A detailed description of the apparatus and its optimization can be found in [79–81]. A technical challenge is the creation of very stable, high magnetic fields on the order of a thousand Gauss, a prerequisite for experiments with Feshbach resonances in ^{87}Rb. Sec. 2.3 briefly describes how such fields are created in our system. More technical details can be found in [80, 82]. The rest of the chapter (Sec. 2.4) is devoted to the implementation and characterization of a three-dimensional optical lattice, which opens up the possibility to perform a new class of experiments [12] with our system.

2.1 Creation of a BEC

The onset of BEC in a gas of indistinguishable bosons is determined by the condition [9, 10]

$$n\lambda_{dB}^3 \gtrsim 2.612 \ , \tag{2.1}$$

where n is the spatial density and $\lambda_{dB} = h/\sqrt{2\pi m k_B T}$ the thermal de-Broglie wavelength of the particles. Starting from a Rb vapor at room temperature, 19 orders of magnitude in phase-space density must be bridged to reach the BEC phase transition. This "phase-space odyssey" is illustrated in Fig. 2.1. First, laser-cooling and trapping techniques like magneto-optical trapping and polarization-gradient cooling [83] are employed. BEC is then reached by evaporative cooling of the magnetically trapped atom cloud [79, 84]. We will now discuss the technical realization of the different stages in our experiment.

2.1.1 Double-MOT system

A scheme of the vacuum system is shown in Fig. 2.2. The apparatus consists of two chambers connected by a differential pumping stage. Each of the chambers

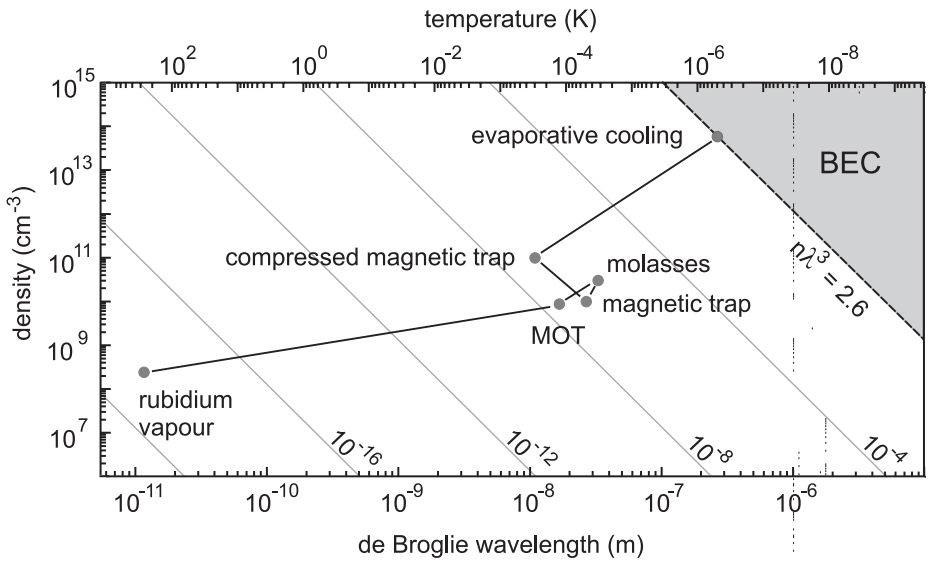

Figure 2.1: Phase-space odyssey. The journey through phase space starts with laser-cooling and trapping techniques. The BEC phase transition is then reached by evaporative cooling.

houses a magneto-optical trap (MOT). The upper MOT serves as an atom source and is optimized for fast loading. It operates at a Rb vapor pressure of $\sim 10^{-8}$ mbar with high loading rates of up to $\sim 5 \times 10^{10}$ s^{-1}. The atoms are transferred to the lower MOT by a short near-resonant laser pulse. The single-shot transfer efficiency is $\sim 15\%$. After 2 s of loading time with 15 transfer shots, typically $\sim 6 \times 10^9$ atoms are collected in the lower MOT. After a short MOT compression phase and subsequent polarization gradient cooling, $\sim 4 \times 10^9$ atoms at temperatures of 40-50 μK are left. The background pressure in the lower part of the apparatus is $\sim 10^{-11}$ mbar. This ensures a low collision rate with background-gas atoms and therefore long lifetimes in the magnetic trap, a prerequisite for reaching the BEC transition.

Fig. 2.3 shows the atomic transitions addressed in the experiment. The MOT beams have a standard σ^+-σ^- configuration. Their frequencies are slightly red-detuned from the cycling transition $5S_{1/2}\, f = 2 \leftrightarrow 5P_{3/2}\, f = 3$. An additional repumping laser resonantly drives the transition $5S_{1/2}\, f = 1 \leftrightarrow 5P_{3/2}\, f = 2$.

All the light addressing the $5S_{1/2}\, f = 2$ state is derived from a single titanium-sapphire laser (Coherent MBR110) with an output power of 1.3 W. The repumping light is provided by a separate diode laser (Toptica DL100) with up to 150 mW of output power. Both lasers are stabilized on atomic transitions using Doppler-free saturation spectroscopy in combination with a Pound-Drever-Hall locking scheme [85].

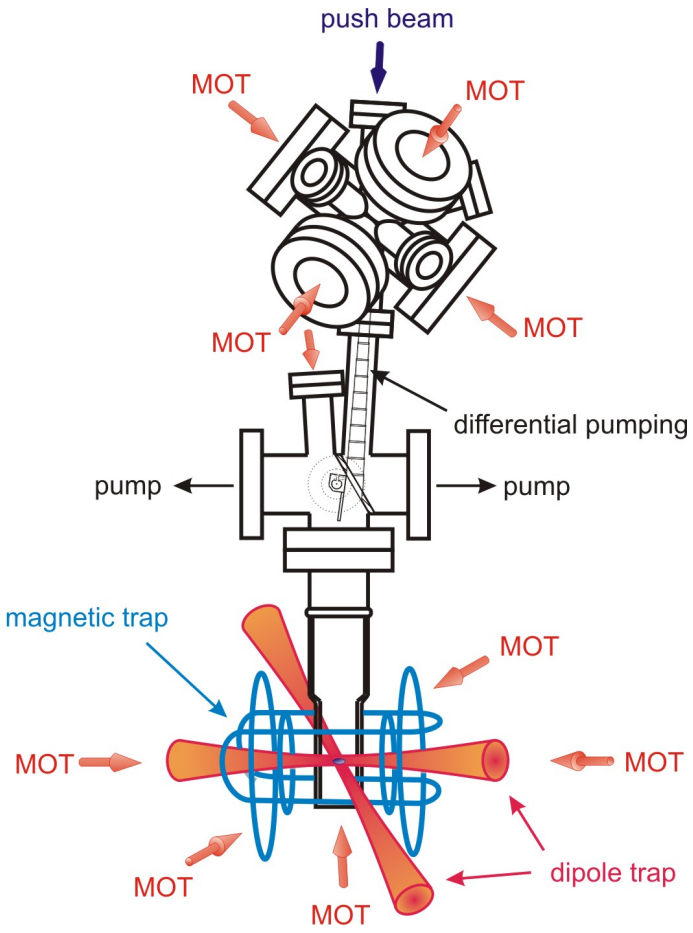

Figure 2.2: Double-MOT system. The vacuum system houses an upper vapor-cell MOT and a lower science MOT in a glass cell. The magnetic trap and the optical dipole trap are also indicated.

2.1.2 Magnetic trap

After polarization gradient cooling and before the transfer to the magnetic trap, the atomic cloud is spin-polarized by optical pumping. Low-field seeking and therefore magnetically-trappable states are $|f, m_f\rangle = |2, 2\rangle$, $|2, 1\rangle$, and $|1, -1\rangle$. The last one is used in the experiment. For optical pumping, a σ^+-polarized and a (much weaker) π-polarized beam resonantly drive the transition $5S_{1/2}\, f = 2 \leftrightarrow 5P_{3/2}\, f = 2$. This transfers roughly 50% of the population into the desired state. Attempts to improve this fraction with another σ^+-polarized laser beam resonant with the transition $5S_{1/2}\, f = 1 \leftrightarrow 5P_{3/2}\, f = 1$ were unsuccessful.

Fig. 2.4 sketches the coil configuration of the magnetic trap. The coils generate a Ioffe-Pritchard field configuration [86]. Four linear rods (the "bars") with alternating current directions generate a two-dimensional quadrupole field, which provides radial confinement. The field of two "pinch" coils confines the atoms along the trap

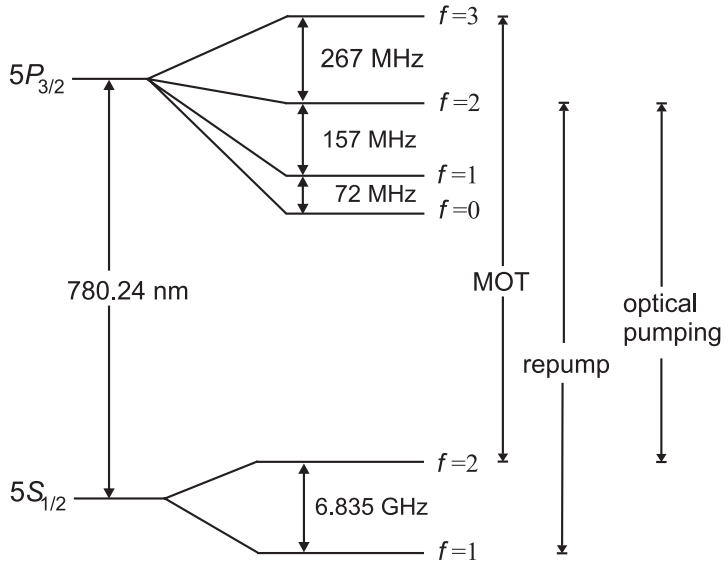

Figure 2.3: Level scheme of ^{87}Rb including hyperfine splitting. Labeled transitions are used in the experiment.

axis. However, the strong center field generated by the pinch coils lowers the radial confinement of the trap. To counteract this, a homogeneous field created by a pair of compensation coils is added in order to reduce the center field to a small value B_0. The finite value B_0 is necessary to suppress Majorana spin flips to non-trappable Zeeman states [87]. The offset-field stability of the magnetic trap is excellent, with a noise value of < 1 mG (rms over 1 hour) [80].

Close to the center, the potential is harmonic in all three dimensions. It is characterized by the radial and axial trap frequencies, ω_r and ω_a, which can be adjusted independently of each other. For efficient loading of the magnetic trap, the trap center position is matched to the position of the atomic cloud after molasses cooling. The trap frequencies are chosen to be $\omega_r = \omega_a = 2\pi \times 8.5\,\mathrm{Hz}$. Together with fast switch-on times of ~ 1 ms, this ensures that the phase-space distribution of the atomic cloud is not significantly altered in the loading process.

2.1.3 Evaporative cooling

The final step for reaching the phase transition to BEC is forced evaporative cooling. The idea is simple: the hottest atoms are selectively removed from the sample. The remaining atoms collide elastically and re-thermalize. As a consequence, the overall temperature decreases. Although atoms are removed from the trap during evaporative cooling, the density in the trap center increases. In combination with

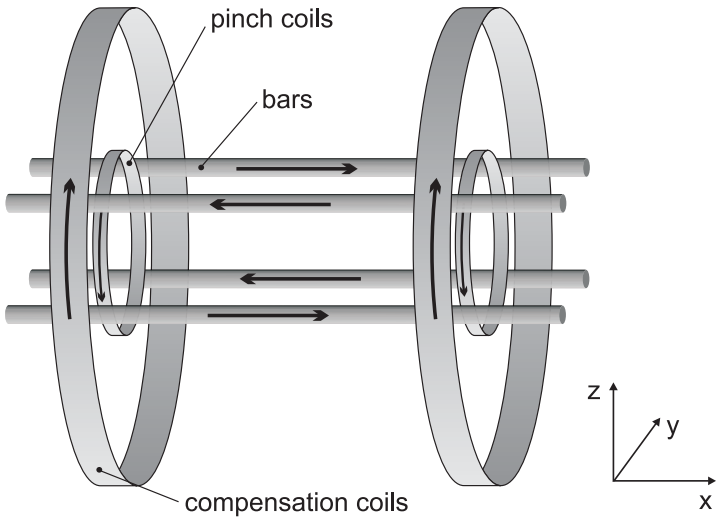

Figure 2.4: Coil configuration of the Ioffe-Pritchard trap. The bars generate a 2D quadrupole field for radial confinement. Along the trap axis, the pinch coils provide harmonic confinement. The compensation coils reduce the magnetic field in the trap center to a small offset field B_0.

the decreasing temperature this means an increase in phase-space density.

In practice, evaporative cooling is implemented by applying a radio-frequency (RF) field to the magnetically trapped cloud. Since the atomic Zeeman energy depends on position, the RF field locally induces transitions to non-trappable Zeeman states, wherever the resonance condition $h\nu_{RF} = m_f g_f \mu_B B(\mathbf{r})$ is satisfied. g_f denotes the Landé factor of the hyperfine state with quantum number f and μ_B Bohr's magneton.

Atoms with a large kinetic energy sample regions of high magnetic field, whereas atoms with a small kinetic energy stay close to the trap center. Hence, a frequency ramp from high to low frequencies continuously removes the hottest atoms from the trap. In the experiment, ν_{RF} is swept from 50 MHz to ~ 2 MHz within 5 s.

For efficient evaporative cooling, the atom cloud is compressed in the magnetic trap before the cooling process. This increases the density and therefore the collision rate. The trap frequencies of the compressed trap are $\omega_a = 2\pi \times 14$ Hz and $\omega_r = 2\pi \times 108$ Hz.

A large fraction of the initial atom cloud is lost during the evaporative cooling. Still, the decrease in temperature and simultaneous increase in peak density bring the system across the phase transition to Bose-Einstein condensation. Typically, a BEC of $\sim 2 \times 10^6$ atoms in the state $|f, m_f\rangle = |1, -1\rangle$ is produced. The remaining thermal fraction has a temperature of some hundred nK.

2.1.4 Detection

Absorption imaging is used for the detection of the atomic density distribution [79]. A near-resonant laser beam propagates along the imaging axis (y axis in Fig. 2.4). The atom cloud absorbs part of the light and casts a shadow in the beam, which is imaged onto a CCD camera. The light is near-resonant with a closed-cycling transition of the atoms, so that one atom can scatter many photons and thus create a large signal. An analogous technique could in principle be applied to molecules, too. But the absence of closed-cycling transitions in molecules would lead to a very small signal.

From the recorded two-dimensional intensity distribution $I_t(x, z)$, the atomic column density $\tilde{n}(x, z) = \int n(\mathbf{r})\, \mathrm{d}y$ can be extracted according to Beer's law. For an incident intensity $I_0(x, z)$ well below the saturation intensity of the atomic transition one obtains

$$\tilde{n}(x, z) = \frac{1}{\sigma_{abs}} \ln \frac{I_0(x, z)}{I_t(x, z)} \ , \tag{2.2}$$

where σ_{abs} is the cross section for the absorption of a photon by an atom.

Before imaging, the atomic cloud is released from the magnetic trap or the dipole trap and is allowed to fall and expand freely for 2-20 ms (time-of-flight method). For a cloud in the collision-less regime, where the interaction energy between atoms is negligible, the cloud expands freely and the spatial distribution after a long expansion time reflects the initial in-trap momentum distribution. This is typically the case for a purely thermal cloud. For high enough densities, as for example realized in a BEC, the interaction energy between atoms due to elastic collisions plays a crucial role and affects the expansion dynamics [10, 88, 89].

Absorption imaging is a destructive detection method. After an image has been taken, a new experimental cycle is started. Hence for reliable quantitative measurements, a good reproducibility and a high repetition rate of the apparatus are desirable. With the ultrastable magnetic trap and an overall cycle time of ~ 15 s, these conditions are well satisfied for our system.

2.1.5 Phase transition

The onset of BEC is marked by a characteristic change in the atomic density distribution. For a thermal cloud above the critical temperature T_c for condensation, the in-trap distribution is to a good approximation Gaussian in position and momentum. As a consequence, the thermal cloud expands isotropically with Gaussian envelope [Fig. 2.5(a)].

Just below T_c, a significant number of particles occupies the ground state of the trapping potential. A cold and dense core appears in the center of the atomic cloud resulting in a typical bimodal density distribution [Fig. 2.5(b)].

Well below T_c, a large fraction of atoms is condensed and the condensate peak is very pronounced. [Fig. 2.5(c)]. For a harmonic potential, the condensate density

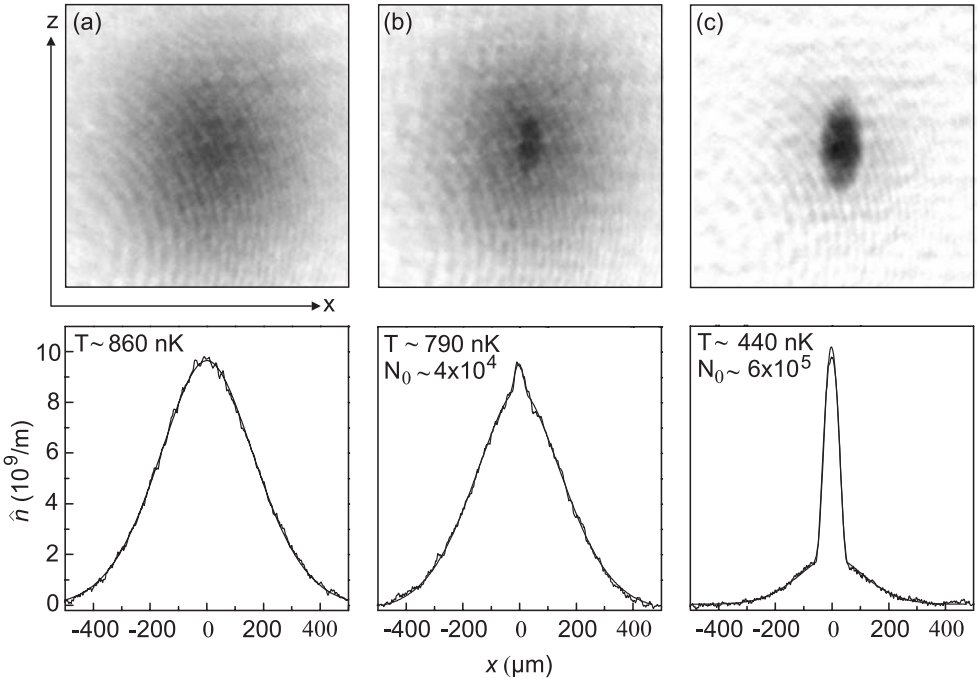

Figure 2.5: Absorption images of an expanding atom cloud taken 20 ms after the release from the magnetic trap. The corresponding integrated density profiles $\hat{n}(x) = \int \tilde{n}(x,z)\mathrm{d}z$ are also shown. (a) Slightly above T_c, the atomic cloud is purely thermal. (b) Slightly below the critical temperature, a small condensate peak can be identified. N_0 denotes the number of condensate atoms. (c) Well below T_c, a large fraction of the atoms is condensed, resulting in the characteristic parabolic density distribution of a harmonically trapped condensate.

distribution is parabolic. During expansion, the parabolic shape of the cloud is preserved but its aspect ratio is inverted [10, 88, 89]. Chap. 3.3.1 discusses the BEC expansion dynamics in more detail.

2.2 Optical dipole trap

The Feshbach resonances studied in this thesis occur for atoms in the hyperfine state $|f, m_f\rangle = |1, +1\rangle$. This state cannot be held in a magnetic trap. Hence, an optical dipole trap is used. In this section, the concept of dipole trapping is explained and the technical realization in the experiment is discussed. For a comprehensive review of dipole trapping the reader is referred to [90].

2.2.1 Optical dipole potential

When an atom is exposed to laser light, the oscillating electric field **E** induces an oscillating electric dipole moment

$$\mathbf{d} = \alpha(\omega)\mathbf{E} \ , \tag{2.3}$$

where $\alpha(\omega)$ is the frequency-dependent complex polarizability of the atom. The potential energy of the induced dipole moment **d** in the external field **E** is given by

$$V_{dip} = -\frac{1}{2}\left\langle \mathbf{d}\cdot\mathbf{E}\right\rangle_t = -\frac{1}{2\epsilon_0 c}\,\mathrm{Re}(\alpha) I \ \ , \tag{2.4}$$

where $\langle\cdots\rangle_t$ denotes the time average over rapidly oscillating terms. Hence, the dipole potential V_{dip} is proportional to the intensity of the light field I and to the real part of the polarizability $\mathrm{Re}(\alpha)$, which describes the component of **d** oscillating in phase with **E**. In addition, the oscillating dipole **d** absorbs (and subsequently re-emits) power due to its out-of-phase component. The resulting photon scattering rate turns out to be proportional to the imaginary part of $\alpha(\omega)$ and to the laser intensity.

The polarizability $\alpha(\omega)$ can be calculated in the classical Lorentz model. This treatment turns out to give fairly accurate results in special cases. A more detailed description treats the atom as a quantum-mechanical two-level system. The classical light field leads to a shift V_{dip} in the ground-state energy of the atom, the AC-Stark shift [83, 90].

Treating the atom as a two-level system, simple formulas for the dipole potential V_{dip} and the photon scattering rate Γ_{sc} can be derived [90]

$$V_{dip}(\mathbf{r}) = -\frac{3\pi c^2\Gamma_{sp}}{2\omega_0^3}\left(\frac{1}{\omega_0-\omega}+\frac{1}{\omega_0+\omega}\right) I(\mathbf{r}) \sim \frac{3\pi c^2\Gamma_{sp}}{2\omega_0^3}\frac{I(\mathbf{r})}{\Delta} \tag{2.5}$$

$$\Gamma_{sc}(\mathbf{r}) = \frac{3\pi c^2\Gamma_{sp}^2}{2\hbar\omega_0^3}\left(\frac{\omega}{\omega_0}\right)^3\left(\frac{1}{\omega_0-\omega}+\frac{1}{\omega_0+\omega}\right)^2 I(\mathbf{r}) \sim \frac{3\pi c^2\Gamma_{sp}^2}{2\hbar\omega_0^3}\frac{I(\mathbf{r})}{\Delta^2} \ . \tag{2.6}$$

$\Delta = \omega - \omega_0$ denotes the detuning of the angular frequency ω of the light with respect to the atomic resonance ω_0. Γ_{sp} is the spontaneous decay rate of the excited state of the atom. For ^{87}Rb, the spontaneous emission rate is $\Gamma_{sp} = 2\pi \times 6$ MHz. The above formulas are valid for a detuning which is large compared to the fine-structure splitting. The approximations on the right-hand side of Eqs. (2.5) and (2.6) are appropriate if $\omega_0 - \omega \ll \omega_0 + \omega$. In this case, the Bloch-Siegert shift [91] is negligible.

Eqs. (2.5) and (2.6) reveal the basic principles of dipole trapping. The sign of Δ determines the sign of V_{dip}: in a red-detuned beam ($\Delta < 0$) atoms will be attracted to regions of maximum intensity. At a given potential depth, the photon scattering rate and the corresponding heating rate can be minimized by choosing large detuning and high intensity.

2.2.2 Technical realization

A Gaussian laser beam of power P and waist w_0 has an intensity profile [92]

$$I(r,z) = \frac{2P}{\pi w^2(z)} e^{-2r^2/w^2(z)} \ , \tag{2.7}$$

where $w(z) = w_0\sqrt{1+(z/z_R)^2}$ is the $1/e^2$ radius of the intensity and $z_R = \pi w_0^2/\lambda$ the Rayleigh-length. λ is the wavelength of the laser light. A red-detuned Gaussian beam forms a cylindrically symmetric atom trap. Close to the center, the trapping potential is approximately harmonic with radial and longitudinal angular trap frequencies

$$\omega_r = \sqrt{\frac{4V_0}{mw_0^2}} \qquad \text{and} \qquad \omega_z = \sqrt{\frac{2V_0}{mz_R^2}} \ , \tag{2.8}$$

where m is the mass of an atom. The trap depth V_0 can be calculated using Eq. (2.5). For a single-beam trap, the confinement along z is weak compared to the radial direction, i.e. $\omega_z \ll \omega_r$. In order to have similar confinement in all directions, a crossed dipole trap consisting of two intersecting Gaussian laser beams is used.

In most of the experiments presented here, the light for the dipole trap is provided by a single Nd:YAG laser (Innolight Mephisto 2000). It delivers up to 2 W of output power in single-frequency operation at a wavelength of 1064 nm. The two beams forming the crossed dipole trap have mutually orthogonal linear polarization to minimize interference effects. One beam propagates along the magnetic-trap axis, while the second beam propagates orthogonally to the first beam and subtends an angle of 25° with the horizontal plane. Depending on the particular experiment, beam waists and powers were adjusted. Typical numbers are 50 μm for the waists and 50 to 100 mW for the laser power per beam. Exact numbers are given when presenting experimental results. The trap frequencies $(\omega_x, \omega_y, \omega_z)$ were measured by parametric heating [93, 94]. In our setup, the geometric mean of the trap frequencies $\bar{\omega} = (\omega_x\omega_y\omega_z)^{1/3}$ is typically on the order of $2\pi \times 100$ Hz.

The dipole trap is loaded from the magnetic trap and can typically hold a BEC of up to $\sim 5 \times 10^5$ atoms. In order to prevent spin flips to other Zeeman states in the dipole trap, a weak magnetic guiding field of ~ 1 G parallel to the center field of the magnetic trap is applied.

2.3 Magnetic fields

For the Feshbach resonances in ^{87}Rb, the ratio of magnetic field width to resonance position is on the order of 10^{-4} or smaller. As a consequence, the magnetic fields for addressing the Feshbach resonances must be stabilized very accurately. At the same time, fast magnetic-field ramps close to resonance are necessary for the experiments on molecule creation and dissociation.

Two separate pairs of coils create the magnetic field. The compensation coils of the magnetic trap serve as a first pair of coils. They produce a strong homogeneous background field. Four power supplies (Agilent 6690A) drive the coils at a total current of up to 1760 A. Sophisticated servo electronics keep the magnetic-field noise caused by current fluctuations below 4 mG (rms). The field magnitude is calibrated using microwave spectroscopy: from the measured frequency of microwave transitions between hyperfine levels, the magnetic field at the location of the atoms can be inferred using the Breit-Rabi formula [95]. The direction of the field is chosen such that it is opposite to the center field of the magnetic trap and the weak guiding field in the dipole trap. Atoms which were in the state $|f, m_f\rangle = |1, -1\rangle$ in the dipole trap are transferred to the desired state $|1, +1\rangle$ with nearly 100% efficiency by rapidly switching on the strong field (typically in ~ 2 ms).

Two additional coils create a magnetic field of a few Gauss, which is added to the strong background field. The coils are made of thin copper wire and have six windings each. Their diameter is small compared to the diameter of the compensation coils. This minimizes mutual inductance effects between the two pairs of coils. Due to their small self-inductance of a few μH, the additional coils allow fast and accurate ramps, with ramp speeds of up to 1 G/μs. The servo loop for these coils is so fast that its step response has a settling time of ~ 1 μs.

2.4 Optical lattice

An optical lattice is a regular array of dipole traps formed by standing-wave light fields (see e.g. Ref. [96]). The periodic lattice potential leads to a situation similar to that of crystal lattices in condensed matter systems, resulting e.g. in a band structure of the lattice energy levels. However, in contrast to condensed-matter systems most parameters of the optical lattice are freely adjustable and can be changed in real time. In this section, the theoretical basics of optical lattices are introduced (Sec. 2.4.1 and 2.4.2). For the three-dimensional optical lattice implemented in our apparatus, details of the setup and the characterization are given (Sec. 2.4.3 and 2.4.4).

2.4.1 Periodic lattice potentials

Retro-reflecting a Gaussian laser beam is the easiest way to create a periodic array of dipole traps (see Fig. 2.6). The intensity distribution of such a one-dimensional standing wave is given by

$$I(\mathbf{r}) = \frac{8P}{\pi w^2(z)} e^{-2r^2/w^2(z)} \cdot \cos^2(k_{lat} z) \ . \tag{2.9}$$

$k_{lat} = 2\pi/\lambda_{lat}$ is the modulus of the wave vector. The dipole potential on the beam axis can be written as

$$V(z) = -V_{lat} \cos^2(k_{lat} z) \ . \tag{2.10}$$

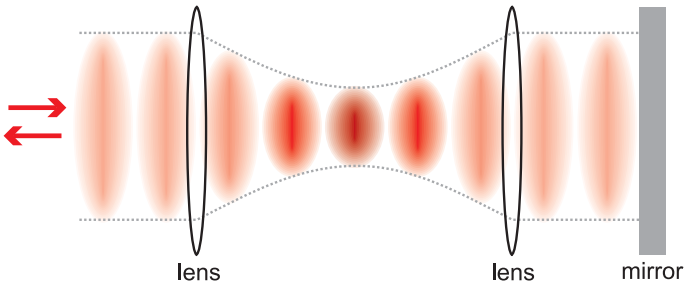

Figure 2.6: A retro-reflected Gaussian beam forms a standing wave pattern.

The lattice depth V_{lat} can be calculated from Eq. (2.5). For simplicity, the Bloch-Siegert shift is neglected in the following. A convenient and widely used energy unit for lattice experiments is the atomic recoil energy $E_{rec} = \hbar^2 k_{lat}^2/2m$, the kinetic energy transferred to an atom at rest due to the momentum kick by an absorbed or emitted lattice photon. In terms of recoil energy the lattice depth then reads

$$\frac{V_{lat}}{E_{rec}} = -\frac{3mc^2}{\hbar^2 k_{lat}^2 \omega_0^3}\frac{8P}{w_0^2}\frac{\Gamma}{\Delta} \ . \tag{2.11}$$

Multidimensional periodic dipole potentials can be formed by superimposing several one-dimensional standing waves. In general, the overall potential is not simply the sum of the single-beam potentials. Additional terms due to interference effects between the beams have to be taken into account. As an example, consider two beams propagating along the y and z axis with linear polarization vectors $\mathbf{e}_y$ and $\mathbf{e}_z$ and a (generally time-dependent) relative phase ϕ. The resulting interference term is proportional to

$$2\mathbf{e}_y \cdot \mathbf{e}_z \cos\phi \cos(k_{lat} y) \cos(k_{lat} z) \ . \tag{2.12}$$

Depending on the relative phase and the polarizations of the two beams, checkerboard-like lattice structures can be realized [97]. However, in order to create simple cubic lattices as in our experiment, the interference term must be minimized. In practice, we eliminate it by choosing the polarizations to be orthogonal and by detuning the frequencies of the two beams with respect to each other, typically by some tens of MHz, so that the relative phase varies rapidly and the interference term averages to zero on the time scale of the atomic motion (typically some tens of kHz).

The resulting 3D simple cubic lattice structure of the potential landscape is sketched in Fig. 2.7. The three standing waves with Gaussian envelope intersect at right angles and thereby form the lattice potential

$$V(\mathbf{r}) = -V_{lat}\left[e^{-2\frac{y^2+z^2}{w_{0x}^2}}\cos^2(k_{lat}x) + e^{-2\frac{x^2+z^2}{w_{0y}^2}}\cos^2(k_{lat}y) + e^{-2\frac{x^2+y^2}{w_{0z}^2}}\cos^2(k_{lat}z)\right] . \tag{2.13}$$

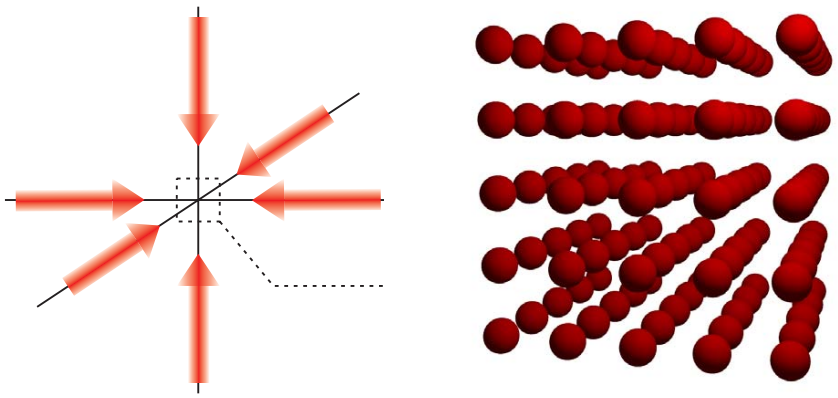

Figure 2.7: 3D simple cubic lattice. At the intersection of three mutually orthogonal standing light waves, a potential landscape with simple cubic lattice structure of its minima forms. Each sphere represents a potential minimum.

Here, we have chosen the lattice depths in all three standing waves to be equal which is also the case in the experiment. w_{0x}, w_{0y}, w_{0z} are the beam waists of the three lattice beams. Usually, the beam diameters are large compared to the size of the atomic cloud loaded into the optical lattice. As a consequence, the most relevant characteristics of the 3D lattice potential can be described by the pseudo-potential

$$V(\mathbf{r}) = -V_{lat}\left[\cos^2(k_{lat}x) + \cos^2(k_{lat}y) + \cos^2(k_{lat}z)\right] - \frac{m}{2}\left(\omega_x^2 x^2 + \omega_y^2 y^2 + \omega_z^2 z^2\right) \ . \tag{2.14}$$

Here, the confinement due to the Gaussian lattice beam shapes is approximated by a harmonic confinement with effective angular trap frequencies

$$\omega_x^2 = \frac{4V_{lat}}{m}\left(\frac{1}{w_{0y}^2} + \frac{1}{w_{0z}^2}\right) \ , \quad \omega_y, \omega_z \text{ by cyclic permutation.} \tag{2.15}$$

Each individual lattice site forms an approximately harmonic potential close to its center, with an angular trapping frequency

$$\omega_{lat} = \sqrt{2\frac{V_{lat}k_{lat}^2}{m}} \ . \tag{2.16}$$

2.4.2 Band structure

The periodic structure of the optical lattice potential $V(\mathbf{r})$ leads to energy bands just like for crystal structures in condensed matter systems. Since the 3D potential is created by three independent standing waves, the problem is fully separable and

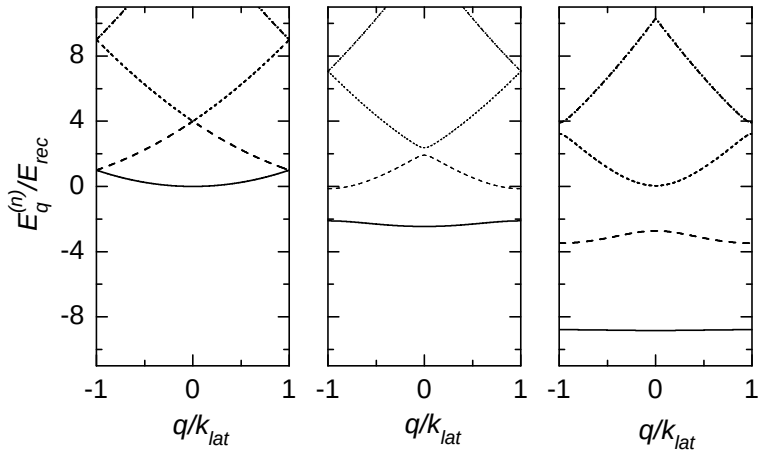

Figure 2.8: Band structure of a one-dimensional optical lattice. The graphs correspond to lattice depths of $V_{lat} = 0, 4, \text{and } 12E_{rec}$ (from left to right). With increasing lattice depth, the band gaps increase and the bands flatten.

it suffices to solve the one-dimensional Schrödinger equation

$$\left[-\frac{\hbar^2}{2m}\partial_x^2 + V(x)\right]\Psi_q^{(n)}(x) = E_q^{(n)} \ . \tag{2.17}$$

Here, $\hbar q$ is the quasi-momentum and n labels the different solutions of Eq. (2.17) corresponding to the different lattice "bands". According to Bloch's theorem the wavefunction can be written as [98]

$$\Psi_q^{(n)}(x) = e^{iqx} \cdot u_q^{(n)}(x) \ , \tag{2.18}$$

where $u_q^{(n)}$ has the same periodicity, $\lambda_{lat}/2 = \pi/k_{lat}$, as the periodic lattice potential $V(x)$. Hence, we can write the wavefunction $\Psi_q^{(n)}(x)$ as a Fourier sum

$$\Psi_q^{(n)}(x) = \sum_s c_s^q e^{i(q+2sk_{lat})x} \ . \tag{2.19}$$

The Fourier decomposition of $V(x)$ is easily written down

$$V(x) = -V_{lat}\cos^2(k_{lat}x) = -V_{lat}\frac{1}{4}\left(2 + e^{2ik_{lat}x} + e^{-2ik_{lat}x}\right) \ . \tag{2.20}$$

By inserting Eqs. (2.19) and (2.20) into Eq. (2.17), one arrives at the following equation which is satisfied for each Fourier component separately

$$\left[\frac{\hbar^2}{2m}(q + 2sk_{lat})^2 - E_q^{(n)} - \frac{V_{lat}}{2}\right]c_s - \frac{V_{lat}}{4}c_{s+1} - \frac{V_{lat}}{4}c_{s-1} = 0 \ . \tag{2.21}$$

The periodicity of the problem implies that the solutions for all $q' = q + r \cdot 2k_{lat}\,(r \in \mathbb{Z})$ are identical. Hence, it is sufficient to solve Eq. (2.21) inside the first Brillouin zone, i.e. for $-k_{lat} \leq q \leq k_{lat}$. The Fourier coefficients c_s decrease quadratically with the modulus of s. Hence, the Fourier series can be truncated at some point and one obtains a finite set of linear equations for the c_s. The energy eigenvalues are then obtained by setting the determinant of its matrix representation to zero. Fig. 2.8 shows calculated band structures for different lattice depths.

2.4.3 Setup of the optical lattice

The light for the three beams forming the optical lattice is provided by a titanium-sapphire laser (Coherent MBR110), which delivers up to 1.9 W of output power at a wavelength of 830 nm. The laser is frequency-stabilized onto an internal reference cavity, which results in a measured rms line width on the order of 100 kHz (measured on a time scale of 10 ms at a bandwidth of 50 kHz).

The setup of one lattice beam is schematically shown in Fig. 2.9. The light from the titanium-sapphire laser is split into three beams of typically 450 mW each. The power in each beam is controlled separately with acousto-optic modulators (AOMs) and mechanical shutters. To eliminate any interference effects between the beams (see Sec. 2.4.1), the AOM frequencies are detuned with respect to each other by 40-200 MHz. Three separate optical fibers guide the beams to the experiment.

The beams on the x axis (along the magnetic trap axis) and the y axis (along the imaging axis) intersect at right angles. The beam along the z axis (vertical) propagates at an angle of 4° with respect to the normal to the x-y plane. Each beam is linearly polarized and the polarizations are chosen orthogonal to each other. Due to the limited optical access, the lattice beams have to be overlapped with the MOT beams using dichroic mirrors. The lattice beams are focussed down to a waist of $w_0 = 135\ \mu$m at the location of the atoms. The Rayleigh length is $z_R = 6.9$ cm. After leaving the glass cell, the beams are collimated again and retro-reflected. All focussing lenses are mounted on 2D translation stages, which allow for alignment perpendicular to the direction of beam propagation.

In the glass cell, the power per lattice beam is up to 200 mW. Due to reflections off the glass cell and losses in optical components, the retro-reflected beams only deliver 60-80% of that power. The Gaussian envelope of the lattice beams creates an additional harmonic confinement. For equal lattice depths V_{lat} in each standing wave and perfectly aligned beams, the corresponding trap frequencies are given by

$$\omega/2\pi = 13\,\mathrm{Hz} \times \sqrt{V_{lat}/E_{rec}} \tag{2.22}$$

in all directions, according to Eq. (2.15).

Coarse alignment of the lattice is done using near-resonant laser light, which is sent through the same fibres as the lattice light. This ensures excellent spatial overlap between lattice light and near-resonant light. By blasting away the atoms trapped in the dipole trap with the near-resonant laser light, the optical elements

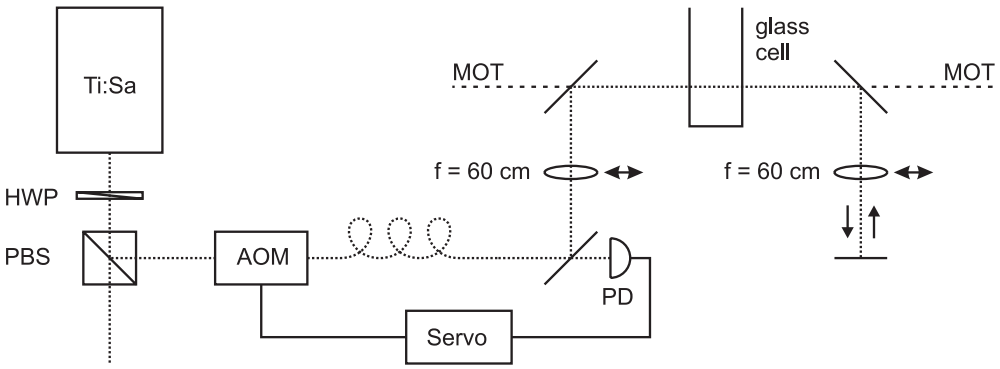

Figure 2.9: Lattice beam setup. Part of the light from the titanium-sapphire laser (Ti:Sa) is divided off using polarization optics (halfwave-plate and polarizing beam splitter) and guided to the experiment through an optical fiber. The focussing lenses for the lattice are mounted on 2D translation stages. Due to limited optical access, the lattice beam has to be overlapped with a MOT beam on a dichroic mirror. Behind the glass cell, another dichroic mirror separates the lattice beam from the MOT beams. The lattice beam is collimated and retroreflected. A feedback loop consisting of an acousto-optic modulator (AOM), a servo, and a photodiode (PD) controls the beam power.

for the lattice light can be adjusted on a coarse level. For fine-alignment, one lattice beam at a time is combined with one dipole trap beam thus forming a crossed dipole trap. At the same time, the retro-reflected beam is blocked. The atom number in this crossed dipole trap serves as a criterion for aligning the lattice beam. Next, the retro-reflected lattice beam is coupled back into the optical fiber. The resulting standing wave is further optimized by using the calibration method described in the next section.

2.4.4 Lattice calibration

In order to interpret any experimental results correctly, the depth of the optical lattice has to be calibrated very carefully. The calibration method should thereby be rather quick and easy-to-use, since the optical lattice requires regular re-alignment and re-calibration due to thermal drifts of the optical components. We adapted the following technique from Ref. [99]: the atoms are released from the optical dipole trap and one lattice beam is pulsed on for a short time. Starting from an atomic cloud at rest, this will create atomic diffraction peaks in time-of-flight images. The population of these peaks reveals the lattice depth.

To understand this process, we note that the 1D lattice potential $-V_{lat}\cos^2(k_{lat}x)$ $= -V_{lat}(2 + e^{-2ik_{lat}x} + e^{2ik_{lat}x})/4$ couples the state $|p = 0\rangle$ to the higher-momentum states $|\pm 2\hbar k_{lat}\rangle$, $|\pm 4\hbar k_{lat}\rangle$, etc. For low enough lattice depths, coupling to $|\pm 4\hbar k_{lat}\rangle$ and higher momenta can be neglected. Using a matrix representation with respect to the momentum state basis $\{|-2\hbar k_{lat}\rangle, |0\rangle, |+2\hbar k_{lat}\rangle\}$, a straightforward calculation shows that the coupling leads to Rabi oscillations of the population in the states $|\pm 2\hbar k_{lat}\rangle$ according to [100]

$$|\langle \pm 2\hbar k_{lat}|\Psi(t)\rangle|^2 \propto \sin^2\left(\frac{\Omega_{lat}}{2}t\right) \propto 1 - \cos\left(\Omega_{lat}t\right)$$
$$\text{with} \qquad \Omega_{lat} = \frac{2}{\hbar}\sqrt{4E_{rec}^2 + \frac{V_{lat}^2}{8}}\ , \tag{2.23}$$

where $\Psi(t)$ is the wave function of the system and Ω_{lat} is the Rabi frequency. A measurement of this population as a function of the lattice pulse duration thus yields V_{lat}.

With this method, V_{lat} is measured for each standing wave separately. Due to imperfect alignment of the beams, the actual lattice depth V_{lat} is typically a factor of ~ 1.5 less than expected from the parameters of the laser beams. Fig. 2.10 shows experimental results for the lattice beam along the magnetic-trap axis (x-axis). Choosing an appropriate time-of-flight, the population in the momentum components $|\pm 2\hbar k_{lat}\rangle$ is clearly visible in the absorption images as diffraction peaks. Besides the discrete diffraction peaks, some of the absorption images show s-wave scattering spheres. They arise due to elastic scattering between atoms in different momentum components [101–103]. Since they appear as non-interfering incoherent background, such scattering spheres can possibly tamper quantitative measurements, e.g. when determining the contrast of a diffraction pattern. However, the scattering spheres can be used to characterize the strength of the standing wave along the imaging axis (y-axis). There, the higher momentum components $|\pm 2\hbar k\rangle$ are not resolved due to the line-of-sight integration by the detection beam. In contrast, the scattering spheres are clearly visible (Fig. 2.10c) and their population also oscillates as a function of pulse duration.

2.4.5 Loading the optical lattice

The BEC is initially trapped in the dipole trap and is loaded into the optical lattice by slowly ramping up the lattice beam powers. The loading must be performed adiabatically in order to populate the ground state of the lattice. Adiabaticity must be ensured with respect to two different processes.

First, population transfer from the lowest Bloch band to higher bands must be avoided. This is a single-atom problem. The adiabaticity criterion is [104]

$$|\langle n, q|d/dt|0, q\rangle| \ll |E_n^{(q)} - E_0^{(q)}|/\hbar\ , \tag{2.24}$$

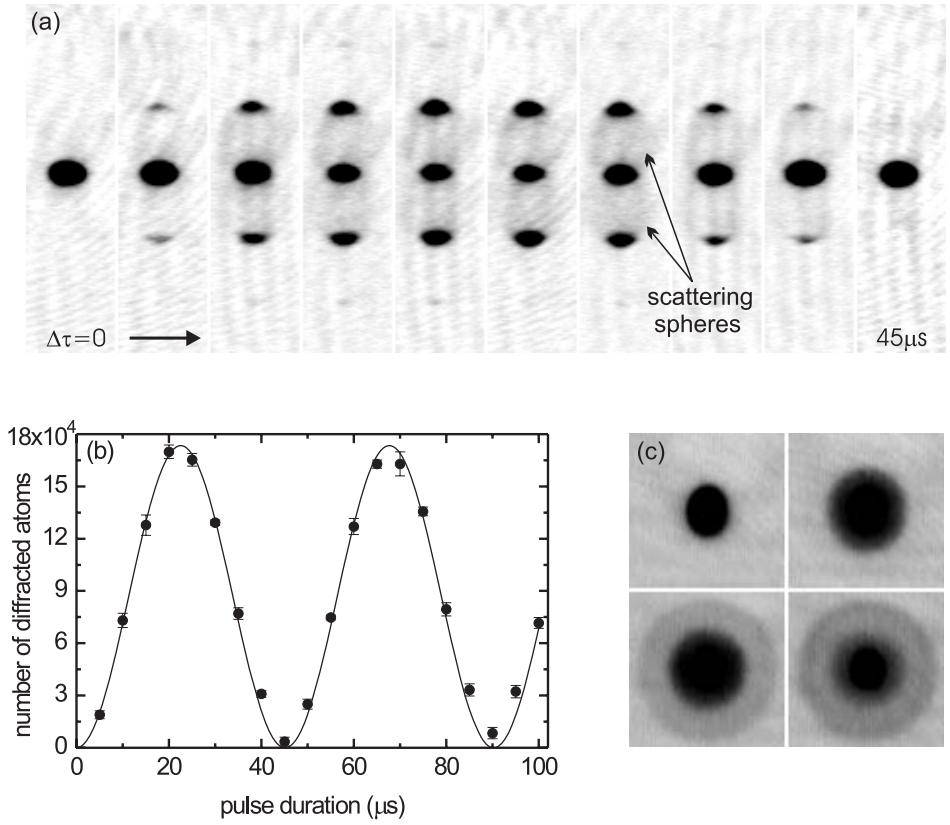

Figure 2.10: Lattice calibration. (a) Immediately after release from the dipole trap, the lattice beam along the magnetic trap axis is pulsed on for a short time. The time-of flight images show diffraction peaks corresponding to the momentum components $|\pm 2\hbar k_{lat}\rangle$. The population in the diffraction peaks oscillates as a function of pulse duration $\Delta\tau$. For the sequence shown, $\Delta\tau$ increases in steps of 5 μs from left to right. In some pictures, s-wave scattering spheres are visible. (b) Number of diffracted atoms as a function of pulse duration for the same lattice parameters as in (a). The dots (•) are experimental data. The fit (line) to the data gives a Rabi frequency Ω_{lat} of $\sim 2\pi \times 22$ kHz, which corresponds to a lattice depth of $\sim 7E_{rec}$. (c) Along the imaging axis, the diffraction peaks at $\pm 2\hbar k_{lat}$ are not visible due to the line-of-sight integration by the detection laser. Instead, the s-wave scattering spheres are quite pronounced and can be used for lattice calibration.

where $|n, q\rangle$ is the Bloch state in the n-th band with quasi momentum q and $E_n^{(q)}$ is the energy of this state. For $V_{lat} \leq E_{rec}$, the spacing between the two lowest bands $E_1^{(0)} - E_0^{(0)} \sim 4E_{rec}$ remains finite for $q \sim 0$. In this case, the adiabaticity criterion can be written as $(d/dt)\, V_{lat}/E_{rec} \ll 32\sqrt{2}E_{rec}/\hbar \sim 9 \times 10^5\,\mathrm{s}^{-1}$ [104]. For deeper lattice potentials, the band spacing increases and the adiabaticity criterion

is fulfilled more easily.

Second, adiabaticity with respect to excitations of the many-body state must be ensured. When the lattice potential is ramped up, the atoms are confined in the lattice sites more strongly and the mean density increases. This causes a larger atom-atom interaction energy. In order to avoid excitations, which lead to a dephasing of the sample, the chemical potential must remain flat. This leads to a redistribution of the atoms for increasing lattice depth. In deep lattice potentials, atom transport is suppressed and the lattice ramp speed must be sufficiently slow to allow for the redistribution. The need for redistribution is partly compensated by the increased harmonic confinement due to the lattice beams at increasing beam powers. The actual dynamics of the sample depends on the detailed experimental conditions and is difficult to quantify. The aspect of many-body adiabaticity will become important in the context of the Mott-insulator phase transition discussed in Chap. 6.

Chapter 3

Atomic scattering near a Feshbach resonance

Magnetically tunable Feshbach resonances offer the possibility to modify and control the scattering properties of ultracold gases in real time. The first part of this chapter presents basic concepts of low-temperature scattering theory and leads up to a discussion of the physics underlying Feshbach resonances. The theoretical introduction is complemented by the presentation of experimental results in the second part of the chapter. By analyzing the mean-field driven expansion of a Bose-Einstein condensate near a Feshbach resonance in ^{87}Rb, the variation of the scattering length a is demonstrated. The results presented here are published in [105].

3.1 Cold collisions

Starting from a time-independent formulation of binary scattering, this section introduces the concept of partial waves and shows that for typical temperatures in ultracold gases the scattering is completely described by a single parameter, the s-wave scattering length. The importance of the scattering length for the static and dynamic properties of a Bose-Einstein condensate is briefly discussed. The reader interested in more details of scattering theory is referred to the literature [106–110].

3.1.1 General remarks

The problem of scattering two particles off one another can be separated into center-of-mass and relative coordinates. The center-of-mass motion is trivial. The problem in the relative motion is equivalent to that of one particle with the reduced mass m_{red} scattering off a potential $V(\mathbf{r})$.

Scattering theory is usually formulated as a time-independent process with an incoming plane wave with wavevector $\mathbf{k}$ pointing along the z-direction and energy $E = \hbar^2 k^2/(2m_{red})$. The corresponding time-independent Schrödinger equation is

given by

$$\left[-\frac{\hbar^2\nabla^2}{2m_{red}} + V(\mathbf{r})\right]\psi_{\mathbf{k}}^{(+)}(\mathbf{r}) \;=\; E\,\psi_{\mathbf{k}}^{(+)}(\mathbf{r}) \quad . \tag{3.1}$$

An appropriate boundary condition for Eq. (3.1) is based on the following argument: Well outside the range of the potential V, the scattering wavefunction $\psi_{\mathbf{k}}^{(+)}$ consists of two parts. The first corresponds to the incoming plane wave, the second is created by the scattering process and falls off radially like a spherical wave. Hence, the wavefunction has the asymptotic form

$$\psi_{\mathbf{k}}^{(+)}(\mathbf{r}) \stackrel{r\to\infty}{\longrightarrow} e^{i\mathbf{kr}} + f(\vartheta,\varphi)\frac{e^{ikr}}{r} \quad , \tag{3.2}$$

where r,ϑ,φ are spherical coordinates. $f(\vartheta,\varphi)$ is the scattering amplitude, which is related to the experimentally accessible differential cross section

$$\frac{d\sigma}{d\Omega} = |f(\vartheta,\varphi)|^2 \quad . \tag{3.3}$$

Here, $d\Omega = \sin\vartheta d\vartheta d\varphi$ is the differential solid angle. The total cross section σ is obtained by integration of the differential cross section over the full solid angle. The task in scattering theory is to determine $f(\vartheta,\varphi)$ for a given potential $V(\mathbf{r})$.

3.1.2 Partial waves

For treating cold collisions theoretically, it is very convenient to switch to an angular momentum basis, i.e. to express the problem in terms of spherical harmonics $Y_{lm_l}(\vartheta,\varphi)$, where l labels the angular momentum with projection m_l along the z-axis. The decomposition of the wavefunction $\psi_{\mathbf{k}}^{(+)}(\mathbf{r})$ then reads

$$\psi_{\mathbf{k}}^{(+)}(r,\vartheta,\varphi) = \sum_{l,m_l}\frac{u_l(r)}{r}Y_{lm_l}(\vartheta,\varphi) \quad , \tag{3.4}$$

The expansion coefficients are written as u_l/r with the radial wavefunctions $u_l(r)$. Inserting Eq. (3.4) into Eq. (3.1) for the special case of a spherically symmetric potential yields a differential equation for the radial part $u_l(r)$

$$\left[-\frac{\hbar^2}{2m_{red}}\frac{d^2}{dr^2} + \frac{\hbar^2 l(l+1)}{2m_{red}r^2} + V(r)\right]u_l(r) \;=\; E\,u_l(r) \quad . \tag{3.5}$$

Besides the scattering potential $V(r)$, this equation contains a repulsive centrifugal term $V_{centr} = \hbar^2 l(l+1)/(2m_{red}r^2)$, which vanishes only for $l = 0$.

Well outside the range of the scattering potential ($r \to \infty$) each radial wavefunction $u_l(r)$ is a superposition of an incoming $\propto e^{-ikr}$ and an outgoing wave $\propto e^{ikr}$.

Since we assume a spherically symmetric potential, the particle flux is conserved for each partial wave separately, i.e. the amplitudes of the incoming and outgoing wave must be the same in magnitude. Hence, the effect of the scattering potential is reduced to a relative phase factor, written as $e^{2i\delta_l}$, where δ_l is real and defined only modulo π

$$u_l(r) \stackrel{r\to\infty}{\longrightarrow} (-1)^{l+1}e^{-ikr} - e^{2i\delta_l}e^{ikr} \quad . \tag{3.6}$$

Inserting Eq. (3.6) into Eq. (3.4) gives an asymptotic formula for $\psi_{\mathbf{k}}^{(+)}(\mathbf{r})$. This is to be compared to the boundary condition (3.2), also expanded in the angular momentum basis. As a result, one can extract an expression for the scattering amplitude f in terms of partial-wave phase shifts δ_l

$$f(\vartheta) = \frac{1}{k}\sum_{l=0}^{\infty}\sqrt{4\pi(2l+1)}e^{i\delta_l}\sin(\delta_l)Y_{l0}(\vartheta) \quad . \tag{3.7}$$

Thus, the scattering problem is now reduced to determining the phase shift δ_l for each partial wave. The corresponding total cross section is given by

$$\sigma = \sum_{l=0}^{\infty}\sigma_l = \frac{4\pi}{k^2}\sum_{l=0}^{\infty}(2l+1)\sin^2\delta_l \quad . \tag{3.8}$$

When determining cross sections, special attention must be paid in the case of indistinguishable particles. The corresponding two-particle wave function has to be properly symmetrized. Since we are dealing with bosons in our experiment, we will restrict the discussion to the scattering of identical bosons. Here, the cross sections double for the even partial waves and vanish for the odd ones [109]

$$\sigma_{boson} = \frac{8\pi}{k^2}\sum_{l\ even}(2l+1)\sin^2\delta_l \quad . \tag{3.9}$$

It is important to notice, that for given k, there is a maximum total cross section of $(2l+1)8\pi/k^2$ for each partial wave, which is called the unitarity limit.

3.1.3 Low-energy scattering

Typical temperatures reached in experiments with ultracold atoms are well below $100\,\mu$K. In this regime, only the s wave, i.e. the partial wave with $l = 0$, is important. This greatly simplifies the description of the scattering process since the only quantity to be determined in Eq. (3.7) is the phase shift δ_0. Qualitatively, this can be understood by observing that for sufficiently low energies the centrifugal barrier V_{centr} in Eq. (3.5) prevents partial waves with $l \neq 0$ from penetrating into the region of the scattering potential V. The higher partial waves do not probe the

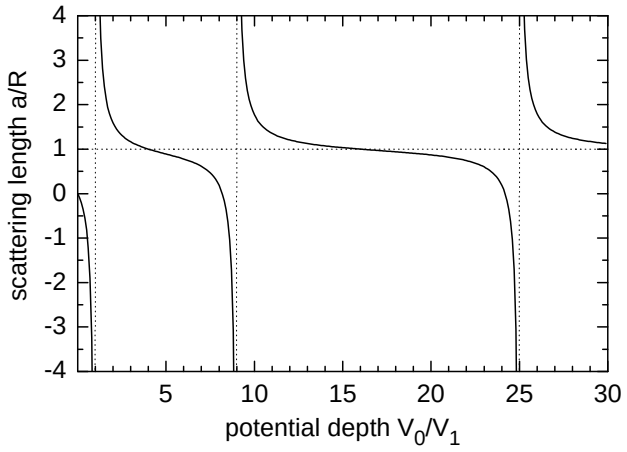

Figure 3.1: Scattering length a as a function of potential depth V_0 for a three-dimensional square-well potential. $V_1 = \pi^2\hbar^2/\left(8m_{red}R^2\right)$ is the potential depth at which the first bound state develops. R is the potential radius. a has a pole whenever a new bound state is supported by the potential.

actual scattering potential. For ^{87}Rb, the d wave contributes significantly around a temperature of 250μK due to a shape resonance behind the centrifugal barrier [111]. Below this temperature, only the s wave is important. The d-wave shape resonance will be discussed in detail in Chap. 5.

For a quantitative analysis, the long-range behavior of the scattering potential plays an essential role. If the potential decreases faster than r^{-3} at large distances, the s-wave phase shift will be proportional to the wavevector k in the limit of vanishing energy, i.e. $\delta_0 \propto k$ for $k \to 0$, and all higher partial-wave phase shifts will vanish even faster [106]. As a consequence, σ becomes constant for sufficiently low energies and the scattering is isotropic. This holds for two ground-state atoms which experience a typical Van-der-Waals potential $\propto r^{-6}$ at large distances.

The low energy behavior of the scattering phase δ_0 motivates the definition of the s-wave scattering length:

$$a = -\lim_{k\to 0}\frac{\tan\delta_0(k)}{k} \quad , \tag{3.10}$$

With this definition the total cross section for bosons in the limit $k \to 0$ can be written as

$$\sigma = 8\pi a^2 \quad . \tag{3.11}$$

For a purely repulsive potential a is positive [106]. However, for an attractive potential the situation is more complex. This point can be clarified by the simple example of a three-dimensional square-well potential

$$V(r) = \begin{cases} -V_0 & r < R, \\ 0 & r > R. \end{cases} \tag{3.12}$$

where $V_0 > 0$ is the potential depth and R is the potential radius. The solution of the Schrödinger equation in the s-wave limit is

$$u_0(r) = \begin{cases} \sin(k'r)\,,\ k' = \sqrt{\frac{2m_{red}(E+V_0)}{\hbar^2}} & r < R, \\ c\sin(kr+\delta_0)\,,\ k = \sqrt{\frac{2m_{red}E}{\hbar^2}} & r > R. \end{cases} \tag{3.13}$$

As a boundary condition, u_0 and du_0/dr have to be matched at $r = R$, thus determining c and δ_0. From the resulting δ_0, the scattering length is calculated using Eq. (3.10)

$$a \;=\; R - \frac{1}{k'}\tan(k'R) \quad . \tag{3.14}$$

This expression is plotted in Fig. 3.1 as a function of V_0. Interestingly, there are poles in $a(V_0)$. Their positions are given by $V_j = V_1(2j-1)^2$, where $V_1 = \pi^2\hbar^2/\left(8m_{red}R^2\right)$ and j is a positive integer. It can be shown that these are exactly the potential depths for which an additional bound state at $E = 0$ develops. Similar poles in a caused by the presence of bound states near $E = 0$ are important when describing Feshbach resonances.

3.1.4 Mean-field description of a BEC

Low-energy scattering plays a key role in describing interactions in cold atomic gases. Typically, these gases are dilute, i.e. interactions are dominated by binary elastic collisions. A dilute system is characterized by a gas parameter $na^3 \ll 1$, where n is the density and a the s-wave scattering length.

In second quantization, the Hamiltonian describing N pairwise interacting bosons confined in an external trapping potential V_{trap} can be written as follows [9, 10]

$$\begin{aligned} \hat{H} \;=\; & \int \mathrm{d}^3r\, \hat{\Psi}^\dagger(\mathbf{r}) \left(-\frac{\hbar^2}{2m}\nabla^2 + V_{trap}(\mathbf{r})\right) \hat{\Psi}(\mathbf{r}) \\ & + \frac{1}{2}\int \mathrm{d}^3r\mathrm{d}^3r'\, \hat{\Psi}^\dagger(\mathbf{r})\hat{\Psi}^\dagger(\mathbf{r}')V_{int}(\mathbf{r}-\mathbf{r}')\hat{\Psi}(\mathbf{r}')\hat{\Psi}(\mathbf{r}) \quad . \end{aligned} \tag{3.15}$$

The bosonic field operator $\hat{\Psi}(\mathbf{r})$ annihilates a particle at position $\mathbf{r}$. The Hamiltonian Eq. (3.15) can be simplified by replacing V_{int} with an effective contact potential

[109, 112]. For s-wave collisions this is appropriate, since the details of the atomic interaction potential at short radii are not probed.

If interactions between particles are not too strong, which is usually the case for a dilute Bose-condensed gas, a mean field can be introduced. In the mean-field approach, the condensate contribution to the field operator is separated out. This was first suggested by Bogoliubov in 1947 [113]. The condensate part of the field operator is replaced by its expectation value $\psi(\mathbf{r},t) = \langle\hat{\Psi}(\mathbf{r},t)\rangle$. Note, that the condensate wavefunction $\psi(\mathbf{r},t)$ is normalized such that $\int \mathrm{d}^3r|\psi(\mathbf{r})|^2$ equals the number of particles in the BEC. Neglecting the non-condensed part of the bosonic field operator, one arrives at the Gross-Pitaevskii (GP) equation for the condensate wavefunction [9, 10, 114, 115]

$$\left(-\frac{\hbar^2\nabla^2}{2m} + V_{trap}(\mathbf{r}) + \frac{4\pi\hbar^2 a}{m}|\psi(\mathbf{r},t)|^2\right)\psi(\mathbf{r},t) \;=\; i\hbar\,\frac{d}{dt}\psi(\mathbf{r},t) \;\;. \tag{3.16}$$

This non-linear Schrödinger equation successfully describes a whole range of phenomena in dilute Bose-Einstein condensates, such as collective modes [116] or vortices [117].

The non-linear term proportional to the s-wave scattering length a and the atomic density $|\psi(\mathbf{r})|^2$ represents interactions on a mean-field level. For positive a, the interaction is effectively repulsive and the condensate is stable. However, for negative a the interaction is effectively attractive. In this case, the condensate can only be stable for a small number of atoms. Above a critical atom number, the condensate becomes unstable and collapses [118]. As the next section will show, Feshbach resonances are a means to change the scattering length and thereby access the different regimes of repulsion and attraction.

3.2 Feshbach resonances

By taking into account different internal states of the colliding atoms, the scattering problem becomes more complex. One consequence is the occurrence of Feshbach resonances. This section discusses the basic principles underlying Feshbach resonances and introduces the relevant interaction mechanisms. The reader interested in a detailed mathematical treatment of resonance scattering is referred to the literature [26, 106, 119–122].

3.2.1 Principle

In many scattering experiments, the particles have internal degrees of freedom, such as spin. Alkali atoms, for example, have a rich hyperfine structure. In a collision, each hyperfine state results in a different interaction potential. These potentials are referred to as scattering channels.

A Feshbach resonance occurs when two atoms undergoing a binary collision couple to a bound state of a different scattering channel. The situation is depicted in

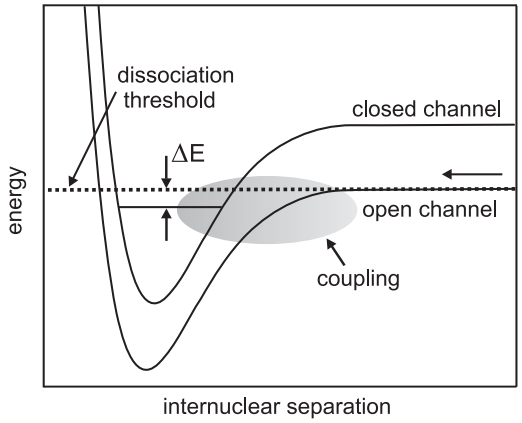

Figure 3.2: Principle of a Feshbach resonance. Due to the inter-channel coupling, atoms in the open channel can populate a bound state in the closed channel at small internuclear distances. When the energy difference between bound state and open-channel threshold, ΔE, goes to zero, the population in the bound state is resonantly enhanced. A Feshbach resonance occurs.

Fig. 3.2. The discussion is restricted to two channels with different threshold energies. Possible other channels corresponding to other atomic hyperfine states are not drawn. The atoms enter in the lower channel (open channel) with a kinetic energy very close to the dissociation threshold of that channel. The energy difference between the channels is much larger than the kinetic energy. Hence, the upper channel is energetically closed, i.e. atoms cannot leave the interaction region in the closed channel due to energy conservation.

If the energy of the atoms in the entrance channel is close to the energy of a bound state in the closed channel, the atoms can temporarily populate this bound state, provided the interaction Hamiltonian can flip spins, i.e. couple the two channels. If the two energies are degenerate, the population in the bound state is resonantly enhanced and a Feshbach resonance occurs.

3.2.2 Magnetically-induced Feshbach resonances

The open and closed channels involved in a Feshbach resonance typically have different spins, resulting in different magnetic moments of the two states. Hence, an external magnetic field induces a differential Zeeman shift between the two scattering potentials. This opens up the possibility to tune the system into resonance. The situation is sketched in Fig. 3.3(a). Shown are the energies of the open-channel dissociation threshold and of the closed-channel bound state as a function of magnetic field. The Feshbach resonance occurs at the magnetic field value B_{res} where the two states cross. In the vicinity of the resonance, the energy difference ΔE between the

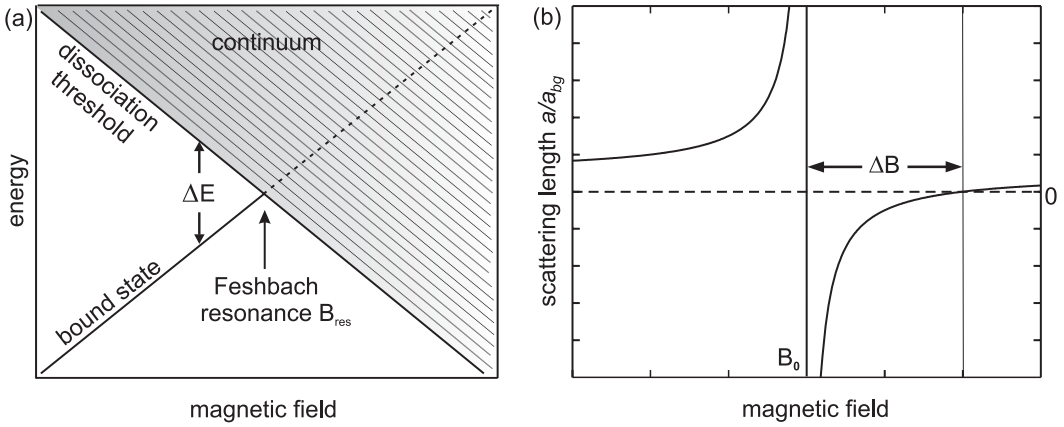

Figure 3.3: Magnetically tunable Feshbach resonance. (a) The energies of the open-channel threshold and the closed-channel bound state as a function of magnetic field. The Feshbach resonance occurs where the two levels cross. Above threshold, the bound state is only quasi-bound due to the coupling to the continuum. (b) At the Feshbach resonance, the s-wave scattering length a has a pole. The position of the pole B_0 is shifted with respect to the crossing of the uncoupled states at B_{res}. The width ΔB corresponds to the difference in magnetic field between the zero-crossing and the pole of a.

two states varies linearly with magnetic field

$$\Delta E \,=\, \Delta\mu\,(B - B_{res}) \;\; . \tag{3.17}$$

Here, $\Delta\mu$ denotes the difference in magnetic moments between the two states.

The coupling between the free atom-pair state and the molecular bound state modifies the scattering properties of the unbound atoms. The scattering length acquires a resonant contribution in the vicinity of the Feshbach resonance. Near resonance, the magnetic-field dependence of the scattering length is given by [120]

$$a = a_{bg}\left(1 - \frac{\Delta B}{B - B_0}\right) \;\; , \tag{3.18}$$

where a_{bg} is the background scattering length far away from the Feshbach resonance. ΔB is the magnetic-field width of the Feshbach resonance. Hence, due to the coupling to the closed-channel bound state the scattering length a has a pole at B_0, which is illustrated in Fig. 3.3(b). This is analogous to the situation described for the simple square-well potential in Sec. 3.1.3, where a bound state near threshold caused a pole in a. Note, that the pole position B_0 is different from the value of the magnetic field B_{res}, where the (uncoupled) molecular state crosses the dissociation threshold of the open channel. For the 1007-G resonance in ^{87}Rb discussed in Sec. 3.3, the resonance shift is $B_0 - B_{res} \approx -60$ mG [122].

3.2.3 Interaction Hamiltonian and selection rules

This section introduces the different interaction mechanisms for two ground-state alkali atoms. These interactions are able to flip spins and can therefore cause Feshbach resonances.

At large radius, the spins of two colliding ground-state alkali atoms are specified in terms of the hyperfine quantum numbers $|f_1, m_{f1}\rangle$ and $|f_2, m_{f2}\rangle$ of the two atoms. Together with l, m_l, E one obtains a complete set of quantum numbers. The atomic hyperfine spins can be added, yielding the total spin $\mathbf{F} = \mathbf{f_1} + \mathbf{f_2}$. The corresponding quantum numbers are F, m_F.

At shorter radius, the exchange interaction V_{ex} is the dominant term in the interaction Hamiltonian, so that the spins of the valence electrons are coupled to a total electronic spin $\mathbf{S}$. The corresponding singlet ($S = 0$) and triplet ($S = 1$) potentials differ drastically. Hence, the hyperfine quantum numbers f_1, m_{f1}, f_2, m_{f2} are not good quantum numbers at short radius. When writing V_{ex} as a matrix in the hyperfine basis, it therefore has large off-diagonal elements, which means that transitions between different hyperfine states are possible. V_{ex} is spherically symmetric and thus conserves l, m_l. For incoming s waves, V_{ex} can therefore cause Feshbach resonances only if the molecular state is an s-wave state. Since V_{ex} creates only forces internal to the system, the total angular momentum $\mathbf{l} + \mathbf{F}$ is conserved. Since m_l is conserved, m_F is conserved, too.

In addition, there are much weaker terms in the interaction Hamiltonian. The strongest of these terms is the spin-spin interaction V_{ss}, which is the sum of the magnetic dipole-dipole interaction of the valence electrons and the second-order spin-orbit interaction for the valence electrons. V_{ss} can change l, m_l because it is not invariant under spatial rotations. It causes transitions according to the selection rules $\Delta l = 0$ or ± 2 and $|\Delta m_l| \leq 2$. For incoming s waves, V_{ss} can therefore cause Feshbach resonances for d-wave molecular states. Since V_{ss} is much weaker than V_{ex}, the resulting inter-channel coupling is typically also much weaker. Hence, Feshbach resonances caused by V_{ss} are usually much narrower than those caused by V_{ex}. Since V_{ss} creates only internal forces, the total angular momentum $\mathbf{l}+\mathbf{F}$ is again conserved.

Even weaker terms in the Hamiltonian can cause other narrow Feshbach resonances, such as in ^{133}Cs near 20 Gauss, where an incoming s wave is coupled to a g-wave molecular state [123]. Δl is always even for the Feshbach resonances in atomic collisions, because the interaction Hamiltonian conserves parity. The only fundamental interaction that does not conserve parity is the weak interaction, but that is negligible here.

When an external magnetic field $\mathbf{B}$ is applied, the total angular momentum $\mathbf{l}+\mathbf{F}$ is no longer conserved, because the external field creates external forces. We consider only the case where $\mathbf{B}$ points along the z axis, so that rotational symmetry around the z axis implies the conservation of $m_l + m_F$. Note that if the magnetic field is strong, f_1, f_2 are no longer good quantum numbers at large radius.

3.2.4 Inelastic collisions

The increase in elastic collision rate near a Feshbach resonance is accompanied by a drastic enhancement of inelastic processes, which lead to atom loss and heating of the atom cloud. Two different inelastic processes are distinguished:

- **Inelastic two-body processes** will occur if the entrance channel in the collision is not the ground-state of the system. In this case, the atoms can undergo a transition to a lower-lying collision channel. The difference in internal energy between the two states is released as relative kinetic energy of the atom pair. Typically, this energy is enough for the atoms to leave the trap. However, since the Feshbach resonances used in our experiment involve the internal ground state of ^{87}Rb, two-body loss processes do not occur.

- In a **three-body recombination** event, three atoms collide, two of them form a weakly-bound molecule and the binding energy is released as relative kinetic energy of the collision partners which typically expels the molecule as well as the third atom from the trap. The third collision partner is needed for the formation of a molecule in order to conserve energy and momentum. The process is density dependent and can be expressed in terms of a rate equation for the atom loss as
$$\frac{dn(\mathbf{r})}{dt} = -K_3 n^3(\mathbf{r}) \,, \tag{3.19}$$
where K_3 is the three-body loss coefficient and $n(\mathbf{r})$ the atomic density. Near a Feshbach resonance three-body recombination is resonantly enhanced, leading to an increase of K_3 by several orders of magnitude [19, 21, 124].

3.3 The 1007-G Feshbach resonance

This section presents measurements on the variation of the scattering length near the broadest Feshbach resonance in ^{87}Rb. To this end, the mean-field driven expansion of a BEC is investigated as a function of magnetic field. Similar methods were used before by other groups for different alkali atoms [19, 21, 23, 125].

3.3.1 Expansion of a BEC near 1007 G

The basic idea behind our method for determining the scattering length is as follows: Let us consider a BEC trapped in an external potential. For typical atom numbers in the experiment, the kinetic-energy term in the Gross-Pitaevskii equation Eq. (3.16) can be neglected (Thomas-Fermi limit). Therefore, in equilibrium the non-linear interaction term $\propto a|\psi|^2$ balances the external trapping potential. But if the trap is switched off suddenly, the condensate expands driven by the non-linear interaction term. Thereby, a large positive scattering length results in a fast expansion. From the expansion dynamics of a condensate, information on the scattering length can

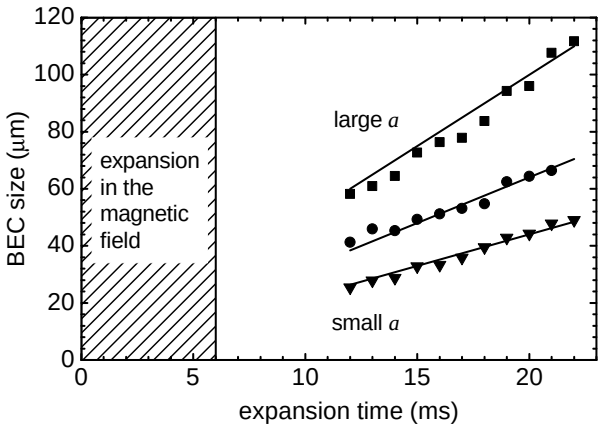

Figure 3.4: BEC expansion near the 1007-G Feshbach resonance. Shown is the half-width of a BEC as a function of expansion time for different values of the s-wave scattering length a. The expansion at different magnetic fields corresponding to different scattering lengths takes place within 6 ms after release from the dipole trap. The larger the scattering length, the faster the expansion and the larger the final size of the BEC. For expansion times longer than 10 ms, all the mean-field energy has been released and the width increases linearly with time.

therefore be extracted. Fig. 3.4 shows experimentally obtained expansion curves for different scattering lengths in the vicinity of the Feshbach resonance at 1007 G.

The experimental sequence for obtaining the data is as follows: A BEC is prepared in the crossed optical dipole trap as described in Chap. 2. For this particular measurement, the waists and powers of the dipole-trap beams are 33 μm and 38 mW for the horizontal beam, and 77 μm and 115 mW for the second beam. The horizontal beam creates an estimated trap depth in the horizontal plane of $\sim k_B \times 3$ μK. In the vertical direction, the trap barely supports the atoms against gravity with a trap depth of $\sim k_B \times 0.8$ μK. In a coordinate system, where the x axis is the symmetry axis of the magnetic trap and where gravity points along z, the trap frequencies are $(\omega_x, \omega_y, \omega_z) = 2\pi\times$ (50,170,120) Hz. The last two frequencies differ due to the gravitational sag. Typically, the atom numbers in the BEC and in the thermal fraction are 10^5 each. The peak density in the BEC is $\sim 2 \times 10^{14}$ cm^{-3}.

After loading of the dipole trap, the 1000-G field is switched on and held a few G above or below the Feshbach resonance for typically 500 ms. During this time, thermal drifts due to the ∼12 kW heat load dissipated in the magnetic-field coils have some time to settle. Next, the optical trap is switched off and simultaneously B is jumped to a value very close to or right at the Feshbach resonance. After holding B at its final value for 6 ms, B is switched off completely. The jump to the final field value actually takes $\sim$ 0.5 ms, the complete turn-off $\sim$ 1 ms. Note, that for this particular experiment, the small pair of coils for fast switching described in

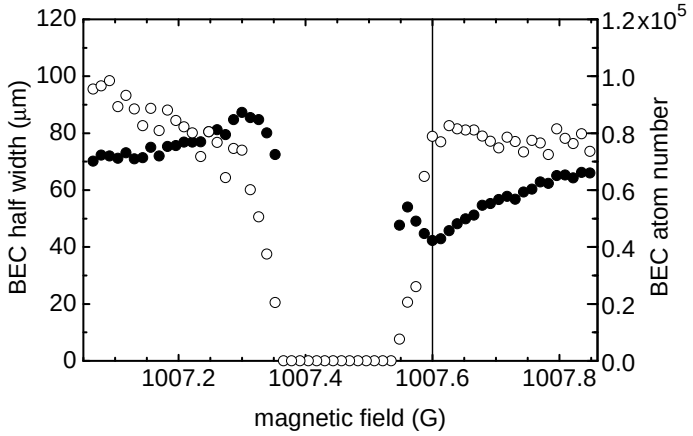

Figure 3.5: Vertical half width (•) and atom number (○) of the expanded BEC as a function of magnetic field B. Data points in the left (right) half of the figure were obtained by jumping towards the Feshbach resonance from smaller (larger) B, and for an expansion time of 18 ms (23 ms). B was jumped to its final value at the moment of release of the atoms from the trap. B was held there for 6 ms and then switched off. The vertical line at 1007.60 G indicates the onset of instability of the BEC due to negative values of a.

Chap. 2.3 was not yet available.

After a certain time-of-flight, an absorption image of the expanded cloud is taken. The atom number and size of the BEC and of the surrounding thermal cloud are determined from a two-dimensional fit. The magnetic field was calibrated using microwave spectroscopy in the vicinity of the Feshbach resonance with an accuracy of 0.03 G.

Figure 3.5 shows the size and atom number of the expanded BEC measured with the timing sequence described above. Instead of monitoring the complete expansion curve for each magnetic field value, it is sufficient to determine the final size and atom number after a time-of-flight of about 20 ms in order to extract a. As expected, the final condensate width increases (decreases) as the Feshbach resonance is approached from below (above). Additionally, the atom number is reduced as one approaches the resonance from either side due to an increase in inelastic processes. No BEC is left between 1007.37 G and 1007.53 G. The separation of adjacent data points in Fig. 3.5 is 13 mG, which is slightly larger than the estimated magnetic field resolution due to the measured current noise.

As one gets very close to the Feshbach resonance from either side, the upward (downward) trend in the width is reversed. On the low-field side of the resonance, this is a trivial consequence of the decrease in atom number, because a lower-density BEC releases less mean-field energy that drives the expansion. On the high-field side of the resonance, however, the effect is presumably related to the instability of the BEC in a regime of negative a discussed in Sec. 3.1.4.

3.3.2 Extracting the scattering length

In order to extract a from the measured size of the expanded BEC, the expansion process must be modeled. To this end, the model presented in Ref. [88] is extended to include a possible time dependence of a during the expansion. For the time being, the observed change in atom number is ignored. This effect will be incorporated in the analysis later on.

Initially, the BEC is confined in a harmonic potential with trap frequencies $(\omega_x, \omega_y, \omega_z)$. In the Thomas-Fermi approximation to the Gross-Pitaevskii equation Eq. (3.16), the initial density distribution $n(\mathbf{r})$ is an inverted parabola

$$n(\mathbf{r}) = n_0 \left[1 - \sum_{k=1}^{3} \left(\frac{r_k}{W_k} \right)^2 \right] \tag{3.20}$$

and $n(\mathbf{r}) = 0$ if the above expression is negative. Here, $n_0 = 15\,N/(8\pi\,W_x W_y W_z)$ is the peak density. The half widths along the coordinate axes r_k are

$$W_k(0) = \frac{1}{\omega_k} \left(15\,\frac{\hbar^2}{m^2}\,\omega_x\omega_y\omega_z\,a_i\,N \right)^{1/5} , \tag{3.21}$$

where m is the atomic mass, N the atom number in the BEC, and a_i the initial scattering length before release. At time $t = 0$, the trap is switched off, and a possible time dependence $a(t)$ may begin.

According to Ref. [88], the BEC profile stays a parabola during the expansion. Its widths are scaled by the parameters

$$\lambda_k(t) = \frac{W_k(t)}{W_k(0)} . \tag{3.22}$$

The evolution of the scaling parameters λ_k is described by the following set of coupled differential equations [88]

$$\ddot{\lambda}_k = \frac{1}{\lambda_x\lambda_y\lambda_z}\,\frac{\omega_k^2}{\lambda_k} . \tag{3.23}$$

The initial conditions are $\lambda_k(0) = 1$ and $\dot{\lambda}_k(0) = 0$. It is straightforward to show that a time-dependence of a modifies this equation to

$$\ddot{\lambda}_k = \frac{a(t)}{a_i}\,\frac{1}{\lambda_x\lambda_y\lambda_z}\,\frac{\omega_k^2}{\lambda_k} . \tag{3.24}$$

$a(t)$ appears in Eq. (3.24), because the expansion is driven by the mean-field energy which is proportional to $a(t)$. a_i appears in Eq. (3.24), because a_i determines the initial widths $W_k(0)$ with respect to which the λ_k are defined.

As mentioned earlier, jumping a from its initial to its final value a_f takes $\sim$ 0.5 ms. This delay is included in the model as follows

$$a(t) = \begin{cases} a_f & 0.5 \text{ ms} < t < 6 \text{ ms} \\ a_i = a_{\text{bg}} & \text{otherwise} . \end{cases} \tag{3.25}$$

Here, a_{bg} is the background value of the scattering length far away from the resonance and $t = 0$ is defined by the turn-off of the optical trap. The fact that a is switched back to a_{bg} at $t = 6$ ms has little effect, since for the parameters of the experiment almost all mean-field energy is released during the first 6 ms (except for very small values of a_f).

The atom loss shown in Fig. 3.5 must also be included in the model. For density-independent losses this is easy to do. In this case, the shape of the BEC remains parabolic during the expansion. With a time-dependent atom number $N(t)$, Eq. (3.24) is then modified to

$$\ddot{\lambda_k} = \frac{a(t)N(t)}{a_i N_i} \frac{1}{\lambda_x \lambda_y \lambda_z} \frac{\omega_k^2}{\lambda_k} . \tag{3.26}$$

Additionally, in Eq. (3.21), N is replaced by the initial value N_i. Since the dominant loss mechanism is actually likely to be density-dependent, this approximation will only be reasonable if a small fraction of the atoms is lost.

It is clear from Eq. (3.26) that the time dependence of the atom number is crucial. By varying the hold time at the final magnetic field from 1 to 6 ms, we experimentally checked for such a time dependence at $B = 1007.35$ G (last non-vanishing data point on the low-field side in Fig. 3.5), but found none: The final atom number was independent of the hold time over this range. It is hence obvious that the loss does not occur continuously during the total hold time. Instead, the loss occurs during the first 1 ms of hold time.

The origin of this loss is not totally clear. On the one hand, three-body recombination is drastically enhanced near resonance. In a later experiment, an increase in K_3 by four orders of magnitude near resonance was confirmed [126]. But, one expects three-body loss to be more or less a continuous process. A possible reason, why three-body losses would only be noticeable on time-scales shorter than 1 ms, could be a drastic decrease in density due to the fast losses and possibly also due to the fast expansion of the cloud. On the other hand, experiments by a group working with ^{85}Rb have revealed counterintuitive loss behavior near a Feshbach resonance which they attributed to the coherent formation of molecules [25, 127]. This mechanism could possibly also play a role in our experiment. However, a detailed understanding of all the loss mechanisms is difficult and not required for determining the scattering length a.

For further analysis, it is assumed that the atom loss occurs instantaneously at the same time as the change in a

$$N(t) = \begin{cases} N_f & 0.5 \text{ ms} < t \\ N_i & \text{otherwise} . \end{cases} \tag{3.27}$$

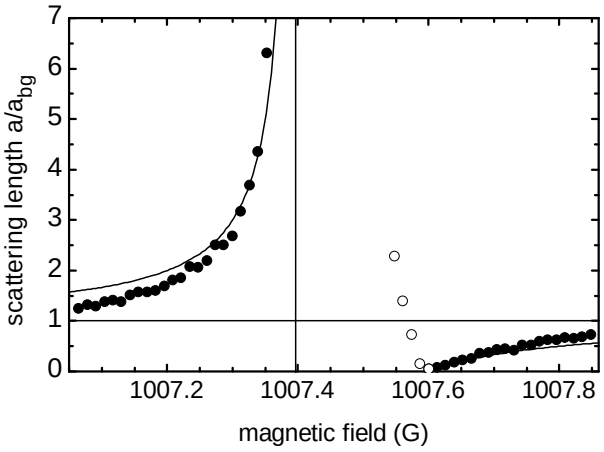

Figure 3.6: Scattering length as a function of magnetic field. The solid line is a fit to the experimental data (•). The best fit yields $\Delta B = 0.20$ G for the width and $B_{\rm res} = 1007.40$ G for the position of the resonance. Some experimental data points (∘) were not included in the fit, because they lie in the regime of negative a where the BEC is unstable.

For processing the data, the initial atom number N_i and the background value of the scattering length $a_{\rm bg}$ are needed. N_i was determined from the overall absorption in a measurement far away from the Feshbach resonance. In order to determine $a_{\rm bg}$, the size of an expanded BEC far away from the Feshbach resonance was measured. Using Eqs. (3.21)-(3.24) with $a(t) = a_i = a_{\rm bg}$, the background scattering length can be extracted, yielding $a_{\rm bg} = 108\, a_0$, where a_0 is the Bohr radius. Within the uncertainties in the calibration of the experiment, this is consistent with the theoretical value $a_{\rm bg} = 100.5\, a_0$ for the state $|1, +1\rangle$ [128]. For further data processing, the theoretical value was used.

Given N_i and $a_{\rm bg}$, $W_x(0)$ is calculated using Eq. (3.21), and thus the measured expanded widths $W_x(t)$ can be converted into $\lambda_x(t)$ according to Eq. (3.22). For every data point, the observed final atom number N_f in the BEC was then used to numerically solve the coupled differential equations (3.26) for the experimentally applied sequence Eqs. (3.25), (3.27). In the calculation, a_f was varied until the experimentally observed width was matched.

With this method, the data shown in Fig. 3.5 were processed to extract the scattering length. The resulting data are displayed in Fig. 3.6 together with a fit to the theoretical expectation Eq. (3.18). Some data points (∘ in Fig. 3.6) are not included in the fit for the following reason: Approaching the resonance from above in Fig. 3.5, one can see that the size of the expanded BEC decreases as expected, until at 1007.60 G (vertical line in Fig. 3.5) this trend is reversed. At the same field, significant atom loss abruptly sets in. We interpret this as the onset of instability of the BEC in a regime of negative scattering length [24, 118, 129–132]. This interpretation is further supported by the fact that the extracted value of a

shown in Fig. 3.6 reaches zero at this field. For the parameters of our experiment, the critical scattering length for instability [131, 133] is $a_{\rm crit} \approx -10^{-3}\, a_{\rm bg}$ which is very close to zero. Hence, we conclude that the zero crossing of a is located at $B_{\rm res} + \Delta B = 1007.60$ G and we use only one free parameter ΔB in our fit.

The fit in Fig. 3.6 agrees well with the experimental data. The best-fit value is $\Delta B = 0.20$ G, resulting in $B_{\rm res} = 1007.40$ G. These values are close to the theoretical predictions $\Delta B^{\rm theory} = 0.17$ G and $B_{\rm res}^{\rm theory} = 1008.5$ G [37]. $B_{\rm res}$ is also near the peak of the atom loss at 1007.34 G measured previously [37].

The method to determine a as described here differs slightly from the methods previously used in other experiments [19, 23, 124]. There, the final magnetic field was applied while the BEC was still in the trap and the system had time to equilibrate before the BEC was released from the trap. No matter if the expansion time is almost zero [23] or long [19, 124] (in which case B was still on during the initial expansion), the observed BEC size W yields $a \propto W^5$. With the method used here $a \propto W^2$. This is due to the fact that the initial BEC peak density n_i is independent of B. Hence, the mean-field energy ($\propto n_i a$) is converted into kinetic energy, so that the final velocity (and thus W) is proportional to $a^{1/2}$. Therefore, noise in the determination of W is not amplified as much when extracting a.

Although the variation of the s-wave scattering length was demonstrated over quite a large range - an increase by a factor of ~ 7 and a decrease by about a factor of ~ 20 compared to a_{bg} - the drastically enhanced inelastic losses near resonance pose a severe problem for future experiments relying on the tuning of the scattering length. This is at least true for the low-field side of the resonance. On the high-field side, the loss only sets in around the zero-crossing of the scattering length. Hence, for experiments relying on minimizing elastic interactions, the Feshbach resonance at 1007.4 G might be suitable.

Chapter 4

Feshbach molecules

The coupling to the molecular bound state near a Feshbach resonance leads to a pole in the s-wave scattering length. This was demonstrated in the previous chapter. The present chapter deals with another consequence of the inter-channel coupling: An adiabatic magnetic-field ramp across a Feshbach resonance can transfer population from the free atomic pair state into the molecular bound state. This corresponds to a controlled chemical reaction with no latent heat released. In principle, an atomic BEC could be converted into a molecular BEC using this technique.

The chapter starts with a brief introduction into the theoretical concepts underlying molecule association by Feshbach resonances. Next, experimental results on molecule creation from a BEC by a magnetic-field ramp across the 1007-G Feshbach resonance in ^{87}Rb are presented [53]. The rest of the chapter is devoted to the dissociation of Feshbach molecules by reversing the magnetic-field ramp. From the energy released in the dissociation process, the width of the corresponding Feshbach resonance can be inferred. The technique is surprisingly insensitive to magnetic-field noise. This allowed us to measure the widths of several very narrow Feshbach resonances in ^{87}Rb [71].

4.1 Molecule Association

Molecule association is easiest to understand for two trapped atoms. Section 4.1.1 deals with this situation. Next, we turn our attention to molecule association in a BEC. A simple mean-field model is introduced in Sec. 4.1.2. In Secs. 4.1.3 - 4.1.5 experimental results on molecule creation in a BEC are presented.

4.1.1 Two atoms in a trap

In a confining trap, the continuum of atom-pair states $|\psi_{\mathbf{k}}^{(+)}\rangle$ above threshold in the open channel is replaced by a ladder of discrete energy levels, as illustrated in Fig. 4.1. Solid (dashed) lines represent energy eigenstates in the presence (absence) of coupling. Note, that the zero of energy is chosen to coincide with the energy of

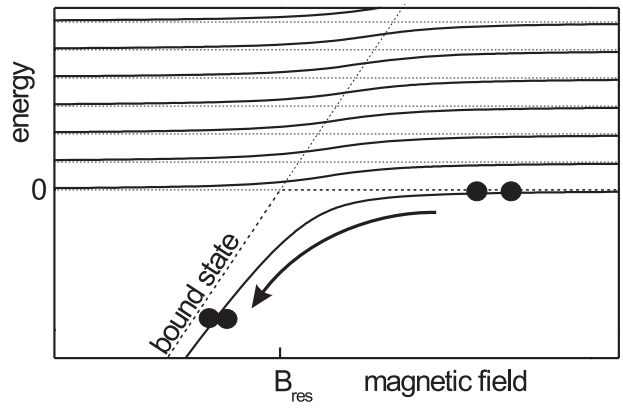

Figure 4.1: Association of a molecule in a trap. The solid lines represent the energy levels of two trapped atoms which couple to a molecular bound state near a Feshbach resonance. The dashed lines are the energies in the absence of inter-channel coupling. B_{res} denotes the crossing of the lowest (uncoupled) atom-pair state with the (uncoupled) molecular state. The lowest atom-pair state is adiabatically connected to the molecular bound state. Hence, an adiabatic magnetic-field ramp with $dB/dt < 0$ (represented by the arrow) transfers an atom pair into a bound molecule. The reverse ramp dissociates the molecule back into the atom pair.

the open-channel dissociation threshold. Hence, the two-atom states are flat in this graph, while the molecular state has a positive slope ($\Delta\mu > 0$).

In order to create molecules, an atom pair is initially prepared in the lowest trap state at magnetic fields well above resonance $B > B_{res}$. The lowest trap state is adiabatically connected to the molecular bound state on the low-field side of the Feshbach resonance. Hence, an adiabatic ramp across resonance to $B < B_{res}$ transfers the unbound atom pair into a bound molecule which is indicated by the arrow in Fig. 4.1. The adiabatic ramp can be reversed, which dissociates the molecule back into an open-channel atom pair. The situation is different if an atom pair is initially prepared in the lowest trap state at magnetic fields $B < B_{res}$. Here, an adiabatic upward ramp takes the atom pair into a higher-lying trap state. This adds energy to the system. Note that the ramping scheme for associating and dissociating molecules is also applicable in free space.

In general, the calculation of the energy eigenvalues is nontrivial. The situation simplifies considerably, if the splitting between the trap levels is large compared to the atom-molecule coupling. In this case, only the lowest (uncoupled) atom-pair state, denoted by $|\phi_a\rangle$, and the (uncoupled) molecular state $|\phi_m\rangle$ have to be taken into account. In a matrix representation with respect to the basis $\{|\phi_a\rangle, |\phi_m\rangle\}$, the

corresponding Hamiltonian is given by

$$H = \begin{pmatrix} 0 & \frac{\hbar}{2}\Omega_0 \\ \frac{\hbar}{2}\Omega_0^* & E_m(t) \end{pmatrix} \quad . \tag{4.1}$$

The energy of the atom-pair state was set to zero, while the time-dependent energy of the molecular state is given by $E_m(t) = \Delta\mu(B(t) - B_{res})$. The coupling matrix element is written in terms of an angular frequency as

$$\frac{\hbar\Omega_0}{2} = \langle\phi_a|H|\phi_m\rangle \quad . \tag{4.2}$$

We will now show that Ω_0 can be related to parameters of the scattering problem with an incoming plane wave. To this end, we consider an interatomic potential with a finite range R and investigate the low-energy limit $\mathbf{k} \to 0$ of the scattering problem. Here, $f \to -a_{bg}$ with a_{bg} from Eq. (3.10). Hence, Eq. (3.2) becomes

$$\psi_0^{(+)}(r) = C\left(-\frac{a_{bg}}{r} + 1 + O(kr)\right) \quad \text{for } R < r \quad . \tag{4.3}$$

Here, C is a constant that is determined by normalization of the wavefunction. If the quantization volume V fulfills $V \gg R^3$, then the contribution of the region $r < R$ to the value of C becomes negligible. Hence, C might depend on a_{bg} but is independent of all other properties of the interatomic potential. Obviously, $\psi_0^{(+)}$ is proportional to C, so that

$$\langle\phi_m|H|\psi_0^{(+)}\rangle = C\frac{g}{\sqrt{2}} \quad . \tag{4.4}$$

For low enough energy, g is independent of $\mathbf{k}$. For the scattering state with an incoming plane wave, $|C|^2 = 1/V$ and we recover Eq. (23) from Ref. [27] with $|\alpha| = |g|/\sqrt{2}$. Combining Eqs. (25) and (42) of that reference, we obtain

$$\Delta B = \frac{|g|^2}{2\Delta\mu U_{bg}} \quad , \tag{4.5}$$

where

$$U_{bg} = \frac{4\pi\hbar^2 a_{bg}}{m} \quad . \tag{4.6}$$

This relates g to parameters of the Feshbach resonance that are already known.

We now discuss the special case of two atoms in a harmonic trap. Experimentally, such a situation can for example be realized with atoms in an optical lattice as will be described in Chap. 6. In the case of a harmonic trap, Eqs. (4.3) and (4.4) are also applicable with $|\phi_a\rangle$ corresponding to $|\psi_0^{(+)}\rangle$. The condition Eq. (4.3) is only useful if the significant values of k fulfill $kR \ll 1$, otherwise the term $O(kr)$ would not be negligible. With $k \sim 1/a_{ho}$, where $a_{ho} = \sqrt{\hbar/m\omega}$ is the harmonic oscillator length, this implies a clear separation of length scales in the problem: $R \ll a_{ho}$.

The problem of two atoms in a harmonic trap fulfilling the condition Eq. (4.3) was solved in Ref. [112]. The result for the ground state is

$$|C|^2 = \left(\frac{1}{\sqrt{2\pi}a_{ho}}\right)^3 \left[1 + 0.490\frac{a_{bg}}{a_{ho}} + O\left(\frac{a_{bg}}{a_{ho}}\right)^2\right] \quad . \tag{4.7}$$

We neglect the terms of order $O(a_{bg}/a_{ho})$ and use Eq. (4.4). Hence,

$$\left|\frac{\hbar\Omega_0}{2}\right|^2 = \left(\frac{1}{\sqrt{2\pi}a_{ho}}\right)^3 \Delta B \Delta\mu U_{bg} \quad . \tag{4.8}$$

The energy levels of Eq. (4.1) form an avoided crossing as a function of magnetic field. It is therefore possible to adiabatically transfer an atom pair to the molecular state by ramping the magnetic field slowly from above to below resonance. For a linear ramp with constant ramp speed, the transition probability to the molecular state in such a two-level system is described analytically by the Landau-Zener formula [134]

$$P_{LZ} = 1 - e^{-2\pi\Gamma_{LZ}} \quad \text{with} \quad \Gamma_{LZ} = \left|\frac{\Omega_{Rabi}^2}{4\frac{d}{dt}\Delta}\right| \quad , \tag{4.9}$$

where $\hbar\Delta$ is the energy difference between the uncoupled states and Ω_{Rabi} the angular Rabi frequency. Hence with $\Delta = E_m/\hbar$ and $\Omega_{Rabi} = \Omega_0$ from Eq. (4.8), we obtain

$$\Gamma_{LZ} = \sqrt{\frac{2}{\pi}}\frac{\hbar}{ma_{ho}^3}\left|\frac{a_{bg}\Delta B}{\frac{dB}{dt}}\right| \quad . \tag{4.10}$$

This is almost identical to the result of Ref. [135] where a different approximation was used. For small ramp speeds, Eqs. (4.9) and (4.10) predict a transition probability close to 1. The validity of the Landau-Zener model was verified in recent experiments on molecule creation in an optical lattice [74, 136].

4.1.2 Molecule association in a BEC

We now turn our attention to molecule association in a Bose-Einstein condensate. Due to the complex many-body nature of the system, a detailed theoretical description is difficult [122, 137–139]. Here, we focus on a simple mean-field model [26, 27, 50, 140].

The model is based on a Hamiltonian in second quantization describing the atom-molecule coupling near a Feshbach resonance (see e.g. Eq. (1) in Ref. [138]). Neglecting correlations between particles and assuming that the molecules form a BEC, a set of coupled Gross-Pitaevskii equations can be derived [27]

$$i\hbar\frac{d}{dt}\psi_a = H_a\psi_a + U_{bg}\psi_a^*\psi_a\psi_a + g^*\psi_a^*\psi_m \tag{4.11}$$

$$i\hbar\frac{d}{dt}\psi_m = H_m\psi_m + \frac{g}{2}\psi_a\psi_a \quad . \tag{4.12}$$

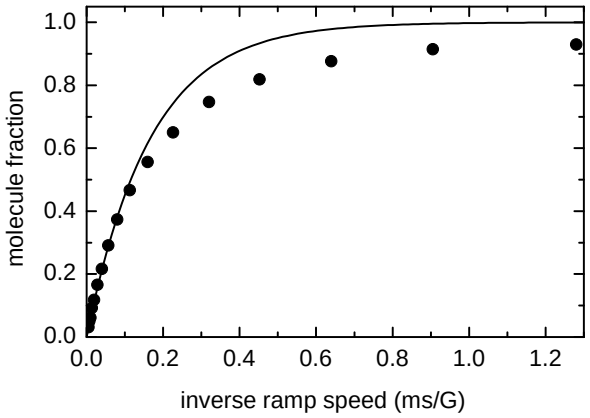

Figure 4.2: Molecule conversion efficiency as a function of inverse ramp speed. The numerical solution (•) of Eqs. (4.11) and (4.12) was determined for a linear ramp across the Feshbach resonance at 1007.4 G and a homogeneous atomic density of $n_a = 10^{14}$ cm^{-3}. U_{bg} is neglected in the calculation. The solid line is the corresponding prediction from the Landau-Zener model Eq. (4.9).

Here, ψ_a and ψ_m denote the atomic and molecular condensate wavefunction, respectively. H_a and H_m are the single-particle Hamiltonians for an atom and a molecule, respectively. We consider a homogeneous system, where they reduce to $H_a = 0$ and $H_m = E_m$. Finally, g and U_{bg} are given by Eqs. (4.5) and (4.6).

For a homogeneous system, ψ_a and ψ_m do not depend on position and the total density

$$n = |\psi_a(t)|^2 + 2|\psi_m(t)|^2 \tag{4.13}$$

is a constant of motion. For the following discussion we assume that the system is initially prepared as a pure atomic BEC and we neglect U_{bg}. The scaling $\tilde{\psi}_m = \psi_m\sqrt{2}$ makes it obvious that the coupled equations (4.11) and (4.12) resemble those of a standard two-level system with a detuning $\Delta = E_m/\hbar$ and a time-dependent Rabi frequency

$$\Omega_{Rabi}(t) = \sqrt{2}g\psi_a(t)/\hbar \ . \tag{4.14}$$

As before, we are interested in linear magnetic-field ramps across the Feshbach resonance. For slow ramps, the mean-field model predicts the formation of a large molecular BEC, as illustrated in Fig. 4.2. For comparison, the solid line shows the prediction from the Landau-Zener model Eq. (4.9) assuming a time-independent Rabi frequency $\Omega_{Rabi} = \frac{g}{\hbar}\sqrt{2n_a}$, where n_a is the initial atomic density. For small molecule fractions, the Landau-Zener model agrees well with the mean-field prediction. This is plausible, since the Landau-Zener model is based on a constant Rabi frequency, corresponding to a small depletion of the atomic condensate.

A more sophisticated model developed by the Köhler group [122] takes a variety of additional effects into account, such as pair correlations, the mean-field energy

in the atomic BEC, a harmonic trap, excitation of collective modes during the magnetic-field ramp in the atomic and the molecular BEC, etc. The only processes not incorporated in the model are inelastic collisions. For the Feshbach resonance at 1007.4 G in ^{87}Rb and realistic experimental parameters, the model predicts a molecule-conversion efficiency near 80% for ramp speeds slower than 1 G/ms. For linear magnetic-field ramps, the predictions of this model are fairly similar to the predictions of the simple mean-field model.

4.1.3 Observation of molecules

We performed an experiment on molecule association in a BEC using a linear magnetic-field ramp across the 1007-G Feshbach resonance in ^{87}Rb. The experiment starts with a BEC of ^{87}Rb atoms prepared in the crossed dipole trap (see Chap. 2). As before, the BEC and the thermal cloud typically contain 10^5 atoms each, leading to a peak density of 2×10^{14} cm^{-3} at trap frequencies of $2\pi \times (50, 170, 120)$ Hz. The atoms populate the spin state $|f, m_f\rangle = |1, +1\rangle$, in which the Feshbach resonance at 1007.4 G occurs. Next, a homogeneous magnetic field of $\sim$ 1008 G is applied. During the turn-on of this field, the system crosses the Feshbach resonance at such a large ramp speed ($\sim$ 40 G/ms) that the resonance has little effect on the atoms.

Next, the dipole trap is switched off and the rest of the experimental sequence takes place with the particles in free flight. This reduces inelastic loss processes as will be explained in more detail in Sec. 4.1.4. The magnetic field is now ramped slowly at typically 1 G/ms from above to below the Feshbach resonance in order to create molecules. Subsequently, the field is held at a certain value B_{hold} for 3 ms. During this time, a magnetic-field gradient of 23 G/cm is applied. This Stern-Gerlach field accelerates atoms and molecules differently because of their different magnetic moments. Hence, atomic and molecular cloud separate in space. Then, the gradient field is turned off, and the magnetic field is ramped back slowly to $\sim$ 1008 G (also typically at 1 G/ms). This dissociates molecules back into free atoms. Next, the magnetic field is turned off completely, again crossing the resonance so rapidly that this has little effect. The atoms fly freely for another 3 ms allowing the two clouds to separate even further. Finally, an absorption image is taken with laser light that is near-resonant with an atomic transition. Atoms that were converted into molecules but never converted back into free atoms are not seen by the detection laser.

Experimental results for $B_{hold} = 1005.2$ G are shown in Fig. 4.3, where two clearly separated atom clouds are visible. With the Stern-Gerlach field applied, the magnetic field decreases from left to right in this figure. Therefore, the cloud on the left/right in Fig. 4.3 must have been in a high/low-field seeking state during application of the Stern-Gerlach field. Hence, the right cloud shows atoms that were converted into low-field seeking molecules during the first crossing of the Feshbach resonance and converted back when ramping back. The left cloud, however, consisted of high-field seeking atoms throughout the whole experiment. The spatial

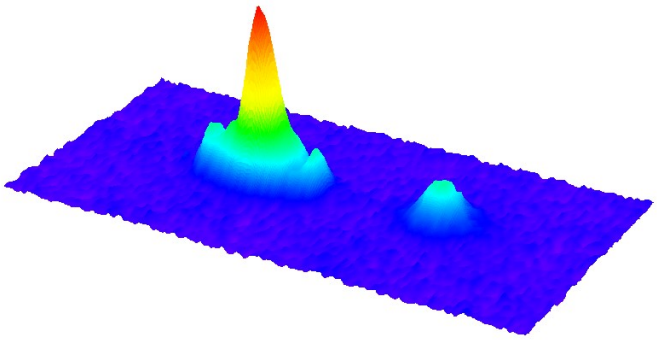

Figure 4.3: Stern-Gerlach detection of molecules. The cloud on the right consists of atoms that were temporarily converted into molecules. The molecules were separated from the non-converted atoms (left cloud) by a Stern-Gerlach field. For imaging, the molecules were dissociated back into free atoms.

separation of the clouds unambiguously shows that molecules are created, without the need to directly image the molecules.

4.1.4 Molecule-creation efficiency

It is obvious from Fig. 4.3 that the molecule-creation efficiency in the experiment is low. In addition, a large fraction of the initial atom number is missing after the association and dissociation. This missing fraction is probably due to inelastic atom-molecule and molecule-molecule collisions. Since Feshbach molecules are in a highly-excited internal ro-vibrational state, they can decay to lower-lying vibrational levels during a collision with an atom or another molecule. The difference in binding energy is released as kinetic energy in the relative motion of the molecule and its collision partner. This energy is typically much larger than the trap depth so that both particles involved in the collision are lost from the trap.

In a measurement with slightly different dipole-trap parameters (see Sec. 4.2.2), we checked for a dependence of the creation efficiency on ramp speed. Results of this measurement are presented in Fig. 4.4. The plot shows the number of atoms converted into molecules and subsequently detected by the Stern-Gerlach technique ($\circ$). We also determined the number of atoms in the remnant BEC (after association and dissociation) and subtracted it from the number of atoms in the initial BEC (before association). This difference ($\bullet$) is also plotted in Fig. 4.4. Note, that the density in the thermal cloud is so low, in particular after expansion, that only very few molecules are associated from the thermal cloud. Hence, the number of atoms in the thermal cloud is hardly affected by the association ramp. With decreasing speed of the molecule-creation ramp, the number of molecules first increases as expected, and then saturates for slow ramps with inverse ramp speeds above ~ 0.5 G/ms. For

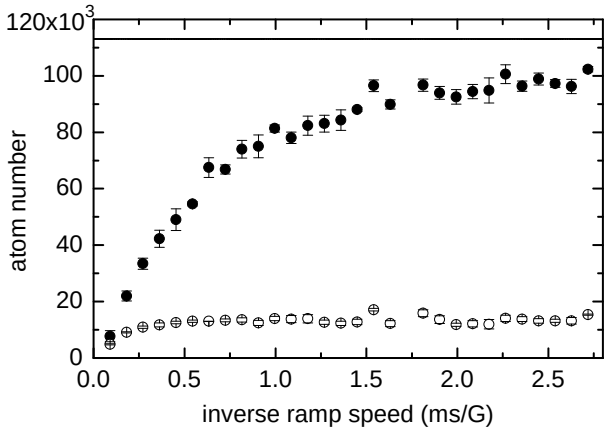

Figure 4.4: Atom numbers as a function of inverse speed of the association ramp. The number of atoms that were temporarily converted into molecules and detected after Stern-Gerlach separation (○) depends hardly on ramp speed. In contrast, the difference (●) between the atom numbers in the initial BEC and the remnant BEC resembles the prediction in Fig. 4.2. The difference between the two data sets shows the large fraction of missing atoms for slow ramps. The solid line indicates the initial atom number.

slow ramps, there is a large fraction of missing atoms.

The inelastic collision rates that cause the large missing fraction are density dependent. If a given molecule creation efficiency is desired, high densities allow for fast association, so that there is only little time during which loss can occur. However, at high density the loss rates are fast. Hence, it is not obvious whether the observed number of molecules will be optimized for small or large density. The experiment shows that if the conversion to molecules is performed just before the release from the trap, the observed number of molecules is reduced by a factor of ~ 2. This might be an indication that the inelastic collision rates dominate for the high densities in the trap. In the experiment, the cloud is therefore allowed to expand after turning off the dipole trap. After an expansion time of typically 1 to 7 ms, the molecules are associated. This expansion is estimated to reduce the atomic density by a factor between 2 and 90 as compared to the in-trap situation. However, a strong dependence of the observed molecule number on density was not found in this regime.

Inelastic atom-molecule and molecule-molecule collisions are characterized by rate coefficients K_{am} and K_{mm}, respectively. Typically, for molecules made from bosonic atoms K_{am} and K_{mm} are on the order of 10^{-10} cm^{3}s^{-1} [59–61]. K_{am} and K_{mm} can be incorporated into the mean-field model Eqs. (4.11) and (4.12). This approach was followed in Ref. [27, 141, 142]. In addition, the mean-field driven expansion of the BEC can be included in numerical simulations [141].

Analytic solutions to this general model are not known. In order to simplify the

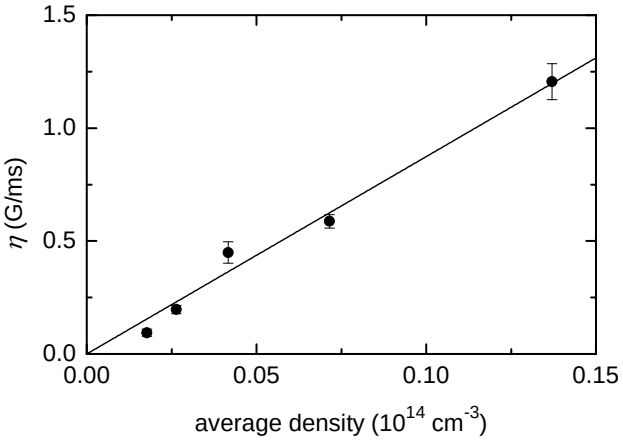

Figure 4.5: Parameter η from Eq. (4.17) as a function of average BEC density. The solid line is a linear fit to the experimental data (•). The slope of the fit agrees reasonably well with the prediction from Eqs. (4.14) and (4.16).

discussion, we now focus on the limit of fast ramps, where analytic expressions can be obtained as explained in the following. For fast ramps, only few molecules are created so that the loss is dominated by K_{am}, which we assume to be independent of magnetic field. In addition, the atomic density n_a hardly varies with time, resulting in a time-independent loss-rate coefficient for molecules $\Gamma = K_{am} n_a$. Furthermore, we assume that the ramp is so fast that the loss during the relevant creation processes is negligible. The relevant creation processes occur for $|\Delta| < |\Omega_{Rabi}|$, so that the ramp speed must meet the condition $|\frac{d}{dt}\Delta| \gg \Gamma|\Omega_{Rabi}|$. In this regime, the evolution of the molecular density can be approximated by a quasi-instantaneous creation at $t = 0$, followed by an exponential decay

$$\frac{2n_m(t)}{n_a^{init}} = \frac{\pi}{2} \left| \frac{\Omega_{Rabi}^2}{\frac{d}{dt}\Delta} \right| e^{-\Gamma t} \qquad \text{for } t > 0 \,. \tag{4.15}$$

Here, we made use of the fact that the atom number hardly changes with time, so that Ω_{Rabi} becomes time-independent, and the Landau-Zener formula can be used. In addition, we expanded the exponential in the Landau-Zener formula for fast ramps. Finally, n_a^{init} is the initial atomic density.

The corresponding evolution of the atomic density results from the following consideration: During the quasi-instantaneous association, the total density is conserved, so that $n_a(0) + 2n_m(0) = n_a^{init}$. The following decay removes one atom along with each molecule, so that $\frac{d}{dt} n_a = \frac{d}{dt} n_m$. Hence,

$$1 - \frac{n_a(t)}{n_a^{init}} = \frac{\pi}{4} \left| \frac{\Omega_{Rabi}^2}{\frac{d}{dt}\Delta} \right| \left(3 - e^{-\Gamma t}\right) \qquad \text{for } t > 0 \,. \tag{4.16}$$

In the experiment, the Stern-Gerlach method separates the atomic and molecular clouds. The typical duration of the separation process is ~ 1 ms. After the separation, the decay caused by K_{am} comes to an end. Eqs. (4.15) and (4.16) illustrate that a long time t between molecule creation and the end of the Stern-Gerlach separation can reduce the molecule number drastically, whereas $1 - \frac{n_a(t)}{n_a^{init}}$ is fairly robust and changes by a factor of no more than 3/2.

We experimentally studied the dependence of the conversion efficiency on ramp speed and on initial atomic density. In order to vary the ramp speed, we scanned the duration of the magnetic field ramp, leaving the initial and final magnetic-field values constant. Varying the ramp speed therefore also varies the time span between creation and Stern-Gerlach separation. A quantitative understanding of n_m as a function of ramp speed is difficult because of the losses. An analysis of $1 - \frac{n_a(t)}{n_a^{init}}$, however, is much easier due to its relative robustness against loss. Equation (4.16) predicts that this quantity depends linearly on inverse ramp speed. We confirmed this experimentally (see e.g. Fig. 4.4) and define a pre-factor η by

$$1 - \frac{n_a(t)}{n_a^{init}} = \eta \left(\frac{dB}{dt} \right)^{-1} . \tag{4.17}$$

Measured values of η are shown in Fig. 4.5. The atomic density was varied by scanning the expansion time between release from the trap and the time, where the association ramp crosses the pole of the Feshbach resonance. Since the system is inhomogeneous, we plot η as a function of the average density $\langle n_a \rangle = (1/N) \int n_a^2(\mathbf{r}) d^3r$, where N is the total atom number before association and we assume that the BEC has the shape of a Thomas-Fermi parabola. Based on the observation that the missing fraction of atoms is large, we assume $\Gamma t \gg 1$ for the analysis. Equations (4.14) and (4.16) predict that η depends linearly on atomic density. The line in Fig. 4.5 shows a linear fit to the data. The slope of the fit agrees with the expectation within 10% which is surprising given the simplicity of the model and the uncertainty in atom-number calibration.

Note that in principle the dissociation ramp could add energy to the remnant BEC and thus heat atoms out of the remnant BEC, as discussed in Refs. [50, 124, 140]. The data shown in Fig. 4.5 were taken with sufficient time of flight between association and dissociation so that the density during dissociation is low enough that this heating is negligible.

While the above discussion shows that the decrease in atom number for fast ramps can be modeled fairly easily, the molecule creation efficiency depends more strongly on the loss processes and a quantitative model is beyond the scope of this thesis. Experimentally we find a maximum creation efficiency of $\sim 10\%$. To this end, the final magnetic field of the molecule creation ramp must be optimized. The best end point of the ramp turns out to be close to the pole of the Feshbach resonance, as expected for fast losses. A similar idea was used to optimize the molecule number in Ref. [123].

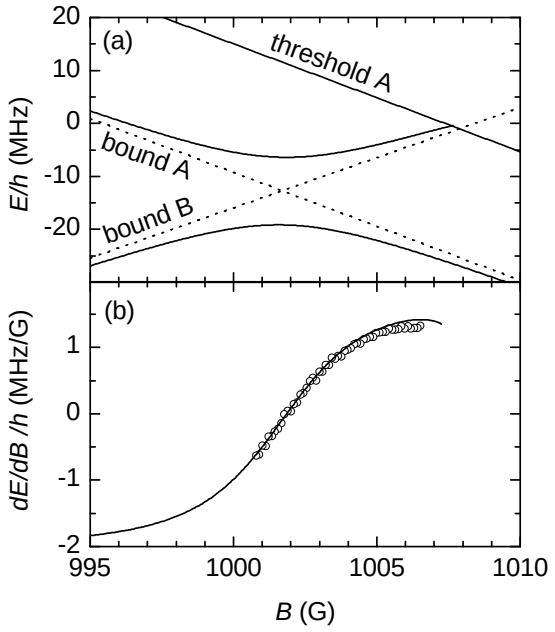

Figure 4.6: Molecular magnetic moment. (a) Energy as a function of magnetic field. The binding energy of the highest-lying bound state in the open-channel (A) with respect to the dissociation threshold is $h \times 24$ MHz, independent of magnetic field. The energy of the bound state supported by the closed-channel (B) crosses both these lines. The bound state in channel A is crossed at 1001.7 G, leading to an avoided crossing with a splitting of $h \times 13$ MHz. The dissociation threshold A is crossed around 1007 G causing the Feshbach resonance. (b) Derivative dE/dB of the upper branch of the avoided crossing. Experimental data for the molecules ($\circ$) are compared with the prediction from theory (solid line) that contains no free fit parameters.

4.1.5 Magnetic moment and 1D trapping

While the molecule-conversion efficiency is rather low in the experiment, the absolute number of molecules is large enough to perform further experiments and thereby investigate the properties of the Feshbach molecules. This section discusses such an experiment.

From the displacement of the clouds induced by the Stern-Gerlach field the magnetic moment of the particles can be extracted. The displacement is proportional to the force $\mathbf{F} = -(dE/dB)\nabla|\mathbf{B}|$ exerted by the Stern-Gerlach field. Here, E is the energy of the atomic and molecular state, respectively. dE/dB is related to the magnetic moment μ of the particles. For the atoms, the extracted experimental value of dE/dB is independent of B_{hold} and agrees well with the expectation from the Breit-Rabi formula [95].

For the molecules, however, Fig. 4.6(b) displays a pronounced dependence of dE/dB on B_{hold}. This magnetic-field dependence is due to the presence of the

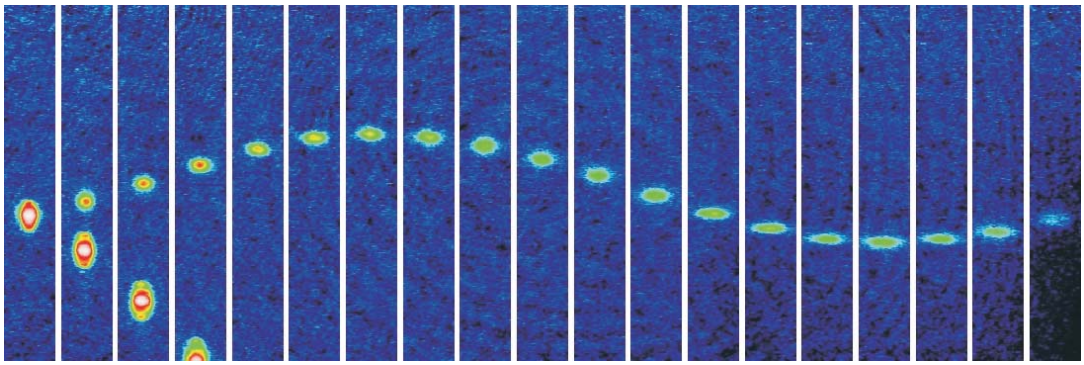

Figure 4.7: Molecule oscillation. According to Fig. 4.6, the molecules are 1001.7-G seekers. With a magnetic field gradient applied in the vertical direction, the molecules oscillate around a point in space where the magnetic field equals 1001.7 G. Note that gravity points to the right in the above pictures. The images were recorded for a series of different durations of the Stern-Gerlach field, ranging from 0 to 18 ms (left to right). The observed oscillation frequency of 56 Hz agrees well with the theoretical expectation. The anisotropic expansion of the molecular cloud is due to the fact that the one-dimensional trapping potential prevents the cloud from expanding in the horizontal direction. The atomic cloud is simply accelerated on a parabola. The size of each image is 1.7×0.24 mm.

highest-lying bound state in the open channel. Theoretical results for the energy of this state are shown in Fig. 4.6(a) [143]. At a field value of 1001.7 G, this bound state (A) crosses the bound state in the closed channel (B) that is populated when ramping across the Feshbach resonance. Due to the exchange interaction, this is an avoided crossing, in which the molecules adiabatically follow the upper branch. The experimentally observed values of dE/dB agree well with the theoretical expectation. Both are shown in Fig. 4.6(b).

When a molecule passes through the upper branch of the avoided crossing, its vibrational quantum number changes from -5 to -1 (counting from threshold). Correspondingly, the size of the molecule, i.e. the outer turning point of the vibrational state of the nuclei, changes by a factor of ~ 3.

The reversal of the sign of dE/dB visible in Fig. 4.6(b) makes the molecules 1001.7-G seekers, instead of the usual high- or low-field seekers. As a consequence, the molecules can be trapped by applying an inhomogeneous magnetic field. In the presence of a magnetic-field gradient, the quadratic dependence of $E(B)$ in Fig. 4.6(a) creates a harmonic confinement for the molecules. The resulting harmonic oscillation is shown in Fig. 4.7 for a magnetic-field gradient of 100 G/cm with the molecules initially prepared at 1003.2 G. This corresponds to a one-dimensional trap for molecules. In principle, such a trap could work in three dimensions.

Note that the trap here is very different from a standard magnetic trap, where usually low-field seeking particles are trapped at a minimum of $|\mathbf{B}|$ (see Sec. 2.1.2).

Here, the molecules are trapped at a specific value of $|\mathbf{B}|$, which is not a minimum of the field configuration.

4.2 Molecule Dissociation

Up to now, molecule dissociation merely served as a tool for molecule detection. Slow dissociation ramps transfer the population back into unbound atom-pair states. Ideally, this does not add energy to the system. But what happens if the dissociation ramp is fast? This section gives an answer to this question and introduces an experiment in which non-adiabatic dissociation ramps are used to determine the width of four Feshbach resonances in ^{87}Rb.

4.2.1 Dissociation by fast ramps

The case of two atoms in a trap (Fig. 4.1) gives us a good idea about the effect of fast ramps: a fast ramp takes part of the population in the molecular bound state diabatically across resonance. At each avoided crossing with a trap state, part of the population ends up in that unbound atom-pair state. The faster the ramp, the more population is dragged to higher trap states. Hence, a faster ramp adds more energy to the system.

In free space, the situation is similar. Here, the molecular state couples to a continuum of states above the open-channel dissociation threshold. At fixed magnetic field, this leads to an exponential decay of the molecular state into unbound atom pairs. The difference in energy between the molecular state and the open-channel threshold, $E = \Delta\mu(B - B_{res})$, is released as kinetic energy in the relative motion of the atom pair. Since total momentum is conserved during dissociation, each atom carries away a kinetic energy of $E_{kin} = E/2$, and the atoms have precisely opposite momentum vectors. The rate $\Gamma_m(E)$, at which a molecule decays into an atom pair, is determined through Fermi's golden rule [50, 144]

$$\Gamma_m(E) = \frac{2\pi}{\hbar}|\langle\phi_m|H|\psi_0^{(+)}\rangle|^2 D(E) \quad . \tag{4.18}$$

As before, $\langle\phi_m|H|\psi_0^{(+)}\rangle$ is the matrix element for atom-molecule coupling, $D(E)$ is the density of plane-wave atom-pair states, which is given by

$$D(E) = \frac{V}{(2\pi)^2}\left(\frac{m}{\hbar^2}\right)^{3/2}\sqrt{E} \quad . \tag{4.19}$$

Here, a box-quantization model is assumed with V denoting the box volume. Using Eq. (4.4) with $|C|^2 = 1/V$ and Eq. (4.5), the molecular decay rate can be expressed as

$$\Gamma_m(E) = \frac{2|\Delta B \Delta\mu|}{\hbar}\left(\frac{m\, a_{bg}^2}{\hbar^2}\, E\right)^{1/2} \quad . \tag{4.20}$$

We consider a magnetic-field ramp that is linear in time. The molecule fraction f_m decaying at a particular energy E is given by [59, 141, 145]

$$f_m(E) = \exp\left(-\frac{4|\Delta B|}{3\hbar\left|\frac{dB}{dt}\right|}\sqrt{\frac{ma_{\mathrm{bg}}^2}{\hbar^2}}\,E^{3/2}\right) \quad . \tag{4.21}$$

The mean kinetic energy of a single atom after dissociation is then given by [59, 141]

$$\langle E_{kin}\rangle = \frac{1}{2}\,\Gamma\left(\frac{5}{3}\right)\left(\frac{3\hbar\left|\frac{dB}{dt}\right|}{4|\Delta B|}\sqrt{\frac{\hbar^2}{ma_{\mathrm{bg}}^2}}\right)^{2/3} \quad , \tag{4.22}$$

where Γ is the Euler gamma function with $\Gamma\left(\frac{5}{3}\right) \approx 0.903$. Eq. (4.22) offers the possibility to determine the width ΔB of a Feshbach resonance from a measurement of $\langle E_{kin}\rangle$, because a_{bg} is typically known with better accuracy than ΔB. And unlike our previous method of measuring ΔB introduced in Sec. 3.3, the method suggested by Eq. (4.22) does not depend on knowledge of the initial atomic density distribution.

The probability density g for the velocity $\mathbf{v}$ of the dissociated atoms is calculated from Eq. (4.21), yielding

$$g(\mathbf{v})\mathrm{d}^3v = \frac{3}{4\pi v_0^3}\exp\left(-\frac{|\mathbf{v}|^3}{v_0^3}\right)\,\mathrm{d}^3v \quad , \tag{4.23}$$

where $\langle E_{kin}\rangle = \frac{m}{2}v_0^2\Gamma\left(\frac{5}{3}\right)$. In time-of-flight, this velocity distribution is converted into a position distribution.

In the experiment, the velocity distribution of the molecules before dissociation has a finite width. The result is an offset energy E_0 in Eq. (4.22), but the shape of the velocity distribution Eq. (4.23) is hardly affected, because E_0 is small, typically a few hundred nK compared to dissociation energies of a few μK.

A fit of Eq. (4.23) to absorption images would be cumbersome, because no analytic solution is known for the integral in Eq. (4.23) along one or two coordinate axes. Instead, a two-dimensional Gaussian fit is used to extract $\langle E_{kin}\rangle$ from the images. In order to analyze the error made by this simplification, Eq. (4.23) is numerically integrated along one coordinate axis for a specific value of $\langle E_{kin}\rangle$. The best-fit value $\langle E_{kin}\rangle$ of a corresponding two-dimensional Gaussian fit turns out to be a factor of ~ 1.18 larger than the true value $\langle E_{kin}\rangle$. The kinetic energies in the data analysis are corrected by this factor.

4.2.2 Determining resonance widths

Before performing the experiment, we slightly changed the dipole trap. Previously, an undesired reflection of the horizontal beam from an uncoated inside surface of the science cell caused a weak standing wave. This created a one-dimensional optical lattice with a well-depth of $\sim k_B \times 0.6\ \mu$K, which exceeds typical values of k_BT

B_{res} (G)	ΔB_{fit} (mG)	ΔB_{th} (mG)	ΔB_{scat} (mG)
632	1.3(2)	1.5	–
685	6.2(6)	10	–
912	1.3(2)	1.3	–
1007	210(20)	170(30)	200(30)

Table 4.1: Positions B_{res} and widths ΔB of the Feshbach resonances. ΔB_{fit} is the best-fit value obtained from the data in Fig. 4.8. ΔB_{th} is the theoretical prediction from Ref. [71]. ΔB_{scat} is the result of the scattering-length measurement presented in Sec. 3.3.

and of the chemical potential. The small diffraction peaks visible in Fig. 4.3 are a signature of the weak lattice. Now, the horizontal beam is tilted by a few degrees with respect to the glass surface, thus eliminating the standing wave. This improves the trap loading substantially, because atoms from the wings of the trap are now free to move to the central region. As a consequence, a BEC of typically 6×10^5 atoms can now be held in the crossed dipole trap, with a small thermal fraction of less than 1×10^5 atoms. With the measured trap frequencies of $2\pi \times (80, 110, 170)$ Hz, this results in a BEC peak density of about 5×10^{14} cm^{-3}. As before, ultracold molecules are created by ramping the magnetic field slowly downward through a Feshbach resonances. Again, this is done in free flight, about 2 ms after the release from the dipole trap. The fraction of the population that is converted into and detected as molecules is $\sim 10\%$ for the broad resonances at 685 G and 1007 G, and only $\sim 3\%$ for the narrower resonances at 632 G and 912 G. No molecules could be detected for even narrower resonances with a predicted width of ~ 0.2 mG. For such narrow resonances, the magnetic-field noise is most likely an issue during the creation ramp. After the molecule creation, the Stern-Gerlach field separates the molecules from the remaining atoms. Next, the magnetic field is ramped upward through the Feshbach resonance at variable ramp speed to dissociate the molecules. Then the atoms are allowed to fly freely for up to 11 ms, before an absorption image is taken. The mean kinetic energy is extracted from the images as described above.

Experimental results as a function of ramp speed are shown in Fig. 4.8 for the 4 broadest Feshbach resonances of the state $|1, +1\rangle$. Solid lines show fits of Eq. (4.22) to the data, with the width of the resonance ΔB and the offset energy E_0 as free fit parameters. The best-fit values are shown in Tab. 4.1, using the theory value $a_{bg} = 100.5$ Bohr radii for the state $|1, +1\rangle$ from Ref. [105]. The measured widths agree well with the theoretical predictions and with a previously measured value, both also shown in Tab. 4.1. The good agreement shows that molecule dissociation is a reliable method to determine ΔB.

It is surprising that a width as small as $\Delta B = 1.3$ mG can be measured with our setup, because the magnetic-field noise is most likely larger than this value. The observed linewidths of microwave transitions measured with 50 ms long pulses sets

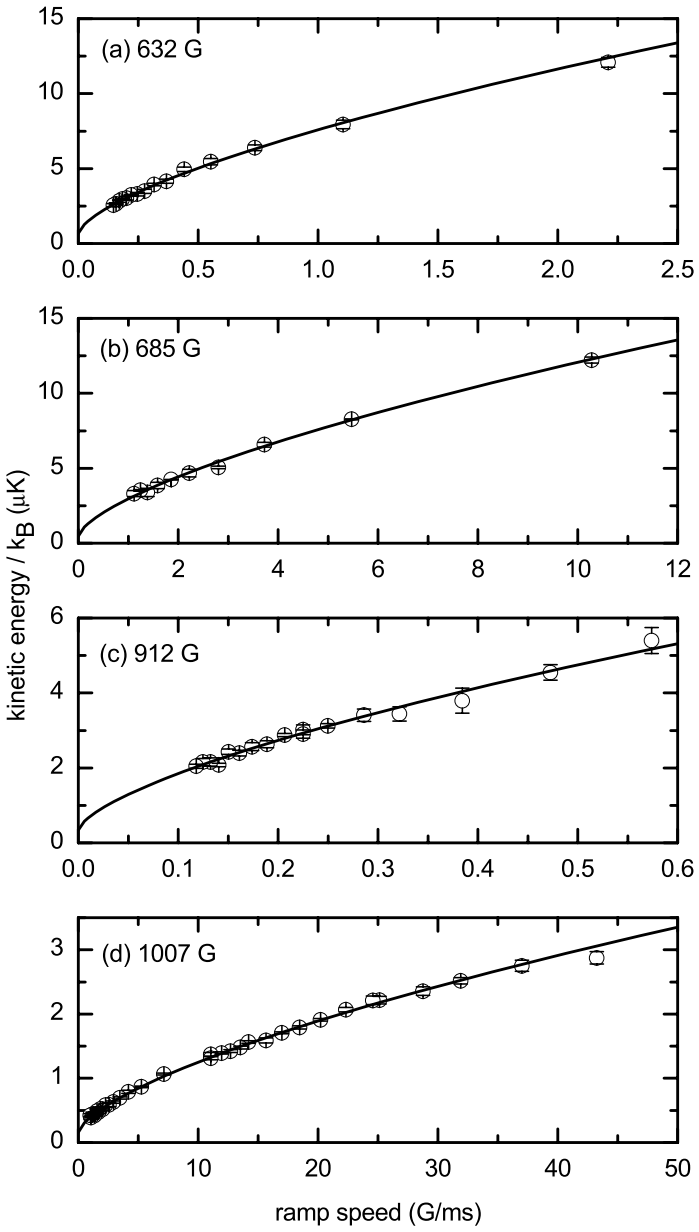

Figure 4.8: Mean kinetic energy per atom as a function of the speed of the dissociation ramp. Parts (a), (b), (c), and (d) were measured for the Feshbach resonances at 632 G, 685 G, 912 G, and 1007 G, respectively. The solid lines show fits of Eq. (4.22) to the data. The best-fit values are shown in Tab. 4.1.

an experimental upper bound on magnetic-field noise of 4 mG (rms). An attempt to directly measure the magnetic-field dependence of the scattering length $a(B)$ for the 632 G or 912 G resonance would therefore most likely suffer strongly from the magnetic-field noise.

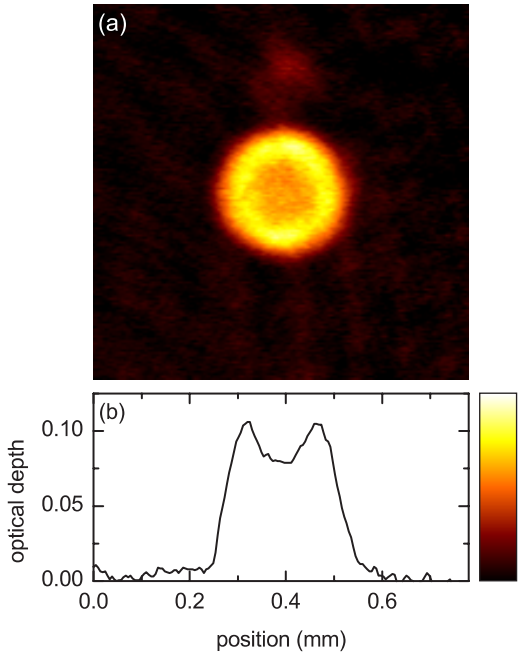

Figure 4.9: (a) (Quasi-)Mono-energetic spherical wave of atoms, created by dissociation of molecules when jumping the magnetic field across the Feshbach resonance. The atoms fly apart on the surface of a hollow sphere. The absorption-imaging beam integrates the three-dimensional density profile along one direction. The observed two-dimensional image therefore shows a ring, with a non-zero density in the center. The image was averaged over ~ 100 experimental shots. (b) Line profile across the center of the image. The dip in the center is clearly visible.

There are presumably two reasons, why such a small ΔB can be measured anyway with the method presented. First, the dissociation process is pretty fast, e.g., $\Gamma_m \sim 10$ kHz for $E = k_B \times 5\ \mu$K at the 912 G resonance. Therefore, low-frequency magnetic-field noise merely shifts the exact time of dissociation but has no effect on the actual ramp speed during the rather short decay time. Second, by choosing fast enough ramp speeds, the experiment is operated in a regime where the relevant decay happens at magnetic fields that are pretty far away from B_{res}. A typical decay energy of $E = k_B \times 5\ \mu$K corresponds to $B - B_{res} \sim 25$ mG for the 912 G resonance. Here, the magnetic-field noise has little effect on the molecule-decay rate due to the $\sqrt{E}$ scaling (see Eq. (4.20)). Detailed calculations on the influence of magnetic-field noise on the dissociation of Feshbach molecules confirm the robustness of the method [146].

4.2.3 Mono-energetic atom pairs

If the magnetic-field is jumped across the Feshbach resonance as fast as possible to a final value B_f and held there, hardly any molecules decay during the jump. Instead,

they all decay at B_f, thus creating atoms with a fixed amount of kinetic energy. Hence, the atoms fly apart on the surface of a hollow sphere during the subsequent free flight. In fact, the shell of the sphere is expected to have a finite width that is determined by the decay rate $\hbar\Gamma_m$.

We performed such an experiment by jumping the magnetic field across the Feshbach resonance at 685 G after creating molecules. In the experiment, the jump is in fact a very fast field-ramp with a slope of ~ 0.1 G/μs. The laser beam for absorption imaging of the dissociated atom pairs integrates the density distribution of the hollow sphere along its propagation direction. In the two-dimensional absorption image, the result is a ring structure, with a non-zero density in the center. Such an image is shown in Fig. 4.9(a).

The initial momentum spread of the molecules leads to a further broadening of the atomic density distribution around the ring. However, the contrast is still good enough to see a clear dip in the center of the line profile in Fig. 4.9(b). The data were taken with 5.5 ms time-of-flight after the dissociation and with $B_f - B_{res} \sim 40$ mG corresponding to $\Gamma_m \sim 20$ kHz.

Technically, the creation of a sharp corner between the magnetic-field jump and the plateau at B_f is difficult. The experimental requirements concerning the sharpness of this corner are more stringent with broader resonances because of the faster molecule-decay rates. Presumably, this prevented us from observing a dip as in Fig. 4.9(b) at the 1007 G resonance. There, the bandwidth of the servo that controls our magnetic field is not sufficient.

The scheme with the jump in the magnetic field can be generalized by using an arbitrary shape of the dissociation ramp. That way, the time and energy dependence of the outgoing atomic wavefunction can be tailored at will.

Chapter 5

Dissociation into s and d waves

At the end of the previous chapter, a rapid change of the magnetic field led to non-adiabatic molecule dissociation, thus adding a significant amount of energy to the outgoing atoms. The question arises, if higher partial waves corresponding to higher kinetic energies can be populated with the same method. Feshbach resonances caused by s-wave bound states couple predominantly to the s-wave continuum due to the exchange interaction. Hence, they do not lead to a noticeable population of higher partial waves. In contrast, a bound state with e.g. d-wave character, in combination with a fast magnetic-field ramp might populate an outgoing d wave. For such a scenario, a series of questions arises:

- If a d wave is created, will there still be an s-wave component?
- Do the different partial waves form a coherent superposition or an incoherent mixture?
- What determines the branching ratio and the phase?
- How fast is the dissociation process?

The answers are nontrivial. This subject has not been studied before, neither in experiment nor in theory. Section 5.1) introduces a corresponding experiment that we performed [147]. For understanding our observations we developed new theory [148] which is summarized in Sec. 5.2.

5.1 Experiment

The section starts with a discussion of a measurement of the molecule-dissociation rate as a function of magnetic field near a d-wave Feshbach resonance (Sec. 5.1.1). The measured dissociation rate shows a resonant enhancement due to a d-wave shape resonance, which is introduced in Sec. 5.1.2. Time-of-flight images reveal the angular distribution of the dissociated atom pairs (Sec. 5.1.3). The images are analyzed using computed tomography, which is explained in Sec. 5.1.4.

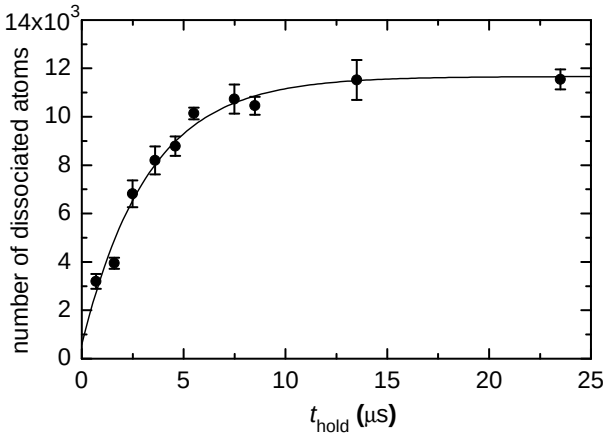

Figure 5.1: Time-resolved molecule decay near the 632-G Feshbach resonance. The measured number of dissociated atoms is shown as a function of hold time t_{hold} at $B - B_{res} = 0.97$ G. An exponential fit (solid line) yields a decay rate of $\Gamma = 310$ kHz.

5.1.1 Dissociation rate

In the experiment, we use a Feshbach resonance at $B_{res} \approx 632$ G which is caused by a d-wave bound state and has a measured width of 1.3 mG (see Tab. 4.1). The experimental sequence begins with the creation of molecules in free flight by a slow magnetic-field ramp across the resonance. Unconverted atoms are spatially separated from the molecules using the Stern-Gerlach technique, described in Sec. 4.1.3. Next, the molecules are dissociated back into unbound atom pairs by jumping the magnetic field to a value $B > B_{res}$ and holding it there for a variable time t_{hold}. During t_{hold}, population in the molecular state decays exponentially with a rate $\Gamma(B)$, which depends on the value of B. After t_{hold}, the magnetic field is switched off rapidly, which stops the dissociation process. After 0.85 ms time of flight (counting from the dissociation), an absorption image is taken. Molecules that did not decay during t_{hold} are invisible in the image.

The number of dissociated atoms is extracted for a series of images at different values of t_{hold} for B, as shown in Fig. 5.1. An exponential fit yields the dissociation rate $\Gamma(B)$. Repeating this procedure for different values of B gives the dissociation rate shown in Fig. 5.2. The data exhibit a clear resonance structure near 1.3 G, where the dissociation rate reaches values of up to ~ 1 MHz.

Experimentally, such high dissociation rates are difficult to measure. The servo used to control B must create slopes on the order of 1 G/μs and have a settling time of ~ 1 μs. Designing such a servo is technically challenging. Moreover, with the high ramp-speeds of 1 G/μs, eddy currents become an issue. In the experiment, the eddy currents were determined by investigating molecule dissociation near the dissociation threshold. There, the eddy currents lead to a delay in the onset of decay. Systematic measurements of this delay show that a step-like change of B creates eddy currents

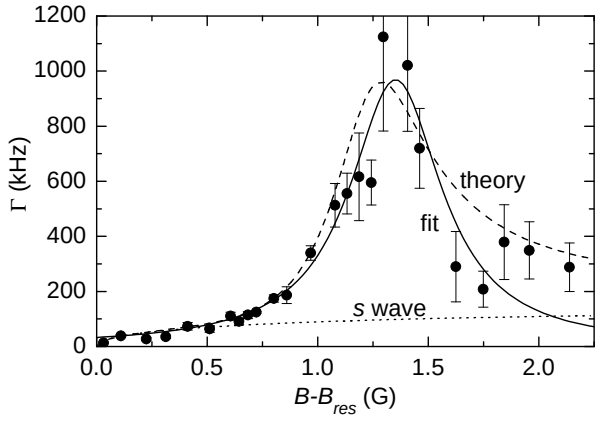

Figure 5.2: Molecule dissociation rate Γ as a function of magnetic field B with respect to the position of the Feshbach resonance B_{res}. The experimental data for the total rate (circles) clearly show a resonant enhancement near 1.3 G, which is due to a d-wave shape resonance (see Sec. 5.1.2). The dashed (dotted) line shows the prediction for the total (s-wave) dissociation rate from a coupled-channels calculation. The s-wave dissociation is not affected by the shape resonance. The solid line is a Lorentzian fit to the data according to the simple model in Eq. (5.1).

that initially cancel $\sim 15\%$ of the step height and exponentially ring down with a $1/e$-time of $\sim 25\mu$s. The eddy currents were accounted for in the data analysis.

5.1.2 d-wave shape resonance

The resonant enhancement of the dissociation rate near 1.3 G in Fig. 5.2 is due to a d-wave shape resonance in the open channel. Fig. 5.3 illustrates the situation. The shape resonance is caused by a quasi-bound state which is localized behind the d-wave centrifugal barrier. Unlike a true bound state, the energy of this shape-resonance state lies above the threshold of the open channel. As a consequence, any population in the shape-resonance state quickly decays into the d-wave continuum by tunneling through the centrifugal barrier.

In the dissociation experiment, the shape-resonance state mediates the decay into the d wave. This can be understood as follows: For magnetic-field values slightly above B_{res}, the energy of the molecular state lies just above the open-channel threshold. Here, the molecular state preferentially decays into the s-wave continuum. Decay into the d wave is suppressed due to the centrifugal barrier. The situation changes when the energy of the molecular state matches the energy of the shape-resonance state. Then population is transferred from the molecular state to the shape-resonance state. From there, the population rapidly decays into d-wave atom pairs by tunneling through the centrifugal barrier. The coupling between the two states is strong due to the good spatial overlap between the two short-

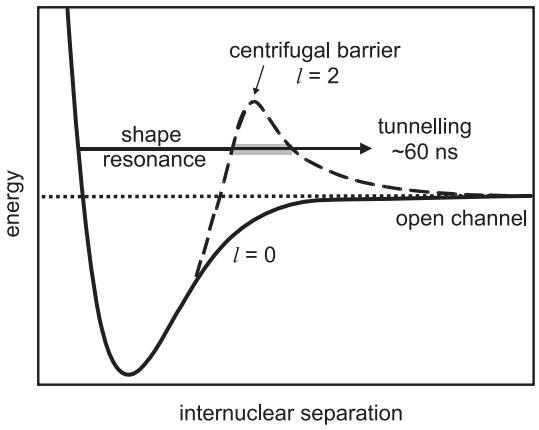

Figure 5.3: Scheme of the d-wave shape resonance. In ^{87}Rb, the d-wave centrifugal barrier of the open-channel potential supports a quasi-bound state, the shape-resonance state. It lies ~ 250 μK above the dissociation threshold. Any population in the shape-resonance state decays rapidly within ~ 60 ns into the d-wave continuum by tunneling through the centrifugal barrier. Note that the energies in the graph are not to scale.

ranged (quasi-)bound states. This explains the significant increase in the measured dissociation rate near 1.3 G.

The two-step dissociation process mediated by the shape-resonance state can be described by a simple analytic model. In the first step, the interaction Hamiltonian H transfers population from the molecular state $|\phi_m\rangle$ to the shape-resonance state $|\phi_{shape}\rangle$. This is described by a generalized Rabi frequency $\Omega = (2/\hbar)|\langle\phi_{shape}|H|\phi_m\rangle|$. In the second step, the population tunnels with a rate Γ_{shape} from $|\phi_{shape}\rangle$ into the continuum of unbound atom pair states. One can show that for $\Omega \ll \Gamma_{shape}$ the molecular state decays exponentially with a rate [149]

$$\Gamma(B) = \frac{\Omega^2}{\Gamma_{shape}} \left[1 + \left(2\,\frac{E_{shape} - E_m(B)}{\hbar\Gamma_{shape}}\right)^2\right]^{-1} , \tag{5.1}$$

where E_{shape} and E_m are the energies of the shape-resonance state and the molecular state, respectively. E_m depends on B, while Γ_{shape}, E_{shape}, and Ω in this simple model do not. For the magnetic-field range considered here, $E_m = \Delta\mu(B - B_{res})$.

In the experiment, $\Delta\mu$ is deduced from the kinetic energy released during dissociation. This energy is extracted from time-of-flight images of the dissociated atom pairs (see Sec. 5.1.3). With this method, we obtain $\Delta\mu = k_B \times 230(18)$ μK/G. Alternatively, the Stern-Gerlach method from Sec. 4.1.5 could be used.

$\Gamma(B)$ in Eq. (5.1) is a Lorentzian, which is fit to the data in Fig. 5.2. Using the above value for $\Delta\mu$, the best-fit parameters are $E_{shape} = k_B \times 312(25)$ μK, $\Gamma_{shape} = 15(3)$ MHz, and $\Omega = 2\pi \times 0.61(7)$ MHz. Hence, energy and lifetime of the shape resonance as well as the Rabi frequency can be extracted from experimental

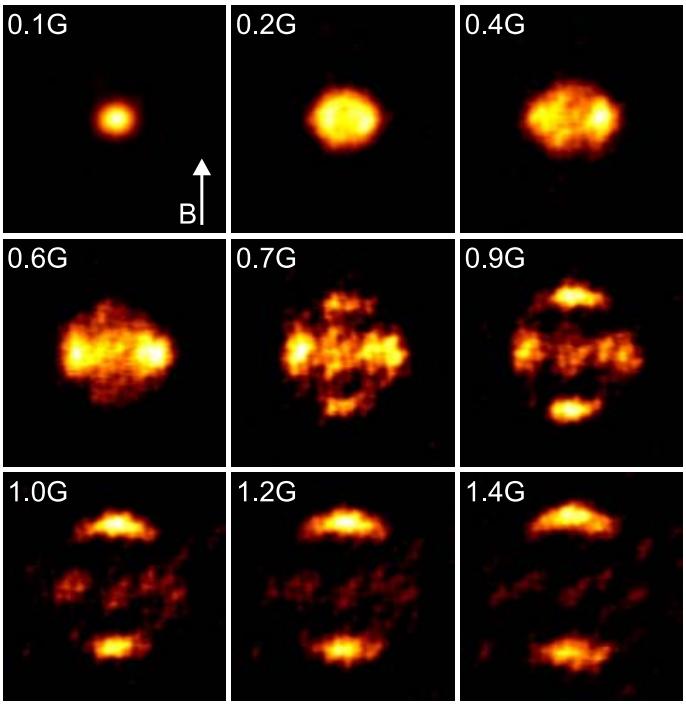

Figure 5.4: Time-of-flight absorption images of unbound atoms obtained by molecule dissociation. The images were taken at different values of $B - B_{res}$, but at the same expansion time of 0.85 ms after dissociation. The magnetic field is vertical in the images. The interference between the s and d partial wave undergoes a change in relative phase and amplitude. At 0.1 G, the dissociation is mostly s wave, producing a circle. For higher magnetic fields, both partial waves are populated. From 0.2 to 0.6 G, the atom emission *along* **B** is suppressed, whereas between 1.0 and 1.4 G the opposite relative phase in the interference suppresses emission *perpendicular* to **B**. At 0.7 and 0.9 G, the relative phase is such that neither component is strongly suppressed. The typical radius reached by the atoms during the constant time of flight increases with increasing B, thus indicating an increase of the kinetic energy released in the dissociation.

data without making any reference to the coupled-channels calculation that will be discussed in Sec. 5.2. Note that previously, the shape resonance in ^{87}Rb was seen in a photoassociation experiment [111] and in scattering experiments [150–152]. Here, we probe the shape resonance by molecule dissociation.

5.1.3 Interference between s and d waves

Figure 5.4 shows time-of-flight images of the dissociated atoms for different values of the magnetic field. The images exhibit spatial interference patterns where only the two partial waves with rotational quantum numbers $(l, m_l) = (0, 0)$ and $(2, 0)$

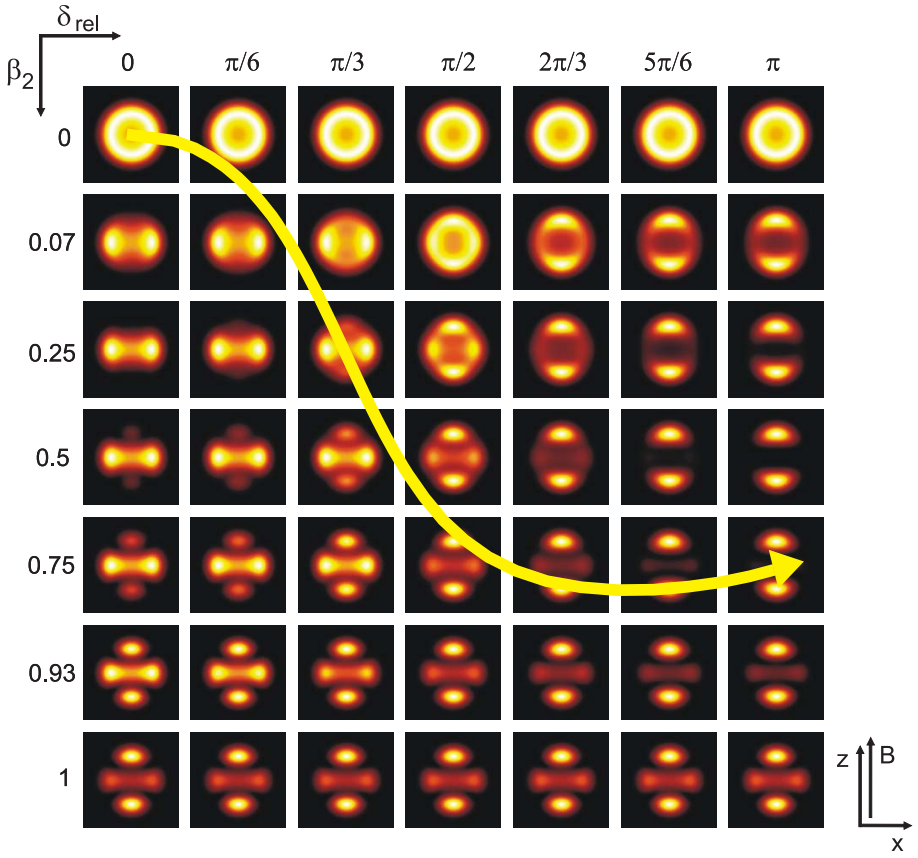

Figure 5.5: Predicted interference patterns. The images are calculated by integrating the modulus squared of the wavefunction Eq. (5.2) along the y axis. The various images represent different values of the branching ratio into the d wave, β_2, and of the relative phase, δ_{rel}. A relative phase near 0 (π) suppresses emission parallel (perpendicular) to the magnetic field **B**. The arrow indicates the path for a magnetic-field scan predicted by the coupled-channels calculation in Sec. 5.2.

contribute.[1]

Hence, the interference pattern can be described by the following wavefunction

$$\psi_{decay}(\mathbf{r}) = g(r,t)\left(\sqrt{\beta_0}Y_{00} - e^{i\delta_{rel}}\sqrt{\beta_2}Y_{20}(\vartheta)\right) \quad , \tag{5.2}$$

where $Y_{lm_l}(\vartheta,\varphi)$ are spherical harmonics. The real numbers β_l and δ_{rel} characterize the amplitudes of the partial waves and their relative phase, and $g(r,t)$ is the radial

[1]This can be explained based on the following arguments: The interaction Hamiltonian conserves parity so that Δl is even. Moreover, due to rotational symmetry around the z axis (along B), $m_l + m_{f1} + m_{f2}$ is conserved, where the magnetic quantum numbers of the atoms are m_{f1}, m_{f2}. These are $+1$ each, before and after the interaction. Hence m_l is identical before and after the interaction. Since the incoming wave in the association is an s wave, all outgoing partial waves must have $m_l = 0$ and even l. Finally, partial waves with $l > 2$ are negligible in the low-energy range considered here.

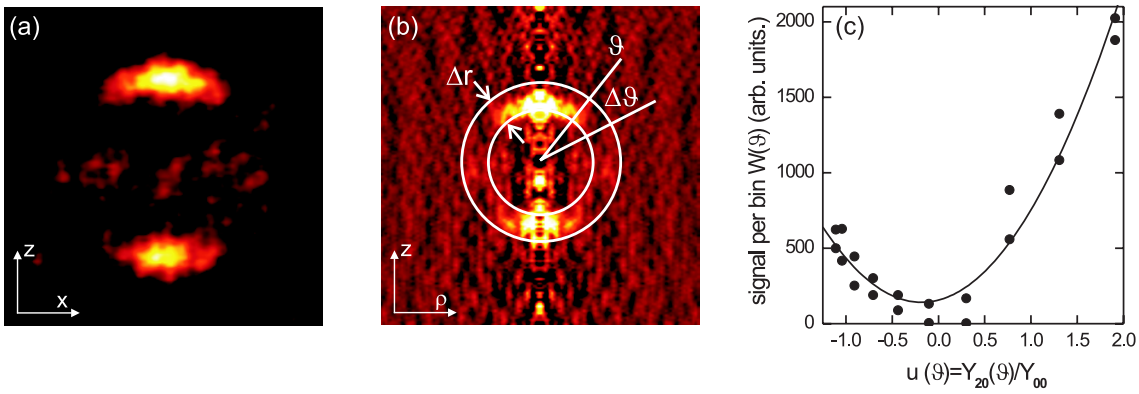

Figure 5.6: Analyzing interference patterns. (a) Absorption image at $B = 1.2$ G. (b) Reconstructed 3D distribution in cylindrical coordinates obtained by computed tomography. For further processing, the image is divided into 20 angular bins $\Delta\vartheta$. Note, that only a small radial region Δr is used for further data analysis. (c) The angular distribution $W(\vartheta)$ is extracted. A fit with a parabola yields the branching ratio into the d wave β_2 and the relative phase δ_{rel} as fit parameters.

part of the wavefunction. $g(r,t)$ is normalized such that $\beta_0 + \beta_2 = 1$, which implies that β_l is the branching ratio for the decay into the l-th partial wave. In the experiment, the modulus squared of the wavefunction Eq. (5.2) is observed.

Figure 5.5 shows a prediction for interference patterns based on Eq. (5.2). In the calculation, the radial distribution was assumed to be a Gaussian centered around some finite radius r_0 which is identical for all the images. Some of the experimentally observed images in Fig. 5.4 strongly resemble the theoretical images in Fig. 5.5. General features, such as a change in the preferred emission direction can be found in both the experimental and the theoretical pictures. The curved arrow in Fig. 5.5 indicates the path that is expected to be followed in the experiment. It was obtained from the coupled-channels calculation in Sec. 5.2.

5.1.4 Branching ratio and relative phase

In order to go beyond the qualitative comparison between Figs. 5.4 and 5.5, we now extract the branching ratio and the relative phase from the images in Fig. 5.4. To this end, we first reconstruct the 3D density distribution using computed tomography [153]. The method is well-known from medical imaging and was adapted before to clouds of cold atoms by two other groups [151, 154]. Due to the cylindrical symmetry around the z axis (magnetic-field axis), the radial density distribution can be reconstructed in cylindrical coordinates from [151]

$$n(\rho, z) = \frac{1}{4\pi} \int_{-\infty}^{\infty} dk_x \tilde{n}(k_x, z) J_0(k_x \rho) |k_x| \quad . \tag{5.3}$$

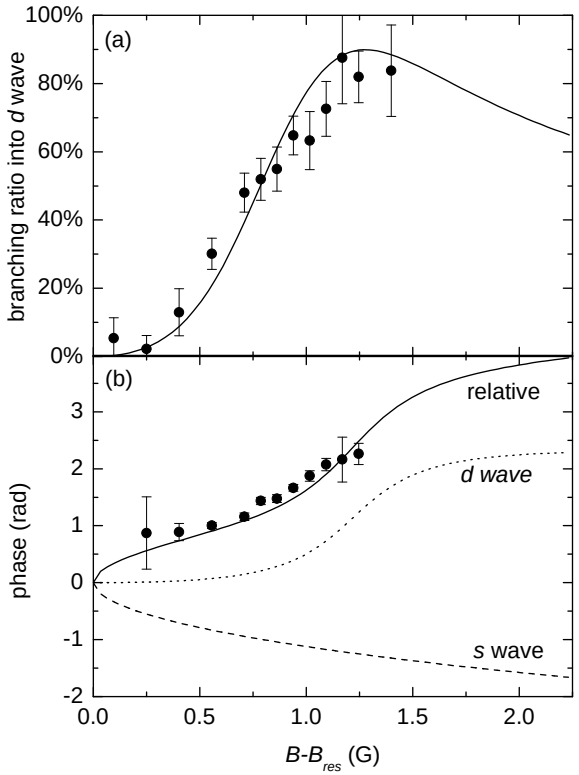

Figure 5.7: Parameters extracted from the spatial interference patterns. (a) Branching ratio for decay into the d wave. Again, the d-wave shape resonance is clearly visible. (b) Partial-wave phases and relative phase. The solid, dashed, and dotted lines show the theoretical prediction for the relative phase $\delta_{rel} = \delta_2^{bg} - \delta_0^{bg}$, the s-wave phase δ_0^{bg}, and the d-wave phase δ_2^{bg}, respectively. Experimental data (circles) agree well with the theory (solid line) in (a) and (b).

Here, $\rho = \sqrt{x^2 + y^2}$ is the radial coordinate, and J_0 is the zeroth-order Bessel function. $\tilde{n}(k_x, z)$ is the 1D Fourier transform of the 2D density distribution $n(x, z)$ along the x direction

$$\tilde{n}(k_x, z) = \int_{-\infty}^{\infty} dx e^{-ik_x x} n(x, z) \quad . \tag{5.4}$$

Parts (a) and (b) of Fig. 5.6 show a 2D absorption image and the corresponding reconstructed 3D density distribution $n(\rho, z)$, respectively.

Next, the 3D density is sorted into 20 angular bins to obtain the probability $W(\vartheta)$ for finding an atom at angle ϑ. In order to improve the signal-to-noise ratio, we consider only a small radial region Δr for further data processing. The resulting angular distribution $W(\vartheta)$ is shown in Fig. 5.6(c). Note that $W(\vartheta)$ is plotted as a function of $u(\vartheta) = Y_{20}(\vartheta)/Y_{00}$. The reason for this becomes clear when rewriting

the modulus squared of the wavefunction Eq. (5.2) as

$$|\psi_{decay}(\vartheta)|^2 = |g(r,t)|^2 |Y_{00}|^2 \left(\beta_0 - 2\sqrt{\beta_2\beta_0}\cos\delta_{rel}\; u(\vartheta) + \beta_2\; u^2(\vartheta)\right) \quad , \tag{5.5}$$

with $\beta_0 = 1 - \beta_2$. Hence, using a parabola as the fit function to the angular distribution $W(\vartheta)$ yields the fit parameters β_2 and δ_{rel}.

These are shown in Fig. 5.7. The branching ratio clearly shows the enhanced decay into the d wave due to the shape resonance. In addition, the relative phase has an inflection point, a signature of a (scattering) resonance [148]. Note, that for β_2 close to 0 or 100%, the fit cannot reliably determine the relative phase δ_{rel}.

5.2 Theoretical analysis

The key to a theoretical description of the dissociation process lies in the observation that the dissociation is "half a collision". In a full collision, two atoms come together and then separate again. In the association and dissociation using Feshbach resonances, the experimenter can "freeze" the population in the middle, after the atoms came together. He can even choose, how much time is spent between association and dissociation. Still, the association and dissociation can be regarded as the first and second half of one collision. The concept of a half collision proved useful in other contexts before (see e.g. Refs. [155–158]). Unfortunately, the models developed there are not directly applicable here. We therefore had to develop our own model, in order to link the dissociation experiment quantitatively to scattering theory. The key ideas are summarized here. For more details see Ref. [148].

5.2.1 Scattering *gedanken* experiment

In the following, we consider a *gedanken* experiment with a colliding atom pair with kinetic energy E in the relative motion in the presence of a magnetic field B near the 632 G Feshbach resonance.

For treating multi-channel scattering, it is very convenient to introduce the S-matrix (or scattering matrix) [107, 119]. The S matrix can be defined by formulating the boundary condition for multi-partial-wave scattering as

$$\psi_{l'}^{(+)} \xrightarrow{r\to\infty} (-1)^{l'} \frac{e^{-ikr}}{r} Y_{l'0}(\vartheta) \; - \; \frac{e^{ikr}}{r} \sum_{l=0}^{\infty} S_{ll'}\, Y_{l0}(\vartheta) \quad . \tag{5.6}$$

Here, l' denotes the incoming partial wave. The outgoing partial waves l have complex amplitudes $S_{ll'}$, which constitute the S-matrix. In the above expression, $m_l = 0$ for all outgoing partial waves, as is the case in the experiment. Note that the above boundary condition is different from the one in Sec. 3.1.1, where an incoming plane wave and an outgoing spherical wave were considered.

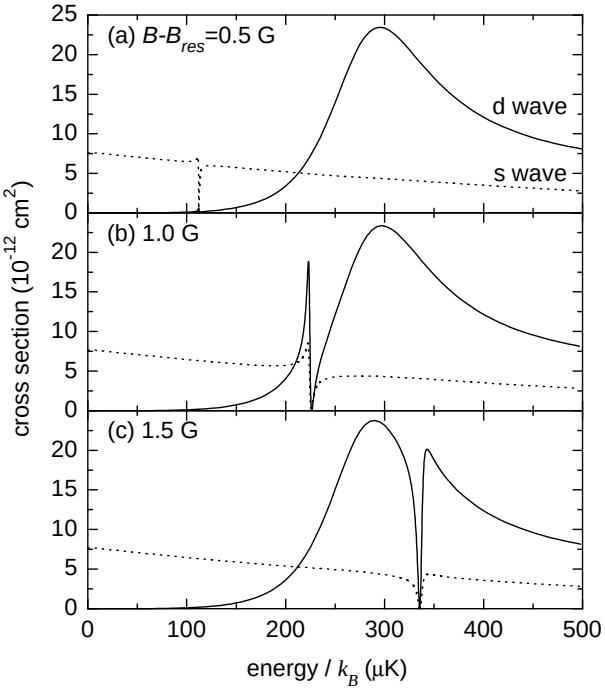

Figure 5.8: Combination of a shape resonance and a Feshbach resonance for scattering of ^{87}Rb in state $|1,+1\rangle$. The partial-wave cross sections for the s wave (dotted line) and the d wave (solid line) are shown. The magnetic field B is held at different values above the zero-energy resonance position $B_{res} \sim 632$ G. The Feshbach resonance is much narrower than the shape resonance. By changing B, the position of the Feshbach resonance can be tuned through the shape resonance.

Since the number of particles is conserved, the S-matrix is unitary. In addition, realistic Hamiltonians in atomic physics are invariant under time reversal, which implies that the S matrix is symmetric. The scattering amplitude $f(\vartheta)$ (see Sec. 3.1.2) can be expressed in terms of the S-matrix as

$$f(\vartheta) = \frac{1}{2ik} \sum_{l,l'=0}^{\infty} \sqrt{4\pi(2l'+1)}\,(S_{ll'} - \delta_{ll'})\,Y_{l0}(\vartheta) \quad . \tag{5.7}$$

Typically, the S-matrix has only few non-zero elements due to symmetry. For a spherically symmetric potential, the S-matrix is diagonal and is given by $S_{ll} = e^{2i\delta_l}$, where the scattering phases δ_l have been introduced before in Sec. 3.1.2. In this case, Eq. (5.7) reduces to Eq. (3.7).

A coupled-channels calculation [121, 159] yields the S-matrix elements $S_{ll'}$ with $l, l' = 0, 2$ as a function of collision energy E and magnetic field B near the Feshbach resonance at $B_{res} = 632$ G. From that, the scattering cross section $\sigma(E, B)$ can be

determined. Figure 5.8 shows calculated s and d-wave cross sections as a function of collision energy for an incoming plane wave and for three different magnetic-field values $B - B_{res}$. The most prominent feature is the broad shape resonance in the d-wave channel. Its position does not depend on magnetic field. In contrast, the energy at which the much narrower Feshbach resonance occurs changes with magnetic field. Therefore, the Feshbach resonance can be tuned through the shape resonance.

According to the theory of multi-channel scattering resonances, near resonance the S-matrix elements are expected to follow an analytic behavior of the form [107, 119, 148]

$$S_{ll'}(E,B) = e^{i[\delta_l^{bg}(E)+\delta_{l'}^{bg}(E)]}\left(\delta_{ll'} - \frac{i\hbar\Gamma_{ll'}(E)}{E - E_m(B) + \frac{i}{2}\hbar\Gamma(E)}\right) \quad . \tag{5.8}$$

Here, $\delta_l^{bg}(E)$ denotes the background scattering phase for the l-th partial wave, where background means for magnetic fields far away from the Feshbach resonance. Note that the shape resonance is contained in the background phase $\delta_2^{bg}(E)$ of the d wave. $\Gamma(E)$ is the total decay rate of the molecular state. The energy of the molecular state $E_m(B)$ was introduced before (see Eq. (3.17)). As we will see in Sec. 5.2.2, the Γ_{ll} can be interpreted as the decay rate into the l-th partial wave. For the S-matrix to be unitary and symmetric, the $\Gamma_{ll'}$ must all be real and satisfy the relations

$$\Gamma_{02} = \pm\sqrt{\Gamma_{00}\Gamma_{22}} \tag{5.9}$$

$$\Gamma = \Gamma_{00} + \Gamma_{22} \; . \tag{5.10}$$

The correct sign in the first expression has to be determined from the coupled-channels calculation. In our case, we find a minus sign. Eq. (5.10) expresses the fact, that the total decay rate Γ is the sum of the partial decay rates.

Next, for any given E, we fit Eq. (5.8) for variable B to the S-matrix elements obtained from our coupled-channels calculation [148]. The fits match the S-matrix extremely well as shown in Fig. 5.9. The open-channel physics, including the shape resonance, is independent of B and is therefore included in the energy-dependent fit parameters $\delta_l^{bg}(E)$ and $\Gamma_{ll'}(E)$. Furthermore, the combination of the fits for different energies yields $\Delta\mu = k_B \times 224\ \mu$K/G.

As mentioned earlier, the kinetic energy E of the atom pairs after dissociation is $E = E_m(B)$. Therefore the energy-dependent fit-parameters $\delta_l^{bg}(E)$ and $\Gamma_{ll'}(E)$ for the *gedanken* experiment become magnetic-field dependent parameters in the dissociation experiment, $\delta_l^{bg}(B)$ and $\Gamma_{ll'}(B)$. The link between scattering and decay is discussed in the following.

5.2.2 Link between scattering and decay

The link between the scattering *gedanken* experiment and the dissociation experiment can be established from evaluating the different terms in the asymptotic form

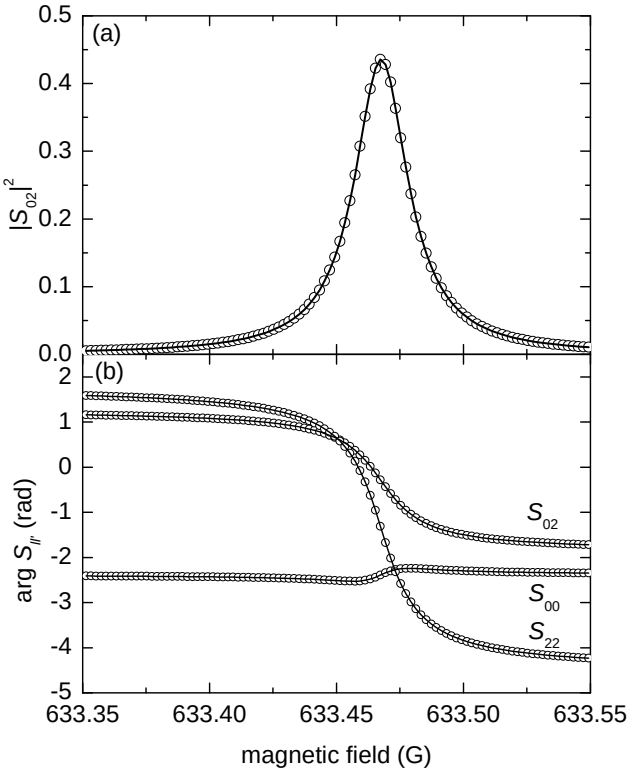

Figure 5.9: Fitting to the S-matrix elements. The theoretically expected Breit-Wigner form Eq. (5.8) is fitted to the results of a coupled-channels calculation ($\circ$). Modulus squared (a) and phase (b) of the S-matrix elements are plotted as a function of magnetic field for a fixed energy of $k_B \times 255\ \mu$K. The fit curves (solid lines) agree so well with the numerical data that they are hardly visible in the plot.

of the regular scattering wavefunction

$$\psi_{l'}^{(+)}(\mathbf{r}) \stackrel{r\to\infty}{\longrightarrow} (-1)^{l'} \frac{e^{-ikr}}{r}\, Y_{l'0}(\vartheta) - \frac{e^{ikr}}{r} \sum_l S_{ll'}^{bg} Y_{l0}(\vartheta) - \frac{e^{ikr}}{r} \sum_l S_{ll'}^{res} Y_{l0}(\vartheta)\ , \quad (5.11)$$

where we assume in the *gedanken* experiment that only one partial wave l' is populated initially. Here, the S-matrix is split into a background part and a resonant part $S_{ll'} = S_{ll'}^{bg} + S_{ll'}^{res}$ with $S_{ll'}^{bg} = e^{2i\delta_l^{bg}} \delta_{ll'}$.

Hence, the scattering wavefunction consists of three parts: an incoming wave, an outgoing background wave, and an outgoing resonant wave. The resonant part is due to particles that make the transition to the molecular state and subsequently decay back into the open channel. The Stern-Gerlach separation removes all incoming flux and along with it the background scattered wave. These two terms therefore need to be removed from the scattering state Eq. (5.11) in order to describe the decay

wavefunction

$$\psi_{decay}(\mathbf{r}) \overset{r\to\infty}{\longrightarrow} -\frac{e^{ikr}}{r}\sum_{l} S^{res}_{ll'}Y_{l0}(\vartheta)\ . \tag{5.12}$$

Inserting the resonant part of the S-matrix Eq. (5.8) and Eq. (5.9) into Eq. (5.12) and setting $l' = 0$, yields the following expression for the decay wavefunction

$$\psi_{decay}(\mathbf{r}) \overset{r\to\infty}{\longrightarrow} \tilde{g}(r,E)\ \left(\sqrt{\beta_0}Y_{00} - e^{i\delta_{rel}}\sqrt{\beta_2}Y_{20}(\vartheta)\right)\ . \tag{5.13}$$

$\tilde{g}(r,E)$ is the radial wavefunction and is related to $g(r,t)$ in Eq. (5.2) through a Fourier transform. Furthermore, the relative phase of the decaying partial waves is abbreviated as

$$\delta_{rel} = \delta_2^{bg} - \delta_0^{bg} \tag{5.14}$$

and the branching ratio into the l-th partial wave as

$$\beta_l(B) = \Gamma_{ll}(B)/\Gamma(B)\ . \tag{5.15}$$

The last expression implies that $\Gamma_{ll}(B)$ represents the partial decay rate into the l-th partial wave.

The theoretical results for the decay rate, branching ratio, and the phases were already shown in Fig. 5.2 and Fig. 5.7. The good agreement between theory and experiment without any free fit parameters supports our model.

Finally, the parameters of the simple model Eq. (5.1) can be extracted from the full theory. The d-wave decay rate $\Gamma_{22} = \Gamma - \Gamma_{00}$ is the difference between the total and the s-wave decay rate, both shown in Fig. 5.2. The maximum of Γ_{22} is located at 1.28 G corresponding to $E_{shape} = k_B \times 287\ \mu$K. The value and the curvature of $\Gamma_{22}(B)$ at the maximum correspond to $\Gamma_{shape} = 17$ MHz and $\Omega = 2\pi \times 0.61$ MHz. These numbers agree well with the values obtained by fitting the simple model Eq. (5.1) to the experimental data.

Chapter 6

A Mott-like state of molecules

As was pointed out in Chap. 4, the Feshbach molecules associated from bosonic atoms strongly suffer from inelastic collisions with other particles. This makes further experiments difficult. A solution to this problem is offered by placing the molecules one-by-one at the sites of a three-dimensional optical lattice. This isolates the molecules from each other and therefore suppresses inelastic collisions as demonstrated in a recent experiment [74].

But molecules in optical lattices are interesting for more than just this reason. During the past few years, quantum gases in optical lattices have attracted a great deal of interest [12]. They resemble solid-state systems but with parameters that can be controlled in realtime. Hence, open problems from solid-state physics might be accessed with lattice systems. A famous example in the case of atoms is the realization of the quantum phase transition from a superfluid to a Mott-insulator state [103], which also plays a prominent role in the present chapter. Molecules, in particular polar ones, offer the prospect to access a new class of solid-state Hamiltonians [160–162]. Moreover, certain schemes for quantum information processing suggest to use molecules in optical lattices as qubits [163, 164].

Here, we present a first step towards these goals, namely the realization of a Mott-like state of molecules [76, 165]. The experiment starts with an atomic Mott insulator with exactly two atoms per lattice site. Next, the atoms are associated to molecules using a Feshbach resonance. The resulting quantum state resembles a Mott insulator state, insofar as it has exactly one molecule per lattice site. Before turning our attention to this experiment in Sec. 6.3, we discuss the physics underlying the atomic Mott insulator in Sec. 6.1 and demonstrate its experimental realization in Sec. 6.2.

6.1 Atomic Mott insulator

This section introduces the Bose-Hubbard Hamiltonian describing bosonic atoms in optical lattices [166]. The ratio of interaction energy to tunneling energy determines whether the ground state of that Hamiltonian is a superfluid or an insulator. Both

regimes are treated separately. The discussion is restricted to the concepts relevant for our experiment. More details can be found in the literature [97, 166–168].

6.1.1 Bose-Hubbard model

For describing atoms in optical lattices, it is convenient to work in a basis of Wannier functions [98]

$$w_n(\mathbf{r}-\mathbf{r}_i) = \mathcal{N}^{-1/2} \sum_{\mathbf{q}} e^{-i\mathbf{q}\mathbf{r}_i}\ \Psi_{\mathbf{q}}^{(n)}(\mathbf{r})\ . \tag{6.1}$$

$\mathcal{N}$ is a normalization constant and the $\Psi_{\mathbf{q}}^{(n)}(\mathbf{r})$ are Bloch waves generalized to three dimensions (compare Sec. 2.4.2). The Wannier functions represent particles that are maximally localized at lattice sites $\mathbf{r}_i$. If the energies involved in the dynamics of the system are much smaller than the band gap between the two lowest bands, only Wannier functions of the lowest band ($n = 0$) need to be considered.

In Sec. 3.1.4, a Hamiltonian in second quantization was introduced to describe a many-body system of bosons with binary interactions. In the lattice, the corresponding bosonic field operator $\hat{\Psi}$ is expanded in the basis of Wannier functions as

$$\hat{\Psi}(\mathbf{r}) = \sum_i \hat{a}_i w(\mathbf{r}-\mathbf{r}_i)\ \ , \tag{6.2}$$

where the operator $\hat{a}_i$ annihilates a boson on the i-th lattice site. Inserting expansion Eq. (6.2) into the Hamiltonian Eq. (3.15) finally yields the Bose-Hubbard Hamiltonian [166, 167]

$$\hat{H} = \sum_i (\epsilon_i - \mu)\,\hat{n}_i - J \sum_{<i,j>} \hat{a}_i^\dagger \hat{a}_j + \sum_i \frac{1}{2} U \hat{n}_i\,(\hat{n}_i - 1)\ \ . \tag{6.3}$$

Here, $\hat{n}_i = \hat{a}_i^\dagger \hat{a}_i$ is the operator for the particle number at site i.

The first term in the Bose-Hubbard Hamiltonian Eq. (6.3) originates from the external confinement of the particles, which causes an energy offset ϵ_i at the i-th lattice site. It also includes the chemical potential μ. In the following we will first neglect the external confinement and discuss a homogeneous system with $\epsilon_i = 0$ for all i.

The second term describes the tunneling of atoms between neighboring lattice sites. Note that the summation is carried out only over nearest neighbors. The tunneling rate J between sites i and j is given by

$$J = -\int \mathrm{d}^3 r\ w(\mathbf{r}-\mathbf{r}_i)\ \left(-\frac{\hbar^2\nabla^2}{2m} + V_{lat}(\mathbf{r})\right)\ w(\mathbf{r}-\mathbf{r}_j)\ \ , \tag{6.4}$$

where $V_{lat}(\mathbf{r})$ denotes the optical-lattice potential introduced in Sec. 2.13. J is related to the energy width of the lowest band through [168]

$$J = \left(\max(E_q^{(0)}) - \min(E_q^{(0)})\right)/4\ . \tag{6.5}$$

In the limit $V_{lat} \gg E_{rec}$, J can be approximated as [169]

$$J = \frac{4}{\sqrt{\pi}} E_{rec} \left(\frac{V_{lat}}{E_{rec}} \right)^{3/4} \exp\left(-2\sqrt{\frac{V_{lat}}{E_{rec}}} \right) \quad . \tag{6.6}$$

The third term in Eq. (6.3) specifies the on-site interaction energy due to binary collisions: each of the n atoms at one lattice site has $n-1$ other atoms to interact with. The interaction strength is

$$U = \frac{4\pi\hbar^2 a}{m} \int \mathrm{d}^3 r \, |w(\mathbf{r})|^4 \, . \tag{6.7}$$

As before, a denotes the s-wave scattering length. In the limit $V_{lat} \gg E_{rec}$, the Wannier functions can be approximated by a Gaussian with a spatial extent determined by the harmonic oscillator length a_{ho}. In this case, U is given by [169]

$$U = \frac{4\pi\hbar^2 a}{m} k_{lat}^3 \left(\frac{1}{2\pi} \sqrt{\frac{V_{lat}}{E_{rec}}} \right)^{3/2} \quad , \tag{6.8}$$

where $k_{lat} = 2\pi/\lambda_{lat}$ is the modulus of the wavevector of the lattice light.

In Fig. 6.1, the on-site interaction energy U, the tunneling energy J and the ratio U/J are plotted as a function of V_{lat}/E_{rec}. The plots were obtained from a numerical calculation with parameters that match our experimental situation [170]. In addition, approximate results according to Eqs. (6.6) and (6.8) are shown. When increasing the lattice depth, the tunneling barrier height increases and J decreases exponentially. At the same time, U increases slightly due to the increased confinement at the lattice site. Therefore, tuning the lattice beam powers and thereby tuning the lattice depth makes it possible to adjust the ratio U/J over a wide range.

Quantum phase transition U/J determines the ground-state properties of the Bose-Hubbard Hamiltonian. For small U/J, the system shows superfluid transport, whereas for large U/J, transport is suppressed and the system is in the so-called Mott-insulator regime. The two regimes are connected by a phase transition, which occurs for some critical value of the ratio U/J. The transition is a so-called quantum phase transition that occurs at $T = 0$. In contrast, phase transitions in classical systems occur at finite temperatures.

The critical value, at which the quantum phase transition occurs, is given by $(U/J)_{crit} = z \cdot 5.8$, where z is the number of nearest neighbors in the lattice [167, 171–173]. For a cubic lattice with $z = 6$ this results in $(U/J)_{crit} = 34.8$. From Fig. 6.1, the critical lattice depth for the transition to the Mott insulator state in a 3D optical lattice can be read off as $(V_{lat})_{crit} \sim 12 E_{rec}$.

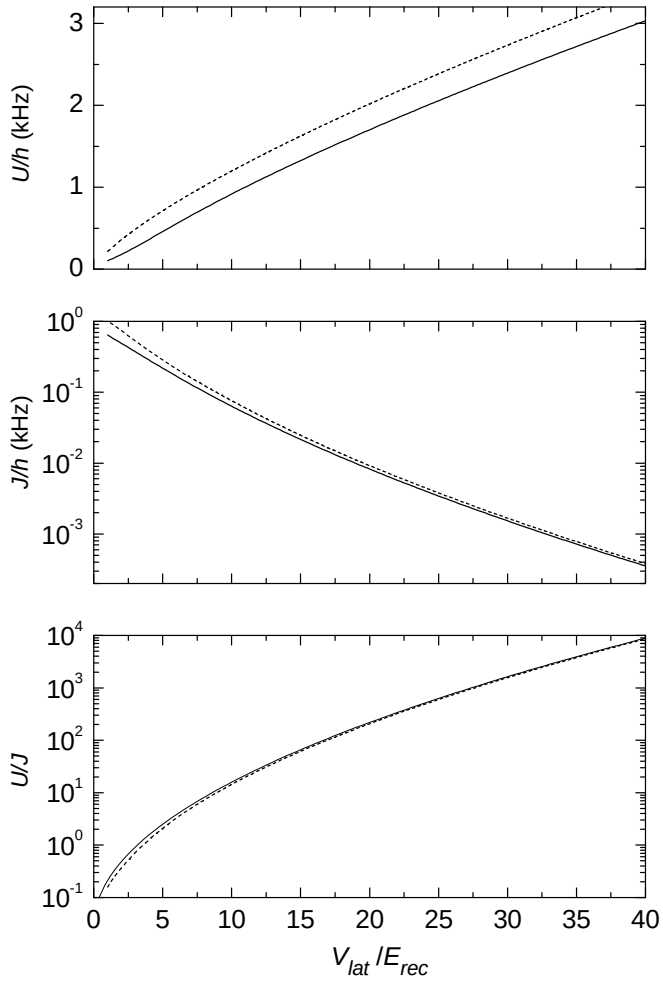

Figure 6.1: Relevant parameters for atoms in an optical lattice. (a) The interaction energy U changes only slightly with increasing lattice depth. (b) Simultaneously, the tunneling parameter J decreases exponentially. (c) As a consequence, the ratio U/J can be adjusted over several orders of magnitude by tuning the lattice depth V_{lat}. The solid lines are the results from numerical calculations [170], while the dashed lines were obtained using the approximate relations Eqs. (6.6) and (6.8).

6.1.2 Superfluid ground state

For $U/J \ll 1$, the tunneling term

$$-J \sum_{<i,j>} \hat{a}_i^\dagger \hat{a}_j \tag{6.9}$$

dominates the Bose-Hubbard Hamiltonian. In order to understand the consequences, it is very instructive to consider a single atom in a double-well potential first. This

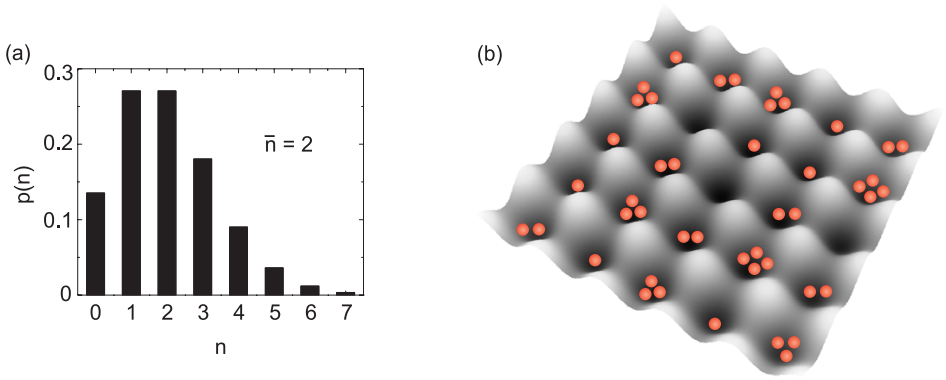

Figure 6.2: Atom-number distribution for the superfluid ground state. (a) At each lattice site, the atom-number distribution follows a Poissonian distribution $p(n)$, which is plotted here for a mean atom number $\bar{n} = 2$. (b) The wave function on each lattice site is a coherent superposition of different atom-number states. Therefore, a snapshot of the atom distribution would yield a random result for each site.

problem is a standard textbook example in quantum mechanics (see e.g. [108]). Here, the tunneling energy E_J is minimized if the atom is delocalized over both wells in a symmetric superposition

$$|\Psi_s\rangle = \frac{1}{\sqrt{2}}\left(\hat{a}_1^\dagger + \hat{a}_2^\dagger\right)|0\rangle \ , \qquad E_J = \langle\Psi_s| - J(\hat{a}_1^\dagger\hat{a}_2 + \hat{a}_2^\dagger\hat{a}_1)|\Psi_s\rangle = -J \ . \tag{6.10}$$

For an atom localized in one potential well, $E_J = 0$, for an antisymmetric superposition $E_J = +J$.

Generalized to an arbitrary number M of potential wells, the atom will tend to delocalize over all wells in order to minimize E_J. In the absence of interactions ($U = 0$), the many-body ground state for N atoms is a product of identical delocalized single-particle states

$$|\Psi_{SF}\rangle = \left(\frac{1}{\sqrt{M}}\sum_{i=1}^{M}\hat{a}_i^\dagger\right)^N |0\rangle \ . \tag{6.11}$$

For each lattice site, the many-body state $|\Psi_{SF}\rangle$ is a superposition of different atom-number (Fock) states. A snapshot of the atom-distribution in the lattice would therefore reveal a random atom number per site with an underlying Poissonian distribution. This is illustrated in Fig. 6.2.

Since it is a product over identical single-particle states, the many-body state Eq. (6.11) can be described by a macroscopic wavefunction. Hence, there is a well-defined phase across the lattice and the system is superfluid.

Momentum distribution An important, experimentally accessible property of an atomic sample is its momentum distribution. The momentum distribution is

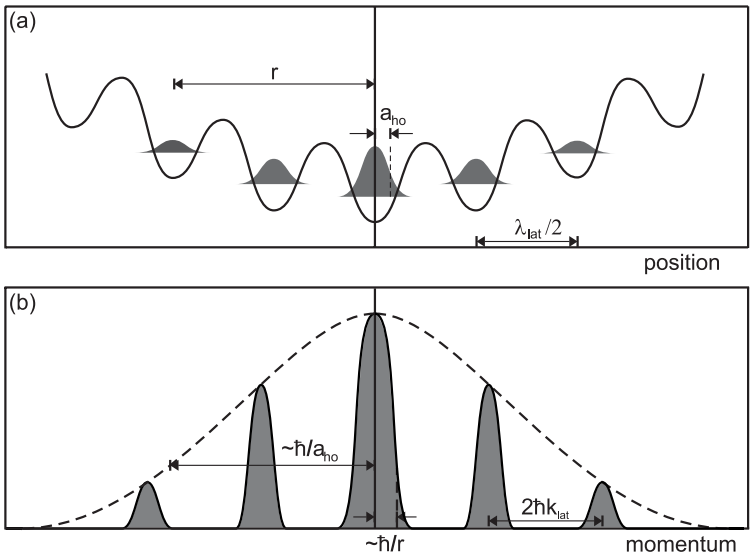

Figure 6.3: (a) Spatial and (b) momentum distribution of a single-particle state in an optical lattice. The periodic lattice potential leads to regularly-spaced satellite peaks in the momentum distribution. The width of the Gaussian envelope of these satellite peaks is determined by the width of the spatial distribution at a single lattice site. The width of the peaks in momentum space is inversely proportional to the overall spatial extent r of the state. The momentum distribution is detected in the experiment by a time-of-flight method.

related to the spatial distribution by a Fourier transform. For atoms in an optical lattice, the position and momentum distribution of a single-particle state are sketched in Fig. 6.3. The periodicity $\lambda_{lat}/2$ of the lattice potential leads to satellite peaks in the momentum distribution separated by $2\hbar k_{lat}$. A simple cubic lattice in position space results in a simple cubic lattice in momentum space. The envelope of the satellite peaks in momentum space is determined by the width of the atom distribution at a single lattice site (see Fig. 6.3). In contrast, the overall spatial extent r of the atom cloud due to an additional external confinement (see Sec. 6.1.4), sets the scale $\sim \hbar/r$ for the width of a peak in momentum space.

As explained in Sec. 2.1.4, the in-trap momentum distribution of the atoms is mapped into a detectable spatial distribution using a time-of-flight method. The atoms are released from the lattice and allowed to expand freely before an absorption image is taken. For many atoms in a lattice, the 3D density distribution $n(\mathbf{x})$ after a time of flight t is described by

$$n(\mathbf{x}) = \left(\frac{m}{\hbar t}\right)^3 |\tilde{w}(\mathbf{k})|^2 \, \mathcal{S}(\mathbf{k}) \quad . \tag{6.12}$$

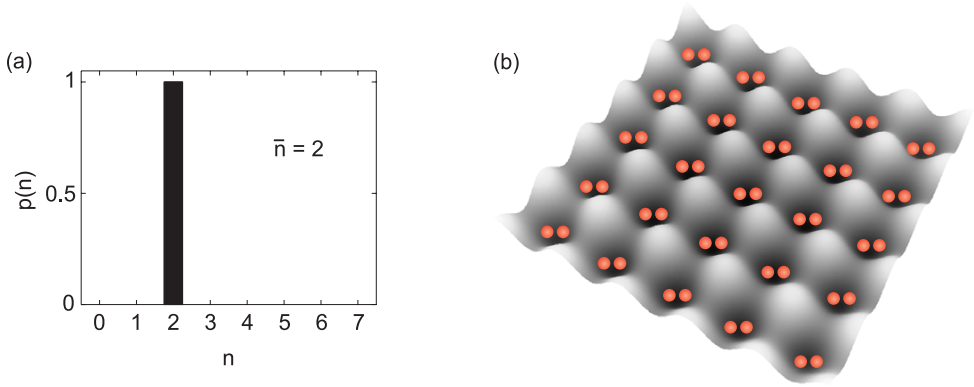

Figure 6.4: Atom-number distribution in the Mott insulator (MI) ground state. (a) The atom-number distribution per site $p(n)$ is discrete in the MI state, shown here for $\bar{n} = 2$. (b) The corresponding spatial distribution with $n = 2$ is shown. It is an ideal starting point to associate Feshbach molecules and thereby create a state with exactly one molecule per site (see Sec. 6.3).

The momentum vector $\mathbf{k}$ is determined by $\hbar\mathbf{k} = m\mathbf{x}/t$. $\tilde{w}$ is the Fourier transform of the single-site Wannier function and the structure factor $\mathcal{S}$ is given by

$$\mathcal{S}(\mathbf{k}) = \sum_{i,j} e^{i\mathbf{k}(\mathbf{r}_i - \mathbf{r}_j)} \langle \hat{a}_i^\dagger \hat{a}_j \rangle \quad . \tag{6.13}$$

The structure factor contains the first-order correlation function $\langle \hat{a}_i^\dagger \hat{a}_j \rangle$, which is a measure for the phase coherence in the system. For the superfluid state Eq. (6.11), the first-order correlation function decreases slowly for increasing spacing $|\mathbf{r}_i - \mathbf{r}_j|$ between lattice sites and approaches a finite value at large distances [9, 10, 169]. This long-range phase coherence results in narrow peaks in the interference pattern.

The formation of narrow interference peaks can also be understood from the observation that the superfluid many-body state of Eq. (6.11) is a product state of identical single-particle states. Therefore, the interference pattern is that of this particular single-particle state. Experimental diffraction patterns are presented in Sec. 6.2.

6.1.3 Mott insulator ground state

In the other limiting case, where $U/J \gg 1$, the interaction term

$$\sum_i \frac{1}{2} U \hat{n}_i \left(\hat{n}_i - 1\right) \tag{6.14}$$

dominates the Bose-Hubbard Hamiltonian. The above expression is minimized when the atom number is the same at each site. This distribution is shown in Fig. 6.4.

Moving an atom to a neighboring lattice site increases the interaction energy by an amount U, which corresponds to the first excited state of the system. Therefore, atom transport in the lattice is suppressed and the excitation spectrum has a gap, which is a signature of an insulator.

The many-body ground state of the Mott-insulating system is a product of local Fock states with n atoms per lattice site

$$|\Psi_{MI}\rangle = \prod_{i=1}^{M} \frac{1}{\sqrt{n!}} (\hat{a}_i^\dagger)^n |0\rangle \ . \tag{6.15}$$

According to the Heisenberg uncertainty principle, a well-defined atom number leads to a maximum phase uncertainty for each lattice site. Hence, there is no macroscopic phase coherence in the system. The atom-atom interactions dominate the behavior of the system and a representation by a macroscopic wave function is not possible. Such a system is called strongly correlated and cannot be treated within the framework of the Gross-Pitaevskii equation [114, 115] or Bogoliubov's theory of weakly interacting bosons [113].

The absence of long-range phase coherence in the MI state implies the absence of diffraction peaks in the corresponding momentum distribution. With the wave-function for the MI state Eq. (6.15), the structure factor Eq. (6.13) reduces to a constant. Hence, we expect the time-of-flight images to show a broad atom distribution without any diffraction peaks.

In a homogeneous system ($\epsilon_i = 0$) with a fixed atom number N and fixed number of lattice sites M, only the fraction of atoms $n \cdot M$ that fit into the commensurate lattice filling with n atoms per site will enter the Mott insulator state. The rest of the atoms will form a superfluid fraction on top of the Mott insulator. This situation is different in the case of an inhomogeneous system, which is treated next.

6.1.4 Inhomogeneous case

In the experiment, the atoms typically experience an external harmonic confinement due to the dipole trap and in addition due to the Gaussian shapes of the lattice beams. In a deep lattice, where $J \ll U$, the atoms will be distributed among the lattice sites such that n_i is the greatest integer that fulfills the inequality

$$\epsilon_i n_i + \frac{1}{2} U n_i (n_i - 1) \leq \mu n_i \ . \tag{6.16}$$

The situation is illustrated in Fig. 6.5. The external confinement leads to a position dependent atom distribution. For $U/J = \infty$, shells of Mott insulator regions with constant n will form. The atom number per site in the shells decreases with increasing ϵ_i.

In the case of $T = 0$ and $J \to 0$, the atom distribution in a 3D lattice with external harmonic confinement can be calculated as follows: The external confinement due to the lattice is modeled by the pseudo-potential of Eq. (2.14). Steps in

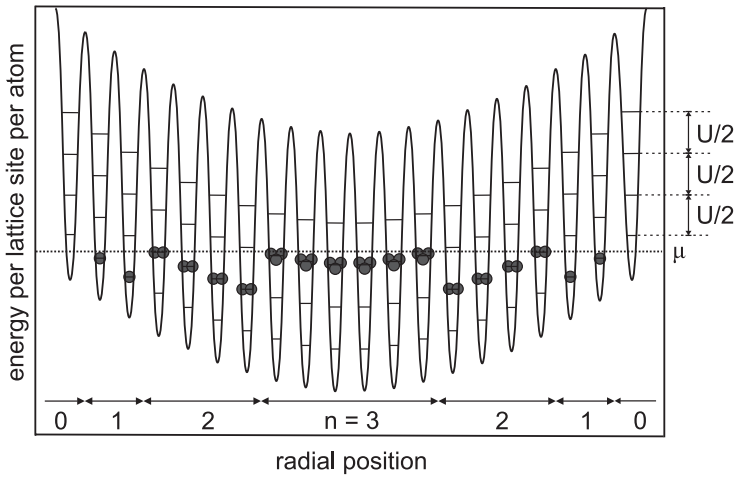

Figure 6.5: Sketch of the lattice filling with external harmonic confinement for $J \to 0$. Note that the energy *per atom* in each lattice site is shown. The energy levels represent different atom numbers n in each lattice site. Atoms fill the lattice sites up to a constant chemical potential μ per atom. In 3D, the system consists of shells of constant atom number per lattice site.

the lattice-filling n occur at radial distances, where $\epsilon_i + U(n-1)/2 = \mu$ for some integer n. Along the coordinate axis j this happens at radii

$$x_{j,n} = \frac{1}{\omega_j}\sqrt{\frac{2}{m}\epsilon_i(n)} = \frac{1}{\omega_j}\sqrt{\frac{2}{m}\left(\mu - \frac{U}{2}(n-1)\right)}\,. \tag{6.17}$$

On the surface of such a shell $\frac{m}{2}\sum_j \omega_j^2 x_j^2$ is constant. Rewritten in scaled variables

$$\tilde{x} = \frac{\omega_j}{\bar{\omega}} x_j \tag{6.18}$$

with $\bar{\omega} = (\omega_x\omega_y\omega_z)^{1/3}$, the shells are spherical. Note that the corresponding volume element is unchanged under this transformation. By rewriting Eq. (6.17) in the scaled variables, setting $r_n = \tilde{x}_{j,n}$, and multiplying by k_{lat}, we obtain

$$k_{lat} r_n = \sqrt{2\frac{U E_{rec}}{\hbar^2\bar{\omega}^2}\left(1 + \frac{2\mu}{U} - n\right)}\,. \tag{6.19}$$

As r_n must be real, there is a maximum value for n:

$$n_{max} = 1 + \lfloor \frac{2\mu}{U} \rfloor\,, \tag{6.20}$$

where $\lfloor x \rfloor$ is the largest integer n with $n \leq x$.

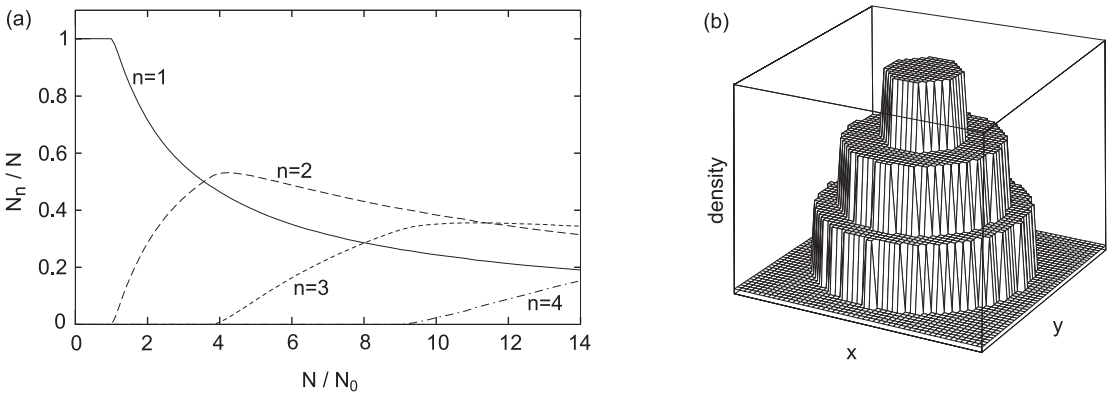

Figure 6.6: Shell structure of the inhomogeneous Mott insulator for $J \to 0$. (a) Fraction of atoms at lattice sites occupied with n atoms each as a function of N/N_0. (b) Corresponding 3D surface plot of the atomic density in a 2D lattice for a maximum atom number per site of $n_{max} = 3$. Inspired by such plots, the shell structure of the Mott insulator is often referred to as a "wedding cake".

Let $S_n = \sum_i \delta_{nn_i}$ be the number of lattice sites occupied with n atoms each. The spacing of the lattice sites is $\lambda_{lat}/2 = \pi/k_{lat}$, so that the average number of lattice sites per volume is $(k_{lat}/\pi)^3$. In the case of many lattice sites per shell, a continuum approximation for S_n can be introduced as

$$S_n = \int_{r_{n+1}}^{r_n} \mathrm{d}r\, 4\pi r^2 \left(\frac{k_{lat}}{\pi}\right)^3 = \frac{4\pi}{3}\left(r_n^3 - r_{n+1}^3\right)\left(\frac{k_{lat}}{\pi}\right)^3 \quad . \tag{6.21}$$

Hence, the total number of atoms is given by

$$N = \sum_{n=1}^{n_{max}} nS_n = \frac{4}{3\pi^2}\sum_{n=1}^{n_{max}} n\left((k_{lat}r_n)^3 - (k_{lat}r_{n+1})^3\right) \quad , \tag{6.22}$$

which can be rewritten as

$$N = N_0 \sum_{n=1}^{n_{max}} \left(1 + \frac{2\mu}{U} - n\right)^{3/2} \tag{6.23}$$

$$N_0 = \frac{8\sqrt{2}}{3\pi^2}\left(\frac{UE_{rec}}{\hbar^2\bar{\omega}^2}\right)^{3/2} \quad . \tag{6.24}$$

N_0 is a normalization factor. In the experiment, μ is not known, but N/N_0 is. μ can then be determined from Eq. (6.23) by inversion. The interaction energy U is calculated according to Eq. (6.8).

The number of atoms at sites with n atoms each is

$$\frac{N_n}{N} = \frac{nS_n}{N} = n\frac{\left(1+\frac{2\mu}{U}-n\right)^{3/2} - \left(\frac{2\mu}{U}-n\right)^{3/2}}{\sum_{m=1}^{n_{max}}\left(1+\frac{2\mu}{U}-m\right)^{3/2}} \ . \tag{6.25}$$

The result is plotted in Fig. 6.6 (a) as a function of N/N_0. Note, that the maximum value for N_2/N is 53%. This value is reached at the point where n_{max} is just above three.

The atomic density distribution in an optical lattice is sometimes illustrated as a 3D surface plot for a two-dimensional cut through the 3D lattice structure. For the case of a Mott insulator in the limit $J \to 0$, i.e. $U/J \to \infty$, such a plot is shown in Fig. 6.6 (b). For obvious reasons, the distribution shown is often referred to as "wedding cake" distribution. Recently, two groups independently resolved the spatial shell structure of the inhomogeneous Mott insulator in their experiments [174, 175].

Finite U/J Up to now, the inhomogeneous case was discussed for $U/J = \infty$ and $T = 0$. There, the atoms arrange in shells of constant n. For finite U/J, these Mott insulator shells are separated by shells of atoms in the superfluid state, and the sharp steps in the atom density distribution soften. Around the steps, a gain in tunneling energy makes energy levels in neighboring sites accessible that would lie above μ in the case of $U/J = \infty$. In these regions, the superfluid state is energetically more favorable than the Mott insulator state. For "wedding cake" illustrations in the case of finite U/J see Ref. [97].

6.2 Quantum phase transition near 1007 G

Here we report the experimental realization of the quantum phase transition from a superfluid to a Mott insulator state for ^{87}Rb atoms in an optical lattice. Similar results were previously reported in Refs. [97, 103]. The novelty of our experiment lies in the fact that we produce the atomic Mott insulator at high magnetic fields close to the Feshbach resonance at 1007.4 G. This is a prerequisite for creating a state with one molecule per lattice site as described in Sec. 6.3.

6.2.1 Experimental sequence

The experimental sequence for creating an atomic Mott insulator near 1007.4 G is as follows: First, a BEC is created in the magnetic trap, and then transferred to the dipole trap. Next, the magnetic field is switched on and set to a value of ~ 1006 G. The magnetic field produces a slight gradient which leads to a shift in the position of the trap minimum and pulls some atoms out of the dipole trap. Therefore, we allow the system to reach equilibrium again within a few hundred ms. After that wait time, the dipole trap contains an almost pure BEC with about 10^5 atoms and no

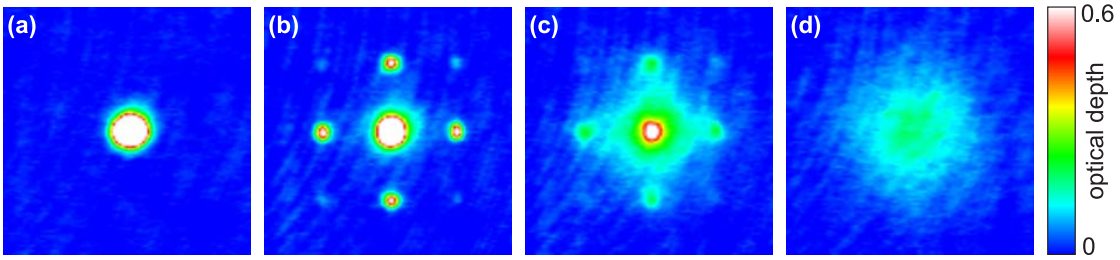

Figure 6.7: Transition from the superfluid to the Mott insulator state at 1006 G. In the experiment, the lattice depth is ramped up slowly to a final value and then switched off abruptly. After a certain time-of-flight, an absorption image is taken. Such images are shown in parts (a)-(d) for lattice depths of $V_{lat} = 0, 5, 12,$ and $24E_{rec}$. For low lattice depths, the system is in the superfluid state. Diffraction peaks are clearly visible around the central cloud. As the lattice depth is increased the contrast of the pattern gradually decreases. It smears out almost completely around $V_{lat} \sim 12E_{rec}$, which marks the onset of the Mott insulator regime. Deep in the Mott insulator regime, a broad structure-less atom cloud is found.

discernable thermal fraction. Subsequently, the power of the lattice light is ramped up to a value corresponding to the desired lattice depth V_{lat}.

The functional form of the lattice-light ramp was adapted from Ref. [97]. We use an exponential ramp with a duration of 80 ms and a time constant $\tau = 20$ ms. After a typical holdtime in the lattice of 20 ms, the atom distribution is analyzed by time-of-flight absorption imaging. To this end, the magnetic field, the lattice potential and the dipole-trap light are switched off simultaneously and the cloud is allowed to expand freely for $t_{exp} = 12$ ms before an image is taken.

We repeated the above sequence for different final lattice depths V_{lat}. Absorption images of this measurement are shown in Fig. 6.7. For low lattice depths diffraction peaks are clearly visible around the central cloud. When the lattice depth is increased further, the strength of the diffraction peaks gradually decreases and the central peak broadens. Around $V_{lat} \sim 12E_{rec}$ the interference pattern smears out almost completely and for even deeper lattice potentials, only a broad atom cloud without any structure is visible.

The vanishing of the interference pattern around the critical lattice depth of $V_{lat} \sim 12E_{rec}$ marks the quantum phase transition to the Mott insulator state. The diffraction pattern thereby vanishes due to the vanishing phase coherence between the lattice sites in the Mott phase (see Sec. 6.1.3). In contrast, the sharp diffraction peaks for low lattice depths are a signature of the long-range phase coherence in the superfluid phase (see Sec. 6.1.2).

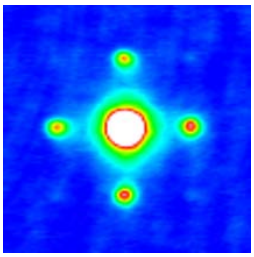

Figure 6.8: Restored phase coherence. After holding the atoms deep in the Mott insulator regime at $V_{lat} = 24E_{rec}$ for 20 ms, the lattice depth is ramped down linearly to $4E_{rec}$ within 10 ms, before switching off the lattice. The diffraction peaks reappear, indicating the transition back to the superfluid state.

6.2.2 Restoring phase coherence

The loss of diffraction peaks in the Mott phase could have several origins. In principle, technical noise could lead to irreversible processes, such as heating or dephasing. This can be tested by melting the Mott insulator, i.e. by ramping the lattice depth back down to well below the transition point. If the quantum phase transition is reversible, the diffraction pattern will reappear. We performed such a measurement for the parameters of Fig. 6.7. First, the lattice depth was ramped up to $V_{lat} = 24E_{rec}$ and held there for 20 ms. Next, the lattice depth was ramped back down linearly to $V_{lat} = 4E_{rec}$ within 10 ms, before switching the lattice off abruptly. As expected, the diffraction pattern reappears, as can be seen in Fig. 6.8. This proves that the vanishing of the diffraction peaks in Fig. 6.7 is caused by the transition to the Mott insulator state, not by heating or dephasing. The restoration of phase coherence will be the main experimental signature when creating a Mott-like state of molecules (see Sec. 6.3).

A quantity of interest is the timescale on which phase coherence in the lattice is restored. Since phase coherence is restored by atoms tunneling between lattice sites, the tunneling time is expected to play a role. In order to test this, the duration of the back-ramp was varied in the experiment. The width of the central peak in the time-of-flight images served as a measure for the phase coherence [97].

The results are plotted in Fig. 6.9. The parameters of this measurement are similar to those of Fig. 6.8, except that the final lattice depth is now $V_{lat} = 4.8E_{rec}$. The lattice ramp-down time was varied from 0 to 10 ms. An exponential fit to the data yields a time constant of $\tau \sim 0.8$ ms, which coincides with the tunneling time at the final lattice depth of $V_{lat} = 4.8E_{rec}$ (see Fig. 6.1). Phase coherence is almost completely restored in ~ 2 ms. Longer ramp times do not change the width significantly. Hence, it only takes a few tunneling events for restoring a macroscopic phase across the lattice (see also Ref. [97]).

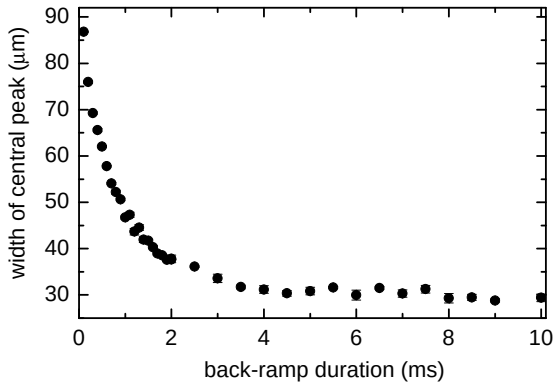

Figure 6.9: Timescale for restoring phase coherence. The width of the central peak of the time-of-flight images gives a measure for the phase coherence. Phase coherence is restored in ~ 2 ms.

6.3 A Mott-like state of molecules

This section reports the creation of a quantum state with exactly one molecule per lattice site. In principle, such a state could be created by inducing a quantum phase transition from a molecular superfluid to a molecular Mott insulator. This is feasible, if the molecule-molecule interactions are predominantly elastic and repulsive. However, many molecular species, and in particular the Feshbach molecules made from bosonic atoms, do not have such convenient interaction properties. Hence, alternative strategies are needed. This section demonstrates a technique that does not rely on the molecule-molecule interaction properties. Instead, we associate the molecules from an atomic Mott insulator with a core of doubly occupied lattice sites. Several previous experiments associated molecules in optical lattices [74, 75, 176–178], but none of them demonstrated the production of a quantum state with one molecule per lattice site.

6.3.1 External confinement

For creating molecules in the optical lattice, we want to start with a Mott insulator that has a maximum fraction of atoms on doubly occupied sites. Lattice sites with more than two atoms are undesirable, because any Feshbach molecule created on a lattice site with $n \geq 3$ is bound to collide inelastically with the other particles (atoms or molecules) on that lattice site. This leads to fast loss of the molecule and its collision partner.

Fig. 6.6a predicts a maximum fraction of doubly occupied sites for an overall atom number $N \sim 4\,N_0$. According to Eq. (6.24), N_0 depends on the overall external confinement due to the dipole trap and the lattice beams. For the dipole-trap

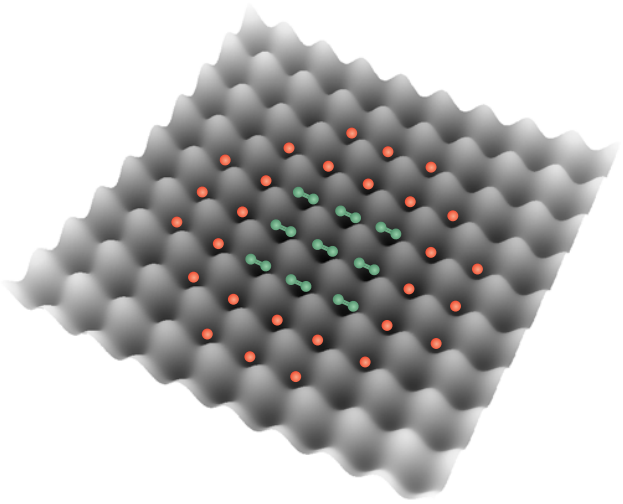

Figure 6.10: Scheme of the Mott-like state of molecules. In the core of the cloud, each lattice site is occupied by exactly one molecule (shown in green). In the surrounding shell, each site is occupied by exactly one atom (shown in red). The atoms can be removed with a blast laser.

setup used in previous experiments and typical lattice parameters, we estimate N_0 to be around $5 - 6 \times 10^3$. Experimentally, such low atom numbers have several disadvantages. We find that creating pure condensates with $\sim 2-3\times10^4$ is difficult. Moreover, such low atoms numbers (and even lower molecule numbers) are harder to detect reliably.

As a consequence, we redesigned our dipole trap in order to reduce the external confinement. Now the trap light is provided by two different lasers. The additional laser is a multi-frequency fiber laser with a central wavelength of 1050 nm and a linewidth of ~ 1 nm. The corresponding beam has an elliptically shaped focus with waists of 60 μm and 700 μm. The strong confinement in one direction holds the atoms against gravity. Typically, we work at a power of 2.1 W, resulting in an angular trap frequency of $2\pi \times 110$ Hz along gravity. In the other two directions, the fiber laser does not provide enough confinement. Here, we use the single-frequency Nd:YAG laser from previous experiments. The two different laser beams intersect at right angles to form a crossed dipole trap. The Nd:YAG-laser beam has a spherically symmetric focus with a waist of 140 μm. At a power of 170 mW, the measured trap frequency is $2\pi \times 20$ Hz. Thus, the mean trap frequency is now reduced to $\bar{\omega}_{dip} = 2\pi \times 35$ Hz and N_0 increases significantly. For $V_{lat} = 24E_{rec}$ and $a \sim 1.14a_{bg}$ (corresponding to $B \sim 1006$ G), N_0 is close to $\sim 2.5 \times 10^4$.

6.3.2 Molecules in the optical lattice

The experimental sequence for creating a Mott-like state of molecules starts with the creation of an atomic Mott insulator at 1006 G as described in Sec. 6.2.1. To that end, about 10^5 atoms are loaded into the optical lattice and the lattice depth is ramped up to $V_{lat} = 24E_{rec}$. At this lattice depth, the atomic tunneling amplitude is $J = 2\pi\hbar \times 4$ Hz (see Fig. 6.1).

The experiment shows that the dipole-trap light from the fiber laser at 1050 nm causes fast loss of the Feshbach molecules, presumably due to photodissociation. Before associating molecules, we therefore reduce the power of the dipole-trap light slowly to zero. Once the trap light is off, we jump the magnetic field to a value of 1008.8 G. About 2 ms later, the magnetic field is slowly (at 2 G/ms) ramped down across the Feshbach resonance at 1007.4 G to a final value of $B = 1006.6$ G.

At lattice sites with a filling of $n = 1$, the magnetic-field ramp has no effect. At sites with $n > 1$, atom pairs are associated to molecules. As explained before, molecules formed on sites with $n > 2$ can collide inelastically with other atoms or molecules at the same lattice site, leading to fast loss of the molecule and its collision partner. The association ramp lasts long enough to essentially empty all sites with $n > 2$ atoms. Typically, we lose about 10% of the overall atom number during the association ramp. This might be due to the fact that we work close to the point where the $n = 3$ core starts to form. On the other hand, the lost atoms might also come from the superfluid regions in between the Mott insulator shells.

For lattice sites with $n = 2$ atoms, the association efficiency is well above 80%, as predicted by the Landau-Zener formula Eq. (4.9). The maximum fraction of atoms that is converted into molecules (measured as the atom number reappearing after dissociation) is found to be 47(3)%, which is close to the theoretical limit of 53% discussed in Sec. 6.1.4. The resulting Mott-like state of molecules with one molecule per site is sketched in Fig. 6.10.

The mobility of atoms and molecules in the lattice differ significantly. The molecular tunneling amplitude is obtained as follows: The polarizability of a Feshbach molecule is approximately twice as large as that for one atom. Hence, the molecules experience a lattice depth of $2V_{lat}$. Moreover, the molecules have twice the mass of a single atom and therefore their recoil energy is half the atomic recoil energy. At a lattice depth of $V_{lat} = 24E_{rec}$ for atoms, the tunneling amplitude for molecules is calculated to be $J_m = 2\pi\hbar \times 0.3$ mHz. This is negligible compared to the holdtime between molecule association and dissociation. Hence, the positions of the molecules are effectively frozen.

In order to show that the molecular part of the sample actually is in a Mott-like state, the molecules are first dissociated back into atom pairs by slowly (at 1.5 G/ms) ramping the magnetic field back across the Feshbach resonance. This brings the system back into the atomic Mott insulator state with shells with $n = 1$ and $n = 2$. Next, the atomic Mott insulator is melted by slowly (within 10 ms) ramping down the lattice from $V_{lat} = 24E_{rec}$ to $V_{lat} = 4E_{rec}$. Finally, the optical

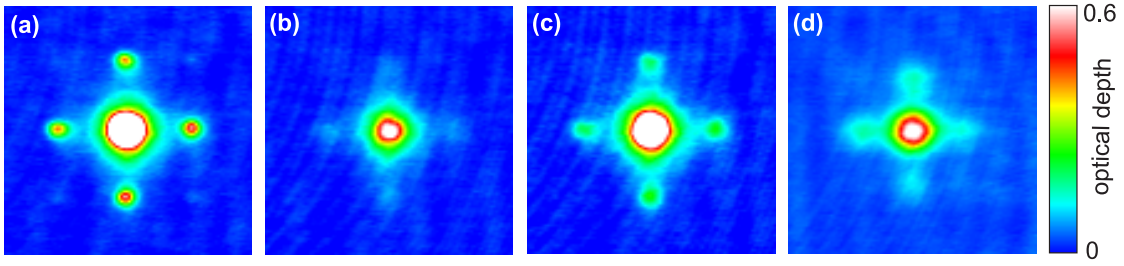

Figure 6.11: Atomic Mott-insulator and Mott-like state of molecules. (a) An atomic Mott insulator is melted by reducing the lattice depth slowly. The system returns to the superfluid phase and phase coherence is restored. This phase coherence is probed by quickly switching off the lattice and observing an atomic interference pattern in time of flight. (b) After association of molecules, only lattice sites occupied by $n = 1$ atoms contribute to the signal after lattice-ramp down. (c) After association and dissociation of molecules, the satellite peaks of the melted system are much stronger than in (b), thus proving that the molecular part of the cloud is in a Mott-like state with $n = 1$. (d) Pure molecular $n = 1$ state. Same as (c) but between association and dissociation, remaining atoms were removed with blast light. For the pictures in (a)-(d), visibilities of 0.93(2), 0.80(5), 0.86(1), and 0.61(2) are obtained, calculated from squares with areas corresponding to atomic momenta of $0.22\hbar k \times 0.22\hbar k$ (see Sec. 6.3.4).

lattice is quickly switched off (together with the dipole trap and the magnetic field), and after some time of flight an absorption image is taken.

Results are shown in Fig. 6.11. Part (a) is identical to Fig. 6.8. No association (or dissociation) ramp was applied. The fact that phase coherence is restored demonstrates that an atomic Mott insulator is realized at 1008.8 G. Part (b) shows the pattern obtained if molecules are associated but not dissociated, so that they remain invisible in the detection. Hence, the signal comes only from sites with a single atom. Part (c) was obtained for the full sequence with association and dissociation of molecules. Obviously, the satellite peaks regain considerable population compared to (b), which proves that after dissociation, an atomic Mott insulator is recovered. Hence, the molecule association and dissociation must have been coherent and adiabatic. Combined with the freezing of the molecular positions and the fact that the association starts from an atomic Mott insulator with a core of doubly occupied lattice sites, this implies that the molecular part of the cloud must have been in a quantum state with one molecule per lattice site.

6.3.3 Pure molecular system

The Mott-like state of molecules sketched in Fig. 6.10 is a mixed system consisting of the molecular $n = 1$ core surrounded by the atomic $n = 1$ shell. The remaining

atoms can be removed from the lattice using a blast technique [56, 74]. We adapted the scheme from Ref. [74] to produce a pure molecular sample. A microwave field and a light field are applied simultaneously for a few ms, immediately after associating the molecules. The microwave field has a frequency of 9126 MHz and drives the transition between levels that are adiabatically connected to $|f, m_f\rangle = |1, +1\rangle$ and $|2, +2\rangle$ at small magnetic field. Due to the small linewidth, the microwave selectively addresses only the atoms and not the molecules. The light pulse is resonant with the closed cycling transition $|2, +2\rangle \leftrightarrow |3, +3\rangle$. At $B \sim 1006$ G, the corresponding transition frequency is ~ 1400 MHz blue detuned from the value at zero magnetic field. Atoms that absorb a microwave photon are subsequently blasted out of the lattice by the light. We find that the molecule numbers before and after the blast are identical within the experimental uncertainty of 5%.

In order to show that the pure molecular sample is in a Mott-like state, the molecules are dissociated, the lattice is ramped down to $V_{lat} = 1.2E_{rec}$ within 30 ms, ramped back up to $V_{lat} = 6E_{rec}$ within 5 ms, and finally switched off. The result is shown in Fig. 6.11(d). Again, an interference pattern is visible. The interference peaks are not as pronounced as in part (c). This might be due to the fact that the state after blasting away the atoms and dissociating the molecules into atom pairs is not the ground state of the system. The additional energy presumably shows up as an increase in temperature when ramping down the lattice.

The special ramp scheme for restoring phase coherence in the case of the purified system is needed due to the following reason. Consider the state consisting only of the $n = 2$ Mott insulator core. If one of the atoms at a doubly occupied site tunneled to an empty neighboring lattice site, an energy U would be released. But there is no reservoir that could absorb this energy so that the tunneling is suppressed, as observed in a recent experiment [177]. In order to restore phase coherence when melting the pure $n = 2$ Mott insulator core, the atoms must tunnel to neighboring lattice sites. Therefore, a strong reduction of U is required. This can be achieved by ramping the lattice down to a point much below $V_{lat} = 4E_{rec}$ (or by reducing the scattering length). But at such a low lattice depth, the sudden switch-off of the lattice does not produce noticeable satellite peaks. To observe such peaks, the lattice therefore must be ramped back up before switching it off.

6.3.4 Visibility

The height of the satellite peaks can be quantified using the visibility

$$\mathcal{V} = \frac{n_{max} - n_{min}}{n_{max} + n_{min}} \quad . \tag{6.26}$$

As in Ref. [179], we measure the maximum density n_{max} at the first lateral peak of the time-of-flight interference pattern. The minimum density n_{min} is determined under 45° off at the same distance from the central peak. For spherically symmetric Wannier functions, the visibility only depends on the structure factor Eq. (6.13).

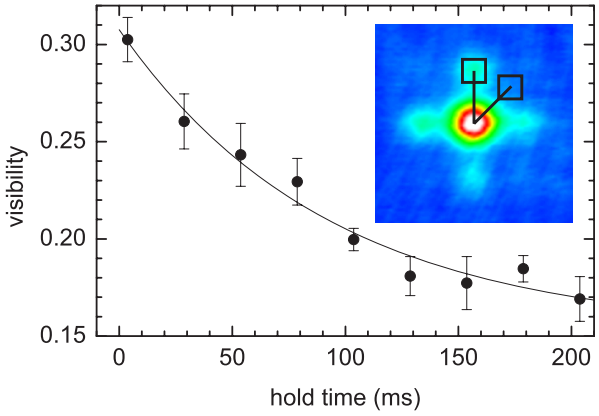

Figure 6.12: Lifetime of the pure Mott-like state of molecules. The visibility of the satellite peaks in measurements similar to Fig. 6.11 (d) decays as a function of the hold time between molecule association and dissociation. The visibility was calculated from squares (as shown in the inset) with areas corresponding to atomic momenta of $1.0\hbar k \times 1.0\hbar k$. The line shows an exponential fit which yields a $1/e$-lifetime of 93(22) ms.

This can be seen by inserting expression Eq. (6.12) into the above definition of the visibility. We average n_{max} and n_{min} over a square as illustrated in the inset of Fig. 6.12. In order to compensate for asymmetries due to technical noise, we take all four pairs of maxima and minima for the data analysis .

Figure 6.12 shows the decay of the visibility as a function of the hold time between molecule association and dissociation. These data were obtained from measurements as in Fig. 6.11(d), except that after dissociation the lattice was ramped down to $V_{lat} = 2.8E_{rec}$ within 10 ms and ramped back up to $V_{lat} = 5.5E_{rec}$ within 4 ms. The observed lifetime of the visibility is sufficient for many applications. For comparison, the measured lifetime of the molecule number is 160(20) ms, similar to Ref. [74]. This sets an upper limit on the lifetime of the visibility, because the sites at which molecules are lost are randomly distributed across the lattice, thus gradually destroying the Mott-like state. The fact that the visibility does not settle to zero might be partly due to the fact that the Wannier function for small lattice depth is not spherically symmetric. Hence, the Fourier transform of the Wannier function does not cancel in the above definition of the visibility, as would be the case otherwise (see expression Eq. (6.12)). The non-zero visibility at long times might also be partly due to non-removed atoms because of imperfections of the blast laser (15% of the total signal at zero hold time).

6.3.5 Excitation spectrum

An interesting property of a Mott insulator state is a gap in the excitation spectrum which is due to the interaction between particles. Here we probe the excitation

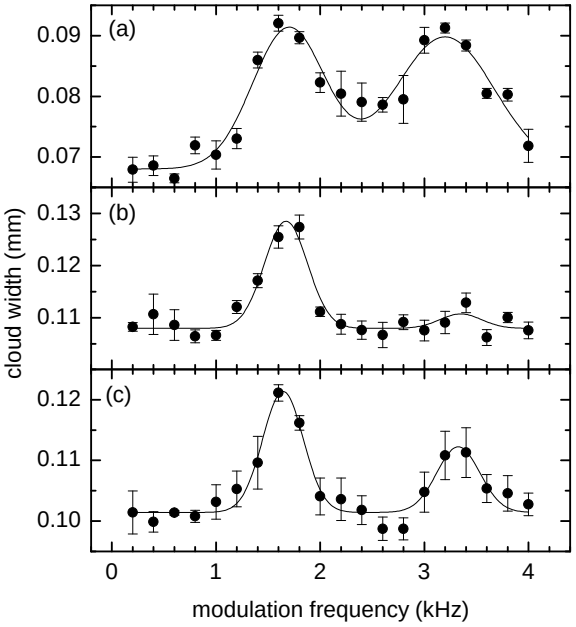

Figure 6.13: Atomic excitation spectrum. The full width at half maximum of the central interference peak is shown as a function of the frequency at which the lattice depth is modulated. The results in parts (a)-(c) correspond to the conditions of Fig. 6.11 (a)-(c). First, the usual lattice ramp-down is interrupted at $V_{lat} = 15E_{rec}$. Next, the power of one lattice beam is modulated for 11 ms with a peak-to-peak amplitude of 50%. Finally, the lattice ramp-down continues as usual. Resonances are visible at 1.6 and 3.2 kHz. The lines are a guide to the eye.

spectrum by amplitude modulation of one of the lattice beams [180]. The modulation with frequency ν_{mod} creates sidebands on the lattice light. Therefore, an atom can absorb a lattice photon at the carrier frequency and emit it into the red sideband, which adds energy to the system. For an $n = 1$ Mott insulator, this will only happen if $h\nu_{mod} \sim U$. In this case, an atom can tunnel to an already occupied neighboring lattice site. The extra energy shows up in a broadening of the interference peaks, when the lattice light is ramped back down into the superfluid regime. An alternative strategy to the modulation method is the application of a magnetic-field gradient [97, 103].

Figure 6.13 shows excitation spectra of the atomic system at a lattice depth of $V_{lat} = 15E_{rec}$. In Fig. 6.13(a), the spectrum was recorded before the association of molecules (corresponding to the situation in Fig. 6.11(a)). Clear resonances at energies U and $2U$ are visible, which is an additional proof that the system initially is an atomic Mott insulator. Figure 6.13(b) shows a spectrum after molecule association. Here, the signal at $2U$ has essentially disappeared, because the signal at $2U$ is

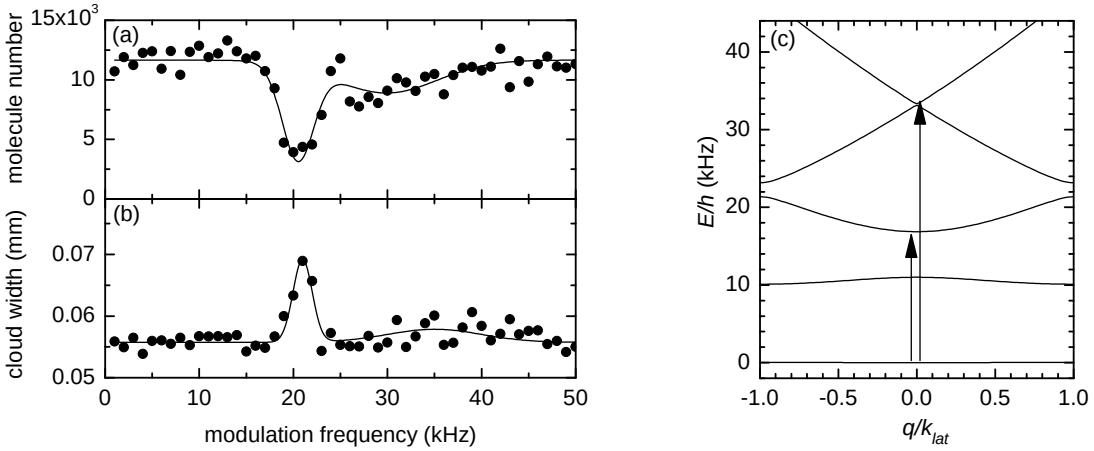

Figure 6.14: Excitation spectrum of the pure Mott-like state of molecules. Parameters are chosen similar to Fig. 6.11(d). The lattice is ramped down from $V_{lat} = 24E_{rec}$ to $V_{lat} = 3.6E_{rec}$ within 20 ms. Next, the power of one lattice beam is modulated for 10 ms with a peak-to-peak amplitude of 20%. Then the lattice is switched off. Parts (a) and (b) show a narrow resonance at 21 kHz and a broad resonance around 33 kHz. The lines are a guide to the eye. These resonances are not related to the molecular on-site interaction matrix element U_m. Instead, both resonances can be explained as band excitation, when considering the one-dimensional band structure for molecules at this lattice depth, which is shown in part (c). The zero of energy in (c) is chosen at the bottom of the lowest band. Arrows indicate the band excitations.

created by processes that require lattice sites with $n \geq 2$ atoms [97]. But these are absent after the molecule-association ramp. After dissociating the molecules back into atom pairs, the peak at $2U$ reappears (Fig. 6.13(c)). The spectrum is similar to the first one Fig. 6.13(a), except for some heating. However, the resonances at U and $2U$ are clearly visible in Fig. 6.13(c). This supports the previous conclusion that the system after the association-dissociation ramp is again an atomic Mott insulator.

We also measured excitation spectra at various lattice depths for the Mott-like state of molecules after removing the atoms, corresponding to Fig. 6.11(d). These spectra show no resonances related to the molecular on-site interaction matrix element U_m. An example is shown in Fig. 6.14. The lattice depth chosen here is a factor of approximately 4 lower than in Fig. 6.14. Hence, the tunneling amplitude for the molecules $J_m = 2\pi\hbar \times 12$ Hz in Fig. 6.14 is comparable to the tunneling amplitude for atoms $J = 2\pi\hbar \times 21$ Hz in Fig. 6.13. The search for resonances related to U_m is hampered by the fact that the value of U_m is unknown. Furthermore, from the measured rate-coefficient for inelastic molecule-molecule collisions [61], we estimate a lifetime of 16 μs for two molecules at one lattice site at a lattice depth of $V_{lat} = 15E_{rec}$. This leads to an estimated resonance width of $\Gamma = 2\pi\hbar \times 10$ kHz.

A possible resonance would therefore be too broad and consequently too shallow to be observed.

We took data in a broad parameter range, but could not find any resonances related to U_m. We only observed band-excitation resonances, as in Fig. 6.14. Both resonances in Fig. 6.14 can be explained as band excitation. We took data in deeper lattices. Here, the broad resonance splits into two narrower resonances, which both follow the energy of a band excitation as a function of lattice depth. The molecule loss at the band-excitation resonance is caused by the fact that the tunneling amplitude in higher bands is much higher than in the lowest band. Hence, a molecule in a higher band can easily tunnel to a neighboring site. If this site was already occupied by another molecule, then an inelastic collision will lead to fast loss.

The data in Fig. 6.14 do not show any signature of the first band-excitation resonance at 11 kHz. This is because of the parity of the states involved. To illustrated this, we consider the states with quasi-momentum $q = 0$. These states have even/odd parity for even/odd band number. Therefore transitions between even and odd bands are suppressed.

In the experiment, the molecule decay rate Γ is much larger than the tunneling matrix element J_m, so that the effective tunneling rate between neighboring lattice sites is $4J_m^2/(\hbar\Gamma)$ [149]. Hence we expect fast on-site decay Γ to suppress the mobility in the many-body system. This might result in an insulator-like behavior without a gap.

Chapter 7

Outlook

The association of ultracold molecules with Feshbach resonances was a real breakthrough in the field of ultracold quantum gases (see Chap. 1). Many groups performed experiments based on this technique. Our group pioneered the work on Feshbach molecules in ^{87}Rb. The experiments described in this thesis reveal many interesting aspects of Feshbach molecules and serve as a good starting point for future investigations.

The preparation of a Mott-like state of molecules in Chap. 6 prompts the question what the transport properties of the system are. As discussed in Sec. 6.3.5, the inelastic interaction properties of the molecules should suppress transport in the many-body system, somewhat analogous to the suppression of tunneling by elastic interactions in the atomic Mott insulator. Experimental studies of this effect are presently under way in our laboratory.

The Mott-like state of molecules offers another very interesting prospect. Raman transitions induced with laser light could drive the molecules to the internal ground state. Next, the optical lattice could be ramped down and a BEC of molecules in the internal ground-state might be formed [181]. Currently, several groups worldwide working with Feshbach molecules aim for the realization of this scheme.

The Feshbach-association technique was recently extended to heteronuclear molecules [182, 183]. If transferred to the internal ground state, they can have a large permanent electric dipole moment. A quantum degenerate gas of these polar molecules is expected to show new behavior due to the long-range nature of the dipole-dipole interaction (see e.g. Refs. [45, 46]). Polar molecules in optical lattices are promising candidates for quantum simulations and quantum information schemes [160–164]. While heteronuclear ground-state molecules have already been produced from laser-cooled atomic samples [184, 185], the production of a quantum degenerate gas of polar molecules is a challenging goal. Polar molecules and their applications are likely to be one of the hot topics for many years to come.

Binary collisions and the association of dimers are well understood by now. In contrast, the complexity of collisions involving more than two particles makes a theoretical description considerably more difficult. The study of magnetic-field

dependent three-atom, atom-dimer, and dimer-dimer collisions might lead to new insights. An intriguing effect is the occurrence of a three-body bound state in a system of three interacting particles. Evidence for this long-standing prediction by Efimov was reported in a recent experiment on three-body loss resonances in cesium [186]. The same group also observed dimer-dimer loss resonances [60]. In both cases, the loss resonances are presumably caused by a bound state crossing the corresponding threshold. Hence, like in the case of dimer association, a slow magnetic-field ramp might create trimers or even tetramers. In analogy to the situation described in Chap. 6, an optical lattice might help to control the initial parameters and to suppress inelastic decay of the trimers/tetramers [187]. The study of molecules with more than two atoms is an interesting topic. Physical insight gained here might be relevant for other fields such as nuclear physics or cluster physics.

Bibliography

[1] M. H. Anderson, J. R. Ensher, M. R. Matthews, C. E. Wieman, and E. A. Cornell. Observation of Bose-Einstein condensation in a dilute atomic vapor. *Science*, 269:198, 1995.

[2] C. C. Bradley, C. A. Sackett, J. J. Tollett, and R. G. Hulet. Evidence of Bose-Einstein condensation in an atomic gas with attractive interactions. *Phys. Rev. Lett.*, 75:1687, 1995. Erratum: *Phys. Rev. Lett.* 79:1170, 1997.

[3] K. B. Davis, M.-O. Mewes, M. R. Andrews, N. J. van Druten, D. S. Durfee, D. M. Kurn, and W. Ketterle. Bose-Einstein condensation in a gas of sodium atoms. *Phys. Rev. Lett.*, 75:3969, 1995.

[4] A. Einstein. Quantentheorie des idealen einatomigen Gases. *Sitzber. Kgl. Preuss. Akad. Wiss*, 1925:3, 1925.

[5] A. Einstein. Quantentheorie des idealen einatomigen Gases. *Sitzber. Kgl. Preuss. Akad. Wiss*, 1924:261, 1924.

[6] A. Griffin. A brief history of our understanding of BEC: From Bose to Beliaev. In M. Inguscio, S. Stringari, and C. E. Wieman, editors, *Proceedings of the international school of physics, "Enrico Fermi", Course CXL: Bose-Einstein condensation in atomic gases*, pages 1–10. IOS Press, Amsterdam, 1998.

[7] J. F. Annett. *Superconductivity, superfluids and condensates*. Oxford, 2004.

[8] UltraCold Atom News. https://ucan.physics.utoronto.ca.

[9] C. J. Pethick and H. Smith. *Bose-Einstein condensation in dilute gases*. Cambridge University Press, Cambridge, 2002.

[10] L. Pitaevskii and S. Stringari. *Bose-Einstein condensation*. Clarendon Press, Oxford, 2003.

[11] O. Morsch and M. Oberthaler. Dynamics of Bose-Einstein condensates in optical lattices. *Rev. Mod. Phys.*, 78:179, 2006.

[12] I. Bloch. Ultracold quantum gases in optical lattices. *Nature Physics*, 1:23, 2005.

[13] B. DeMarco and D. S. Jin. Onset of Fermi degeneracy in a trapped atomic gas. *Science*, 285:1703, 1999.

[14] H. Feshbach. Unified theory of nuclear reactions. *Ann. Phys.*, 5:357, 1958.

[15] H. Feshbach. A unified theory of nuclear reactions 2. *Ann. Phys.*, 19:287, 1962.

[16] W. C. Stwalley. Stability of spin-aligned hydrogen at low temperatures and high magnetic fields: new field-dependent scattering resonances and predissociations. *Phys. Rev. Lett.*, 37:1628, 1976.

[17] E. Tiesinga, A. J. Moerdijk, B. J. Verhaar, and H. T. C. Stoof. Conditions for Bose-Einstein condensation in magnetically trapped atomic cesium. *Phys. Rev. A*, 46:1167, 1992.

[18] E. Tiesinga, B. J. Verhaar, and H. T. C. Stoof. Threshold and resonance phenomena in ultracold ground-state collisions. *Phys. Rev. A*, 47:4114, 1993.

[19] S. Inouye, M. R. Andrews, J. Stenger, H.-J. Miesner, D. M. Stamper-Kurn, and W. Ketterle. Observation of Feshbach resonances in a Bose-Einstein condensate. *Nature*, 392:151, 1998.

[20] P. Courteille, R. S. Freeland, D. J. Heinzen, F. A. van Abeelen, and B. J. Verhaar. Observation of a Feshbach resonance in cold atom scattering. *Phys. Rev. Lett.*, 81:69, 1998.

[21] J. L. Roberts, N. R. Claussen, J. P. Burke, C. H. Green, E. A. Cornell, and C. E. Wieman. Resonant magnetic field control of elastic scattering in cold ^{85}Rb. *Phys. Rev. Lett.*, 81:5109, 1998.

[22] V. Vuletić, A. J. Kerman, C. Chin, and S. Chu. Observation of low-field Feshbach resonances in collisions of cesium atoms. *Phys. Rev. Lett.*, 82:1406, 1999.

[23] S. L. Cornish, N. R. Claussen, J. L. Roberts, C. E. Cornell, and C. E. Wieman. Stable ^{85}Rb Bose-Einstein condensates with widely tunable interactions. *Phys. Rev. Lett.*, 85:1795, 2000.

[24] E. A. Donley, N. R. Claussen, S. L. Cornish, J. L. Roberts, E. A. Cornell, and C. E. Wieman. Dynamics of collapsing and exploding Bose-Einstein condensates. *Nature*, 412:295, 2001.

[25] E. A. Donley, N. R. Claussen, S. T. Thompson, and C. E. Wieman. Atom-molecule coherence in a Bose-Einstein condensate. *Nature*, 417:529, 2002.

[26] E. Timmermans, P. Tommasini, R. Côté, M. Hussein, and A. Kerman. Rarified liquid properties of hybrid atomic-molecular Bose-Einstein condensates. *Phys. Rev. Lett.*, 83:2691, 1999.

[27] E. Timmermans, P. Tommasini, M. Hussein, and A. Kerman. Feshbach resonances in atomic Bose-Einstein condensates. *Phys. Rep.*, 315:199, 1999.

[28] M. Holland, S. J. J. M. F. Kokkelmans, M. L. Chiofalo, and R. Walser. Resonance superfluidity in a quantum degenerate Fermi gas. *Phys. Rev. Lett.*, 87:120406, 2001.

[29] E. Timmermans, K. Furuya, P. W. Milonni, and A. K. Kerman. Prospect of creating a composite Fermi-Bose fluid. *Phys. Lett. A*, 285:228, 2001.

[30] Y. Ohashi and A. Griffin. BCS-BEC crossover in a gas of Fermi atoms with a Feshbach resonance. *Phys. Rev. Lett.*, 89:130402, 2002.

[31] T. Loftus, C. A. Regal, C. Ticknor, J. L. Bohn, and D. S. Jin. Resonant control of elastic scattering in an optically trapped Fermi gas of atoms. *Phys. Rev. Lett.*, 88:173201, 2002.

[32] L. Khaykovich, F. Schreck, G. Ferrari, T. Bourdel, J. Cubizolles, L. D. Carr, Y. Castin, and C. Salomon. Formation of a matter-wave bright soliton. *Science*, 296:1290, 2002.

[33] K. E. Strecker, G. B. Partridge, A. G. Truscott, and R. G. Hulet. Formation and propagation of matter-wave soliton trains. *Nature*, 417:150, 2002.

[34] K. Dieckmann, C. A. Stan, S. Gupta, Z. Hadzibabic, C. H. Schunck, and W. Ketterle. Decay of an ultracold fermionic lithium gas near a Feshbach resonance. *Phys. Rev. Lett.*, 89:203201, 2002.

[35] S. Jochim, M. Bartenstein, G. Hendl, C. Chin, J. Hecker-Denschlag, R. Grimm, A. Mosk, and M. Weidemüller. Magnetic field control of elastic scattering in a cold gas of fermionic lithium atoms. *Phys. Rev. Lett.*, 91:240402, 2002.

[36] K. M. O'Hara, S. L. Hemmer, M. E. Gehm, S. R. Granada, and J. E. Thomas. Observation of a strongly interacting degenerate Fermi gas of atoms. *Science*, 298:2179, 2002.

[37] A. Marte, T. Volz, J. Schuster, S. Dürr, G. Rempe, E. G. M. van Kempen, and B. J. Verhaar. Feshbach resonances in rubidium 87: precision measurement and analysis. *Phys. Rev. Lett.*, 89:283202, 2002.

[38] A. Moerdijk, H. M. J. M. Boesten, and B. J. Verhaar. Collisions of dressed ground-state atoms. *Phys. Rev. A*, 53:916, 1996.

[39] M. Marinescu and L. You. Controlling atom-atom interaction at ultralow temperatures by dc electric fields. *Phys. Rev. Lett.*, 81:4596, 1998.

[40] P. O. Fedichev, Y. Kagan, G. V. Shlyapnikov, and J. T. M. Valraven. Influence of nearly resonant light on the scattering length in low-temperature gases. *Phys. Rev. Lett.*, 77:2913, 1996.

[41] F. K. Fatemi, K. M. Jones, and P. D. Lett. Observation of optically induced Feshbach resonances in collisions of cold atoms. *Phys. Rev. Lett.*, 85:4462, 2000.

[42] M. Theis, G. Thalhammer, K. Winkler, M. Hellwig, G. Ruff, R. Grimm, and J. Hecker-Denschlag. Tuning the scattering length with an optically induced Feshbach resonance. *Phys. Rev. Lett*, 93:123001, 2004.

[43] G. Thalhammer, M. Theis, K. Winkler, R. Grimm, and J. Hecker-Denschlag. Inducing an optical Feshbach resonance via stimulated Raman coupling. *Phys. Rev. A*, 71:033403, 2005.

[44] J. J. Hudson, H. T. Ashworth P. C. Condylis, M. R. Tarbutt, B. E. Sauer, and E. A. Hinds. Towards a new measurement of the electrons's dipole moment. In E. A. Hinds, E. Ferguson, and E. Riis, editors, *Proceedings of the 17th International Conference on Laser Spectroscopy*, pages 129–136. World Scientific Publ., Singapore, 2005.

[45] L. Santos, G. V. Shlyapnikov, P. Zoller, and M. Lewenstein. Bose-Einstein condensation in trapped dipolar gases. *Phys. Rev. Lett.*, 85:1791, 2000.

[46] A. Griesmaier, J. Stuhler, T. Koch, M. Fattori, T. Pfau, and S. Giovannazzi. Comparing contact and dipolar interactions in a Bose-Einstein condensate. *Phys. Rev. Lett.*, 97:250402, 2006.

[47] J. D. Weinstein, R. deCarvalho, T. Guillet, B. Friedrich, and J. M. Doyle. Magnetic trapping of calcium monohydride molecules at millikelvin temperatures. *Nature*, 395:148, 1995.

[48] H. L. Bethlem, G. Berden, and G. Meijer. Decelerating neutral dipolar molecules. *Phys. Rev. Lett.*, 83:1558, 1999.

[49] J. Doyle, B. Friedrich, R. V. Krems, and F. Masnou-Seeuws. Quo vadis, cold molecules? *European Phys. J. D*, 31:149, 2004.

[50] F. H. Mies, E. Tiesinga, and P. S. Julienne. Manipulation of Feshbach resonances in ultracold atomic collisions using time-dependent magnetic fields. *Phys. Rev. A*, 61:022721, 2000.

[51] C. A. Regal, C. Ticknor, J. L. Bohn, and D. S. Jin. Creation of ultracold molecules from a Fermi gas of atoms. *Nature*, 424:47, 2003.

[52] J. Herbig, T. Kraemer, M. Mark, T. Weber, C. Chin, H.-C. Nägerl, and R. Grimm. Preparation of a pure molecular quantum gas. *Science*, 301:1510, 2003.

[53] S. Dürr, T. Volz, A. Marte, and G. Rempe. Observation of molecules produced from a Bose-Einstein condensate. *Phys. Rev. Lett.*, 92:020406, 2004.

[54] J. Cubizolles, T. Bourdel, S. J. J. M. F. Kokkelmans, G. V. Shlyapnikov, and C. Salomon. Production of long-lived ultracold Li_2 molecules from a Fermi gas. *Phys. Rev. Lett.*, 91:240401, 2003.

[55] K. E. Strecker, G. B. Partridge, and R. G. Hulet. Conversion of an atomic Fermi gas to a long-lived molecular Bose gas. *Phys. Rev. Lett.*, 91:080406, 2003.

[56] K. Xu, T. Mukaiyama, J. R. Abo-Shaeer, J. K. Chin, D. E. Miller, and W. Ketterle. Formation of quantum-degenerate sodium molecules. *Phys. Rev. Lett.*, 91:210402, 2003.

[57] S. Jochim, M. Bartenstein, A. Altmeyer, G. Hendl, S. Riedl, C. Chin, J. Hecker-Denschlag, and R. Grimm. Bose-Einstein condensation of molecules. *Science*, 302:2101, 2003.

[58] M. W. Zwierlein, C. A. Stan, C. H. Schunck, S. M. F. Raupach, S. Gupta, Z. Hadzibabic, and W. Ketterle. Observation of Bose-Einstein condensation of molecules. *Phys. Rev. Lett.*, 91:250401, 2003.

[59] T. Mukaiyama, J. R. Abo-Shaeer, K. Xu, J. K. Chin, and W. Ketterle. Dissociation and decay of ultracold Feshbach molecules. *Phys. Rev. Lett.*, 92:180402, 2004.

[60] C. Chin, T. Kraemer, M. Mark, J. Herbig, P. Waldburger, H.-C. Nägerl, and R. Grimm. Observation of Feshbach-like resonances in collisions between ultracold molecules. *Phys. Rev. Lett.*, 94:123201, 2005.

[61] N. Syassen, T. Volz, S. Teichmann, S. Dürr, and G. Rempe. Collisional decay of ^{87}Rb Feshbach molecules at 1005.8 G. *Phys. Rev. A*, 74:062706, 2006.

[62] C. A. Regal, M. Greiner, and D. S. Jin. Lifetime of molecule-atom mixtures near a Feshbach resonance in ^{40}K. *Phys. Rev. Lett.*, 92:083201, 2004.

[63] D. S. Petrov, C. Salomon, and G. V. Shlyapnikov. Weakly bound dimers of fermionic atoms. *Phys. Rev. Lett.*, 93:090404, 2004.

[64] M. Greiner, C. A. Regal, and D. S. Jin. Emergence of a molecular Bose-Einstein condensate from a Fermi gas. *Nature*, 426:537, 2003.

[65] C. A. Regal, M. Greiner, and D. S. Jin. Observation of resonance condensation of fermionic atom pairs. *Phys. Rev. Lett.*, 92:040403, 2004.

[66] M. Bartenstein, A. Altmeyer, S. Riedl, S. Jochim, C. Chin, J. Hecker-Denschlag, and R. Grimm. Crossover from a molecular Bose-Einstein condensate to a degenerate Fermi gas. *Phys. Rev. Lett.*, 92:120401, 2004.

[67] M. W. Zwierlein, C. A. Stan, C. H. Schunck, S. M. F. Raupach, A. J. Kerman, and W. Ketterle. Condensation of pairs of fermionic atoms near a Feshbach resonance. *Phys. Rev. Lett.*, 92:120403, 2004.

[68] M. W. Zwierlein, J. R. Abo-Shaeer, A. Schirotzek, C. H. Schunck, and W. Ketterle. Vortices and superfluidity in a strongly interacting Fermi gas. *Nature*, 435:1047, 2005.

[69] E. Hodby, S. T. Thompson, C. A. Regal, M. Greiner, A. C. Wilson, D. S. Jin, E. A. Cornell, and C. E. Wieman. Production efficiency of ultracold Feshbach molecules in bosonic and fermionic systems. *Phys. Rev. Lett.*, 94:120402, 2005.

[70] S. T. Thompson, E. Hodby, and C. E. Wieman. Spontaneous dissociation of ^{85}Rb Feshbach molecules. *Phys. Rev. Lett.*, 94:020401, 2005.

[71] S. Dürr, T. Volz, and G. Rempe. Dissociation of ultracold molecules with Feshbach resonances. *Phys. Rev. A*, 70:031601, 2004.

[72] S. T. Thompson, E. Hodby, and C. E. Wieman. Ultracold molecule production via a resonant oscillating magnetic field. *Phys. Rev. Lett.*, 95:190404, 2005.

[73] J. R. Abo-Shaeer, D. E. Miller, J. K. Chin, K. Xu, T. Mukaiyama, and W. Ketterle. Coherent molecular optics using ultracold sodium dimers. *Phys. Rev. Lett.*, 94:040405, 2005.

[74] G. Thalhammer, K. Winkler, F. Lang, S. Schmid, R. Grimm, and J. Hecker-Denschlag. Long-lived Feshbach molecules in a three-dimensional optical lattice. *Phys. Rev. Lett.*, 96:050402, 2006.

[75] T. Stöferle, H. Moritz, K. Günter, M. Köhl, and T. Esslinger. Molecules of fermionic atoms in an optical lattice. *Phys. Rev. Lett.*, 96:030401, 2006.

[76] T. Volz, N. Syassen, D. M. Bauer, E. Hansis, S. Dürr, and G. Rempe. Preparation of a quantum state with one molecule at each site of an optical lattice. *Nature Physics*, 2:692, 2006.

[77] K. Winkler, F. Lang, G. Thalhammer, P. v. d. Straten, R. Grimm, and J. Hecker-Denschlag. Coherent optical transfer of Feshbach molecules to a lower vibrational state. *Phys. Rev. Lett.*, 98:043201, 2007.

[78] K. M. Jones, E. Tiesinga, P. D. Lett, and P. S. Julienne. Ultracold photoassociation spectroscopy: long-range molecules and atomic scattering. *Rev. Mod. Phys.*, 78:483, 2006.

[79] J. Schuster. *Stoßlawinen in einem Bose-Einstein-Kondensat*. PhD thesis, Max-Planck-Institut für Quantenoptik, Garching, and Universität Konstanz, 2002. Unpublished, e-print available at http://www.ub.uni-konstanz.de/kops/volltexte/2002/868.

[80] A. Marte. *Feshbach-Resonanzen bei Stößen ultrakalter Rubidiumatome*. PhD thesis, Max-Planck-Institut für Quantenoptik, Garching, and Technische Universität München, November 2003. Unpublished, e-print available at http://tumb1.biblio.tu-muenchen.de/publ/diss/ph/2003/marte.html.

[81] B. Sang. *Magnetische Speicherung eines ultrakalten atomaren Gases für die Bose-Einstein-Kondensation*. Diplomarbeit, Max-Planck-Institut für Quantenoptik, Garching, and Universität Konstanz, 2001. Unpublished.

[82] T. Volz. *Feshbach Resonances in Rubidium 87*. Diplomarbeit, Max-Planck-Institut für Quantenoptik, Garching, and Universität Konstanz, 2002. Unpublished.

[83] H. Metcalf and P. van der Straten. *Laser Cooling and Trapping*. Springer, Heidelberg, 1999.

[84] W. Ketterle and N. J. van Druten. Evaporative cooling of trapped atoms. In B. Bederson and H. Walther, editors, *Advances in Atomic, Molecular and Optical Physics*, volume 37, pages 181–236. Academic Press, San Diego, 1996.

[85] G. C. Bjorklund, M. D. Levenson, W. Lenth, and C. Ortiz. Frequency modulation (fm) spectroscopy. *Appl. Phys. B*, 32:145, 1983.

[86] D. E. Pritchard. Cooling neutral atoms in a magnetic trap for precision spectroscopy. *Phys. Rev. Lett.*, 51:1336, 1983.

[87] A. L. Migdall, J. V. Prodan, W. D. Phillips, T. H. Bergeman, and H. J. Metcalf. First observation of magnetically trapped neutral atoms. *Phys. Rev. Lett.*, 54:2596, 1985.

[88] Y. Castin and R. Dum. Bose-Einstein condensates in time dependent traps. *Phys. Rev. Lett.*, 77:5315, 1996.

[89] U. Ernst, J. Schuster, F. Schreck, A. Marte, A. Kuhn, and G. Rempe. Free expansion of a Bose-Einstein condensate from an Ioffe-Pritchard magnetic trap. *Appl. Phys. B*, 67:719, 1998.

[90] R. Grimm, M. Weidemüller, and Y. B. Ovchinnikov. Optical dipole traps for neutral atoms. In B. Bederson and H. Walther, editors, *Advances in Atomic, Molecular and Optical Physics*, volume 42, pages 95–170. Academic Press, San Diego, 2000.

[91] F. Bloch and A. Siegert. Magnetic resonance for nonrotating fields. *Phys. Rev.*, 57:522, 1940.

[92] A. E. Siegman. *Lasers*. University Science Books, Sausalito, 1986.

[93] T. A. Savard, K. M. O'Hara, and J. E. Thomas. Laser-noise-induced heating in far-off resonance optical traps. *Phys. Rev. A*, 56:1095, 1997.

[94] M. E. Gehm, K. M. O'Hara, T. A. Savard, and J. E. Thomas. Dynamics of noise-induced heating in atom traps. *Phys. Rev. A*, 58:3914, 1998.

[95] N. F. Ramsey. *Molecular beams*. Oxford University Press, Oxford, 1956.

[96] P. S. Jessen and I. H. Deutsch. Optical lattices. In B. Bederson and H. Walther, editors, *Advances in Atomic, Molecular and Optical Physics*, volume 37, pages 95–138. Academic Press, San Diego, 1996.

[97] M. Greiner. *Ultracold quantum gases in three-dimensional optical lattice potentials*. PhD thesis, Ludwig-Maximilians-Universität, München, 2001. Unpublished.

[98] N. W. Ashcroft and N. D. Mermin. *Solid State Physics*. Brooks/Cole, Pacific Grove, 1976.

[99] J. Hecker-Denschlag, J. E. Simsarian, H. Häffner, C. McKenzie, A. Browaeys, D. Cho, K. Helmerson, S. L. Rolston, and W. D. Phillips. A Bose-Einstein condensate in an optical lattice. *J. Phys. B*, 35:3095, 2002.

[100] S. Dürr, S. Kunze, and G. Rempe. Pendellösung oscillations in second-order Bragg scattering of atoms from a standing light wave. *Quantum Semiclass. Opt.*, 8:531, 1996.

[101] Y. B. Band, M. Trippenbach, J. P. Burke, and P. S. Julienne. Elastic scattering loss of atoms from colliding Bose-Einstein condensate wave packets. *Phys. Rev. Lett.*, 84:5462, 2000.

[102] A. P. Chikkatur, A. Görlitz, D. M. Stamper-Kurn, S. Inouye, S. Gupta, and W. Ketterle. Suppression and enhancement of impurity scattering in a Bose-Einstein condensate. *Phys. Rev. Lett.*, 85:483, 2000.

[103] M. Greiner, O. Mandel, T. Esslinger, T. W. Hänsch, and I. Bloch. Quantum phase transition from a superfluid to a Mott insulator in a gas of ultracold atoms. *Nature*, 415:39, 2002.

[104] M. B. Dahan, E. Peik, J. Reichel, Y. Castin, and C. Salomon. Bloch oscillations of atoms in an optical potential. *Phys. Rev. Lett.*, 76:4508, 1996.

[105] T. Volz, S. Dürr, S. Ernst, A. Marte, and G. Rempe. Characterization of elastic scattering near a Feshbach resonance in ^{87}Rb. *Phys. Rev. A*, 68:010702, 2003.

[106] C. J. Joachain. *Quantum collision theory.* North-Holland, Amsterdam, 1975.

[107] J. R. Taylor. *Scattering Theory.* Wiley, New York, 1972.

[108] J. J. Sakurai. *Modern Quantum Mechanics.* Addison-Wesley, Reading, 1994.

[109] J. Dalibard. Collisional dynamics of ultra-cold atomic gases. In M. Inguscio, S. Stringari, and C. E. Wieman, editors, *Proceedings of the international school of physics, "Enrico Fermi", Course CXL: Bose-Einstein condensation in atomic gases*, pages 321–349. IOS Press, Amsterdam, 1998.

[110] L. D. Landau and E. M. Lifshitz. *Quantum mechanics. Non-relativistic theory.* Pergamon Press, Oxford, third (revised and enlarged) edition, 1977.

[111] H. M. J. M. Boesten, C. C. Tsai, J. R. Gardner, D. J. Heinzen, and B. J. Verhaar. Observation of a shape resonance in the collision of two cold ^{87}Rb atoms. *Phys. Rev. A*, 55:636, 1997.

[112] T. Busch, B. G. Englert, K. Rzazewski, and M. Wilkens. Two cold atoms in a harmonic trap. *Founds. Phys.*, 28:549, 1998.

[113] N. N. Bogoliubov. *J. Phys. (USSR)*, 11:23, 1947.

[114] E. P. Gross. Structure of a quantized vortex in boson systems. *Nuovo Cimento*, 20:454, 1961.

[115] L. P. Pitaevskii. Vortex lines in an imperfect Bose gas. *Sov. Phys. JETP-USSR*, 13:451, 1961.

[116] F. Dalfovo, S. Giorgini, L. P. Pitaevskii, and S. Stringari. Theory of Bose-Einstein condensation in trapped gases. *Rev. Mod. Phys.*, 71:463, 1999.

[117] K. W. Madison, F. Chevy, W. Wohlleben, and J. Dalibard. Vortex formation in a stirred Bose-Einstein condensate. *Phys. Rev. Lett.*, 84:806, 2000.

[118] C. C. Bradley, C. A. Sackett, and R. G. Hulet. Bose-Einstein condensation of Lithium: observation of limited condensate number. *Phys. Rev. Lett.*, 78:985, 1997.

[119] H. A. Feshbach. *Nuclear Reactions*. Wiley, New York, 1992.

[120] A. Moerdijk, B. J. Verhaar, and A. Axelsson. Resonances in ultracold collisions of ^{6}Li, ^{7}Li, and ^{23}Na. *Phys. Rev. A*, 51:4852, 1995.

[121] F. A. van Abeelen. *Interaction processes in cold gases of alkali atoms*. PhD thesis, Technical University Eindhoven, 1999. ISBN 90-386-0937-X.

[122] K. Góral, T. Köhler, S. A. Gardiner, E. Tiesinga, and P. Julienne. Adiabatic association of ultracold molecules via magnetic-field tunable interactions. *J. Phys. B*, 37:3457, 2004.

[123] M. Mark, T. Kraemer, J. Herbig, C. Chin, H.-C. Nägerl, and R. Grimm. Efficient creation of molecules from a cesium Bose-Einstein condensate. *Europhys. Lett.*, 69:706, 2005.

[124] J. Stenger, S. Inouye, M. R. Andrews, H.-J. Miesner, D. M. Stamper-Kurn, and W. Ketterle. Strongly enhanced inelastic collisions in a Bose-Einstein condensate near Feshbach resonances. *Phys. Rev. Lett.*, 82:2422, 1999.

[125] J. L. Roberts, J. P. Burke, N. R. Claussen, S. L. Cornish, E. A. Donley, and C. E. Wieman. Improved characterization of elastic scattering near a Feshbach resonance in ^{85}Rb. *Phys. Rev. A*, 64:24702, 2001.

[126] G. Smirne, R. M. Godun, D. Cassettari, V. Boyer, C. J. Foot, T. Volz, N. Syassen, S. Dürr, G. Rempe, M. D. Lee, K. Góral, and T. Köhler. Collisional relaxation of Feshbach molecules and three-body recombination in ^{87}Rb Bose-Einstein condensates. *Phys. Rev. A*, 75:020702, 2007.

[127] N. R. Claussen, E. A. Donley, S. T. Thompson, and C. E. Wieman. Microscopic dynamics in a strongly interacting Bose-Einstein condensate. *Phys. Rev. Lett.*, 89:10401, 2002.

[128] E. G. M. van Kempen and B. J. Verhaar. Personal communication.

[129] C. A. Sackett, J. M. Gerton, M. Welling, and R. G. Hulet. Measurements of collective collapse in a Bose-Einstein condensate with attractive interactions. *Phys. Rev. Lett.*, 82:876, 1998.

[130] J. M. Gerton, D. Strekalov, I. Prodan, and R. G. Hulet. Direct observation of growth and collapse of a Bose-Einstein condensate with attractive interactions. *Nature*, 408:692, 2000.

[131] J. L. Roberts, N. R. Claussen, S. L. Cornish, E. A. Donley, E. A. Cornell, and C. E. Wieman. Controlled collapse of a Bose-Einstein condensate. *Phys. Rev. Lett.*, 86:4211, 2001.

[132] J. K. Chin, J. M. Vogels, and W. Ketterle. Amplification of local instabilites in a Bose-Einstein condensate with attractive interactions. *Phys. Rev. Lett.*, 90:160405, 2003.

[133] N. R. Claussen, S. J. J. M. F. Kokkelmans, S. T. Thompson, E. A. Donley, E. Hodby, and C. E. Wieman. Very-high-precision bound-state spectroscopy near a ^{85}Rb Feshbach resonance. *Phys. Rev. A*, 67:060701, 2003.

[134] J. R. Rubbmark, M. M. Kash, M. G. Littman, and D. Kleppner. Dynamical effects at avoided level crossings: a study of the Landau-Zener effect using Rydberg atoms. *Phys. Rev. A*, 23:3107, 1981.

[135] P. S. Julienne, E. Tiesinga, and T. Köhler. Making cold molecules by time-dependent Feshbach resonances. *J. Mod. Opt.*, 51:1787, 2004.

[136] E. Hansis. *Ultracold molecules in an optical lattice.* Diplomarbeit, Max-Planck-Institut für Quantenoptik, Garching, and Technische Universität München, 2006. Unpublished.

[137] M. Holland, J. Park, and R. Walser. Formation of pairing fields in resonantly coupled atomic and molecular Bose-Einstein condensates. *Phys. Rev. Lett.*, 86:1915, 2001.

[138] S. J. J. M. F. Kokkelmans and M. J. Holland. Ramsey fringes in a Bose-Einstein condensate between atoms and molecules. *Phys. Rev. Lett.*, 89:180401, 2002.

[139] T. Köhler, T. Gasenzer, and K. Burnett. Microscopic theory of atom-molecule oscillations in a Bose-Einstein condensate. *Phys. Rev. A*, 67:013601, 2003.

[140] F. A. van Abeelen and B. J. Verhaar. Time-dependent Feshbach resonance scattering and anomalous decay of a Na Bose-Einstein condensate. *Phys. Rev. Lett.*, 83:1550, 1999.

[141] V. A. Yurovsky and A. Ben-Reuven. Formation of molecules in an expanding Bose-Einstein condensate. *Phys. Rev. A*, 70:013613, 2004.

[142] V. A. Yurovsky, A. Ben-Reuven, P. S. Julienne, and C. J. Williams. Atom loss from a Bose-Einstein condensate due to Feshbach resonance. *Phys. Rev. A*, 60:765, 1999.

[143] E. G. M. van Kempen and B. J. Verhaar. Personal communication.

[144] T. Köhler, K. Góral, and P. S. Julienne. Production of cold molecules via magnetically tunable Feshbach resonances. *Rev. Mod. Phys.*, 78:1311, 2006.

[145] T. M. Hanna, K. Góral, E. Witkowska, and T. Köhler. Classification of zero-energy resonances by dissociation of Feshbach molecules. *Phys. Rev. A*, 74:023618, 2006.

[146] S. Brouard and J. Plata. Dissociation of ultracold molecules via Feshbach resonances: the effect of magnetic-field fluctuations. *Phys. Rev. A*, 72:023620, 2005.

[147] T. Volz, S. Dürr, N. Syassen, G. Rempe, E. van Kempen, and S. Kokkelmans. Feshbach spectroscopy of a shape resonance. *Phys. Rev. A*, 72:010704, 2005.

[148] S. Dürr, T. Volz, N. Syassen, G. Rempe, E. van Kempen, S. Kokkelmans, B. J. Verhaar, and H. Friedrich. Dissociation of Feshbach molecules into different partial waves. *Phys. Rev. A*, 72:052707, 2005.

[149] C. Cohen-Tannoudji, J. Dupont-Roc, and G. Grynberg. *Atom-Photon Interactions*, pages 49–59. Wiley, New York, 1992.

[150] N. R. Thomas, N. Kjaergaard, P. S. Julienne, and A. C. Wilson. Imaging of s and d partial-wave interference in quantum scattering of identical bosonic atoms. *Phys. Rev. Lett.*, 93:173201, 2004.

[151] Ch. Buggle, J. Léonard, W. von Klitzing, and J. T. M. Walraven. Interferometric determination of the s and d-wave scattering amplitudes in ^{87}Rb. *Phys. Rev. Lett.*, 93:173202, 2004.

[152] Ch. Buggle, J. Léonard, W. von Klitzing, and J. T. M. Walraven. Bose-Einstein condensates studied with a linear accelerator. In E. A. Hinds, E. Ferguson, and E. Riis, editors, *Proceedings of the 17th International Conference on Laser Spectroscopy*, pages 199–206. World Scientific Publ., Singapore, 2005.

[153] M. Born and E. Wolf. *Principles of Optics*, pages 217–227. Cambridge University Press, 7th (expanded) edition, 1999.

[154] R. Ozeri, J. Steinhauer, N. Katz, and N. Davidson. Direct observation of the phonon energy in a Bose-Einstein condensate by tomographic imaging. *Phys. Rev. Lett.*, 88:220401, 2002.

[155] M. L. Du and A. Dalgarno. Artificial-channel method for multichannel-decay-resonance energies and widths. *Phys. Rev. A*, 43:3474, 1991.

[156] M. Machholm, A. Giusti-Suzor, and F. H. Mies. Photoassociation of atoms in ultracold collisions probed by wave-packet dynamics. *Phys. Rev. A*, 50:5025, 1994.

[157] E. Wells, K. D. Carnes, B. D. Esry, and I. Ben-Itzhak. Charge transfer and elastic scattering in very slow H^++D(1s) half collisions. *Phys. Rev. Lett.*, 86:4803, 2001.

[158] T. Schneider and J.-M. Rost. Double photoionization of two-electron atoms based on the explicit separation of dominant ionization mechanisms. *Phys. Rev. A*, 67:062704, 2003.

[159] S. J. J. M. F. Kokkelmans. *Interacting atoms in clocks and condensates*. PhD thesis, Technical University Eindhoven, 2000. ISBN 90-386-1569-8.

[160] K. Góral, L. Santos, and M. Lewenstein. Quantum phases of dipolar bosons in optical lattices. *Phys. Rev. Lett.*, 88:170406, 2002.

[161] A. Micheli, G. K. Brennen, and P. Zoller. A toolbox for lattice-spin models with polar molecules. *Nature Physics*, 2:341, 2006.

[162] R. Barnett, D. Petrov, M. Lukin, and E. Demler. Quantum magnetism with multicomponent dipolar molecules in an optical lattice. *Phys. Rev. Lett.*, 96:190401, 2006.

[163] D. DeMille. Quantum computation with trapped polar molecules. *Phys. Rev. Lett.*, 88:067901, 2002.

[164] C. Lee and E. A. Ostrovskaya. Quantum computation with diatomic bits in optical lattices. *Phys. Rev. A*, 72:062321, 2005.

[165] S. Dürr, T. Volz, N. Syassen, D. M. Bauer, E. Hansis, and G. Rempe. A Mott-like state of molecules. In C. Roos, H. Häffner, and R. Blatt, editors, *Proceedings of the 20th International Conference on Atomic Physics*, pages 199–206. AIP Conference Proceedings, Melville, 2006.

[166] D. Jaksch, C. Bruder, J. I. Cirac, C. W. Gardiner, and P. Zoller. Cold bosonic atoms in optical lattices. *Phys. Rev. Lett.*, 81:3108, 1998.

[167] M. P. A. Fisher, P. B. Weichmann, G. Grinstein, and D. S. Fisher. Boson localization and the superfluid-insulator transition. *Phys. Rev. B*, 40:546, 1989.

[168] D. Jaksch. *Bose-Einstein Condensation and Applications*. PhD thesis, Leopold-Franzens-Universität Innsbruck, Austria, 1999. Unpublished.

[169] M. Zwerger. Mott-Hubbard transition of cold atoms in optical lattices. *Journal of Optics B: Quantum and Semiclassical Optics*, 5:S9, 2003.

[170] J. J. Garcia-Ripoll. Personal communication.

[171] K. Sheshadri, H. R. Krishnamurthy, R. Pandit, and T. V. Ramakrishnan. Superfluid and insulating phases in an interacting-boson model: mean-field theory and the RPA. *Europhys. Lett.*, 22:257, 1993.

[172] J. K. Freericks and H. Monien. Phase diagram of the Bose-Hubbard model. *Europhys. Lett.*, 26:545, 1995.

[173] D. van Oosten, P. van der Straten, and H. T. C. Stoof. Quantum phases in an optical lattice. *Phys. Rev. A*, 63:053601, 2001.

[174] S. Fölling, A. Widera, T. Müller, F. Gerbier, and I. Bloch. Formation of spatial shell structure in the superfluid to Mott insulator transition. *Phys. Rev. Lett.*, 97:060403, 2006.

[175] G. K. Campbell, J. Mun, M. Boyd, P. Medley, A. E. Leanhardt, L. G. Marcassa, D. E. Pritchard, and W. Ketterle. Imaging the Mott insulator shells by using atomic clock shifts. *Science*, 313:649, 2006.

[176] T. Rom, T. Best, O. Mandel, A. Widera, M. Greiner, T. W. Hänsch, and I. Bloch. State selective production of molecules in optical lattices. *Phys. Rev. Lett.*, 93:073002, 2004.

[177] K. Winkler, G. Thalhammer, F. Lang, R. Grimm, J. Hecker-Denschlag, A. J. Daley, A. Kantian, H. P. Büchler, and P. Zoller. Repulsively bound atom pairs in an optical lattice. *Nature*, 441:853, 2006.

[178] C. Ryu, X. Du, E. Yesilada, A. M. Dudarev, S. Wan, Q. Niu, and D. J. Heinzen. Raman-induced oscillations between an atomic and a molecular quantum gas. *e-print available at http://arXiv.org/abs/cond-mat/0508201*, 2005.

[179] F. Gerbier, A. Widera, S. Fölling, O. Mandel, T. Gericke, and I. Bloch. Phase coherence of an atomic Mott insulator. *Phys. Rev. Lett.*, 95:050404, 2005.

[180] T. Stöferle, H. Moritz, C. Schori, M. Köhl, and T. Esslinger. Transition from a strongly interacting 1D superfluid to a Mott insulator. *Phys. Rev. Lett.*, 92:130403, 2004.

[181] D. Jaksch, V. Venturi, J. I. Cirac, C. J. Williams, and P. Zoller. Creation of a molecular condensate by dynamically melting a Mott insulator. *Phys. Rev. Lett.*, 89:040402, 2002.

[182] C. Ospelkaus, S. Ospelkaus, L. Humbert, P. Ernst, K. Sengstock, and K. Bongs. Ultracold heteronuclear molecules in a 3D optical lattice. *Phys. Rev. Lett.*, 97:120402, 2006.

[183] S. B. Papp and C. E. Wieman. Observation of heteronuclear Feshbach molecules from a ^{85}Rb -^{87}Rb gas. *Phys. Rev. Lett.*, 97:180404, 2006.

[184] M. W. Mancini, G. D. Telles, A. R. L. Caires, V. S. Bagnato, and L. G. Marcassa. Observation of ultracold ground-state heteronuclear molecules. *Phys. Rev. Lett.*, 92:133203, 2004.

[185] J. M. Sage, S. Sainis, T. Bergeman, and D. DeMille. Optical production of ultracold polar molecules. *Phys. Rev. Lett.*, 94:203001, 2005.

[186] T. Kraemer, M. Mark, P. Waldburger, J. G. Danzl, C. Chin, B. Engeser, A. D. Lange, K. Pilch, A. Jaakkola, H.-C. Nägerl, and R. Grimm. Evidence for Efimov quantum states in an ultracold gas of caesium atoms. *Nature*, 440:315, 2006.

[187] M. Stoll and T. Köhler. Production of three-body Efimov molecules in an optical lattice. *Phys. Rev. A*, 72:022714, 2005.

Danksagung

Zu guter Letzt gilt es, all denjenigen meinen Dank auszusprechen, ohne die das Gelingen der vorliegenden Arbeit undenkbar gewesen wäre.

Zuvorderst ist hier mein Doktorvater Gerhard Rempe zu nennen, der mir die Möglichkeit gegeben hat, an einer technisch ausgefeilten Apparatur an hochaktuellen Fragestellungen auf dem Gebiet der ultrakalten Quantengase zu arbeiten. Er hat mir stets großes Vertrauen entgegengebracht und mir viel Freiraum beim Umsetzen eigener Ideen gewährt.

Gleich als nächstes sei hier unser Habilitand Stephan Dürr erwähnt, mit dem ich die ersten anderthalb Jahre meiner Doktorarbeit im Labor verbracht und von dem ich eine gute Portion Pragmatismus gelernt habe. Auf meine zahlreichen physikalischen Fragen hat er stets mit großer Geduld und in aller Ausführlichkeit geantwortet. Sein Ruf als phänomenaler Rechenkünstler, der auch die letzten Faktoren 2 findet, eilt ihm voraus. Besonderer Dank gilt ihm für das kritische Korrekturlesen dieser Arbeit und die wertvollen Verbesserungsvorschläge - und natürlich auch für die gemeinsamen Champions-League-Abende bei Pizza und Bier.

Ganz herzlich möchte ich mich auch bei meinen beiden Mitdoktoranden Niels Syassen und Dominik Bauer bedanken, die beide großen Anteil am Gelingen insbesondere der Gitterexperimente hatten. Während Computerexperte Niels mit einer neuen Steuerung das Experiment in das 21. Jahrhundert katapultiert hat, hat Dominik mit großer Sorgfalt den Gitterlaser aufgebaut und betreut. Die Zusammenarbeit mit Niels und Dominik hat für mich den Begriff Teamarbeit neu definiert. Nicht zuletzt danke ich den beiden auch für die gemeinsamen Ausflüge in die Berge und den ein oder anderen gemütlichen Abend bei einem kühlen BECk's.

Darüber hinaus seien hier die Diplomanden Sebastian Ernst, Sven Teichmann und Eberhard Hansis genannt. Eberhard möchte ich besonders hervorheben, da er sich zusammen mit Niels um die neue Experimentsteuerung verdient gemacht hat.

Die Vielzahl an spannenden Experimenten wurde erst durch die fantastische Apparatur ermöglicht. Meine beiden Vorgänger Andreas Marte und Johannes Schuster haben die Apparatur mit der größtmöglichen Sorgfalt aufgebaut. Im gleichen Atemzug muß hier auch unsere sehr kompetente "technische Abteilung" genannt werden. Den bayrischen Charme von Helmuth Stehbeck, Franz Denk, Tom Wiesmaier und Joseph Bayerl werde ich sicherlich in Zukunft vermissen.

Ohne Unterstützung von theoretischer Seite wären sicherlich einige der experimentellen Ergebnisse unverstanden geblieben. Im Laufe der Jahre gab es zahlreiche Diskussionen mit Boudewijn Verhaar, Eric van Kempen und Servaas Kokkelmans über Zwei-Köper-Stöße. Harald Friedrich hat uns geholfen, Streuprobleme mit vielen Partialwellen zu verstehen. Zu Molekülen im Gitter und ihren Transporteigenschaften gab es intensiven Gedankenaustausch mit Ignacio Cirac und Juan Jose Garcia-Ripoll.

Schließlich möchte ich mich auch bei der ganzen Gruppe Rempe für die freund-

liche Atmosphäre und die gute Laune bei diversen Grillfesten, Skitagen und Gruppenseminaren in Rechtegg und auf Schloss Ringberg bedanken. Ich hatte immer das Gefühl, dass bei allen Experimenten die (Labor-) Türe offen stand und gerne Fragen beantwortet wurden. Nicht-gebrauchte Gerätschaften und sonstiges Labormaterial wurden stets bereitwillig verliehen. Hier sei besonders Jörg Bochmann gedankt, der uns in der Stunde großer Not seinen neuen Faserlaser überließ. Außerdem gilt mein Dank Karim Murr und Niels Syassen, welche die finale Version meiner Arbeit nochmals Korrektur gelesen haben.

Zu guter Letzt gilt es natürlich auch denjenigen Personen Dank auszusprechen, die mich außerhalb der Arbeit unterstützt haben. Hier ist insbesondere meine Frau Monica Neve zu nennen, die mein Seelenleben inzwischen vielleicht besser kennt als ich selbst und die in den letzten Jahren eine Menge Geduld mit mir und dem Experiment hatte. Daneben haben mich meine Eltern stets vorbehaltlos unterstützt.